



POLITECNICO
MILANO 1863

SCUOLA DI INGEGNERIA CIVILE,
AMBIENTALE E TERRITORIALE

Satellite data to support simulation of estuarine plumes

MASTER OF SCIENCE THESIS IN
ENVIRONMENTAL AND LAND PLANNING ENGINEERING

Author: **Umberto Sasso**

Student ID: 952681

Advisor: Prof. Marco Mancini

Co-advisors: Ing. Antonia Menzione

Academic Year: 2021-22

Abstract

River plumes are a widespread phenomenon worldwide in coastal areas near the mouths of rivers. Being generated by the flow of buoyant river water into the coastal sea, especially after severe precipitation events, they spread a mixture of suspended sediments, nutrients and pollutants of anthropic origin into the sea and along the coast. Accordingly, river plumes influence the coastal maritime environment and shelves seas area, modifying its physics, biology and geochemistry. The development of computational fluid-dynamics finite element models in these areas can be used to study and predict the dispersion and direction of the plumes and concentration levels of the pollutants transported. In these areas, in-situ measurements are only sometimes available in order to adequately calibrate the computational model. This work presents a new support approach for developing fluid-dynamics models in 2D and 3D, integrating the few in-situ measurements with data from multispectral optical satellites. Through the satellite images captured on the days in which the coastal area exhibited the fluvial plume phenomenon, using the recordings of the measurement stations available in the area, it is possible to understand which factors, and in what ratio, shape the fluvial plumes. In the absence of sampling of the concentrations of suspended solid sediments, it is possible to estimate the concentrations of solid sediments at the surface using equations based on the reflectance of the water, which act as a filter for the spectral bands of the satellite data. This estimate is used in the models to calibrate the concentration and diffusion of the tracer simulating the river plume. This thesis aims to study the fluvial plume phenomenon and to understand if, with the help of satellite images, it is possible to create a hydrodynamic model able to replicate the plume events captured by satellite. The results obtained with the aid of the 2D model can only partially simulate the direction and concentrations of the river plume, while the 3D model can reproduce a better flow field but with tracer concentrations that are not yet optimal.

Keywords: river plume, satellite data, computational models

Abstract in lingua italiana

I pennacchi fluviali sono un fenomeno molto diffuso in tutto il mondo nelle zone costiere vicino alla foce dei fiumi. Essendo generati dal flusso di acqua fluviale, specialmente dopo eventi di precipitazione intensa, essi disperdono a mare e lungo la costa una miscela composta di sedimenti in sospensione, nutrienti e inquinanti di origine antropica. Di conseguenza, i pennacchi fluviali influenzano l'ambiente marittimo costiero e le piattaforme continentali dei mari, modificandone la fisica, la biologia e la geochimica. L'elaborazione di modelli computazionali fluidodinamici agli elementi finiti in queste aree può essere utilizzata per studiare e prevedere la dispersione e la direzione dei pennacchi e i livelli di concentrazione degli inquinanti trasportati. Non sempre in queste zone si hanno misurazioni in-situ per poter calibrare adeguatamente il modello computazionale. In questo lavoro si vuole presentare un nuovo approccio di supporto per l'elaborazione di modelli fluidodinamici in 2D e 3D, integrando le poche misurazioni in-situ con i dati dei satelliti ottici multispettrali. Tramite le immagini satellitari catturate nei giorni in cui l'area costiera presentava il fenomeno del pennacchio fluviale, utilizzando le registrazioni delle stazioni di misura disponibili nella zona, è possibile capire quali fattori, e in che rapporto, condizionano i pennacchi fluviali. In assenza di campionamenti delle concentrazioni dei sedimenti solidi in sospensione, è possibile compiere una stima delle concentrazioni dei sedimenti solidi in superficie tramite equazioni basate sulla riflettanza dell'acqua che fungono da filtro per le bande spettrali dei dati satellitari. Questa stima è utilizzata nei modelli per calibrare la concentrazione e la diffusione del tracciante che simula il pennacchio fluviale. Questa tesi mira a studiare il fenomeno del pennacchio fluviale e a capire se, con l'ausilio di immagini satellitari, sia possibile creare un modello idrodinamico in grado di replicare gli eventi di pennacchio catturati da satellite. I risultati ottenuti dal modello 2D riescono solo in parte a simulare l'andamento e le concentrazioni del pennacchio fluviale; invece, il modello 3D riesce a riprodurre un campo di moto migliore ma con concentrazioni di tracciante non ancora ottimali.

Parole chiave: pennacchio fluviale, dati satellitari, modelli computazionali

Contents

Abstract	i
Abstract in lingua italiana	iii
Contents	v
1 Introduction	1
1.1 General introduction	1
1.2 Aim of the work	2
1.3 Geographical context	4
1.3.1 Ofanto river history	4
1.3.2 Ofanto River nowadays	4
1.3.3 Coastal area	9
2 Part I - Coastal river plume and satellite data	11
2.1 Coastal river plume dynamic description	11
2.1.1 The dynamic regions of river plumes	13
2.1.2 Plume mixing	17
2.1.3 Plume transport	19
2.1.4 Types of plumes	19
2.2 Satellite data - Remote sensing	22
2.2.1 Electromagnetic energy	22
2.2.2 Electromagnetic spectrum	23
2.2.3 Characteristic radiometric parameters for remote sensing	24
2.2.4 Interaction between solar radiation and the Earth's atmosphere	25
2.2.5 Interaction between solar radiation and natural surfaces	25
2.2.6 Sensors	26
2.3 Satellite data - Overview of Planet Labs satellites	27
2.3.1 PlanetScope satellite constellation	27

2.3.2	SkySat satellite constellation	29
2.3.3	RapidEye satellite constellation	30
2.3.4	Landsat 8 satellite	31
2.3.5	Sentinel-2 satellite constellation	33
2.4	Satellite images and plume patterns for the case study	35
2.4.1	Satellite images research	35
2.4.2	Hydro-meteorological data	38
2.4.3	Plume patterns and correlations	45
3	Part II - The hydraulic model for coastal river interaction	53
3.1	2D hydraulic model	54
3.1.1	TELEMAC-2D	54
3.1.2	Ofanto River flood modeling	58
3.1.3	Coastal zone modelling	64
3.1.4	Coastal modelling simulations and calibrations	67
3.2	3D hydraulic model	74
3.2.1	TELEMAC-3D	74
3.2.2	Coastal zone modeling	79
	Conclusions and future developments	85
	Bibliography	89
A	Appendix Part I	93
A.1	Satellite images	93
A.2	Matlab code	102
B	Appendix Part II	103
B.1	River model	103
B.1.1	TELEMAC-2D river model code	106
B.1.2	TELEMAC-2D river model results	108
B.2	Coastal model	111
B.2.1	TELEMAC-2D coastal model code	112
B.2.2	TELEMAC-3D coastal model code	114
B.2.3	Other 3D model results	117

List of Figures	119
List of Tables	125

1 | Introduction

1.1. General introduction

In the last century, growing industrial development and soil exploitation have affected the quality of surface waters, which have become a repository of anthropic substances of various origins [Heise and Förstner, 2007]. In this context, several rivers have undergone substantial changes (remediation of riverbeds and dams) and have received a large amount of domestic and industrial wastewater related to production activities near the water source [Kanbar et al., 2017]. Due to these wastewater discharges, riverbed sediments are often polluted. The flow of river sediments during flood events can affect water quality and contaminate floodplains and bathing areas near the estuary [Hissler and Probst, 2006], requiring extensive investigations. Therefore, the prediction of potential re-suspension and sediment transport in these heavily polluted river systems is a hot topic in today research [Lepesqueur et al., 2018]. Suspended sediment particles are integral to ecosystem health in many coastal environments as they are associated with the flux of heavy metals and micropollutants. Understanding the transport of suspended sediments is fundamental for managing water quality in coastal areas [Onishi et al., 1981]. Numerical models have long been important for understanding and evaluating sediment movement in coastal and marine environmental systems. However, predicting coastal sediment transport remains a challenge due to (highly complex) sediment dynamics and the need to understand the critical sedimentary processes underlying real-world dynamical system behaviour [Smith et al., 2011]. State-of-the-art regional-scale sediment transport models based on semi-empirical relationships suffer from significant prediction uncertainty unless constrained by observations [Amoudry and Souza, 2011]. Traditionally, observations for model initialization, calibration and validation have been collected via shipboard surveys or fixed moorings. Often, these data are unavailable or expensive and sampled with low spatial and temporal density [Zhang et al., 2014]. This thesis will use satellite data to support the hydrodynamic modelling of fluvial plumes without sampling in the area of interest.

1.2. Aim of the work

The purpose of this thesis is to take advantage of the available satellite data in order to support the reproduction, through hydrodynamics computational models, of the fluvial plumes generated by the Ofanto River in the Apulian coasts between Barletta and Margherita di Savoia. River plume events, especially for this torrential river, are particularly correlated with heavy rainfall events. This is because the plume mainly consists of suspended sediments, which are triggered in large quantities only after a certain threshold of river water velocity is reached.

The web platform of the American company Planet Labs provides a constantly updated (daily) database of satellite images captured by different types of multispectral optical satellites, both managed by the company and by NASA and ESA.

The research period taken into consideration for the search for images in the Ofanto River estuary area includes the time interval from July 1, 2019, to March 31, 2021. All the images available in the database on these dates are analysed, searching for each plume event that occurred, both of considerable size and impact (reaching dimensions of tens of kilometres) and of medium-small size (reaching dimensions of hundreds of meters). After careful research, it was decided to represent the rainfall event of March 10 and 11, 2021, since the satellite image of March 11 is the one that best shows the plume effect from the Ofanto River mouth to the Adriatic Sea. This rainfall event was not the highest in terms of cumulative precipitation, but it is the one in which the plume is clearly visible from the satellite image; instead, on many other dates considered, the images were non-existent because the satellites did not pass over the area on the required days, or the images were available but with only the cloud layer captured.

The hydrometric measurements of water level surface elevation (stage) and volumetric discharge (flow) closest to the Ofanto River mouth are those recorded by the stream gauging station of San Samuele di Cafiero, municipality of San Ferdinando di Puglia (BT), which is located about 18 kilometres from the river mouth. For this reason, it was necessary to develop two simulation models:

1. the simulation of the flow rate from the stream gauging station to the mouth, in order to extract the downstream discharge considering the overflow areas caused by the flood event and the time in which it arrived at the mouth;
2. the simulation of the lower part of the river and its outlet to the sea, in order to simulate the plume caused by suspended sediments.

The work aims to reproduce the fluvial plume phenomenon by developing a hydrodynamic model capable of replicating satellite-captured plume events. In order to obtain a more precise simulation of the river plume, the following are integrated into the model: the hydrodynamic data of the river at the mouth, the available anemometric data recorded in more detail and as close as possible to the domain and the tidal data obtained from the TPXO global model [Egbert and Erofeeva, 2002].

The proposed modelling framework is based on TELEMAC-MASCARET [Hervouet, 2007]. TELEMAC-MASCARET is an integrated suite of solvers for use in the field of free-surface flow. Having been used in the context of many studies worldwide, it has become one of the major standards in its field.

For the river simulation model, the hydrodynamic simulation is carried out thanks to the TELEMAC-2D software; it solves Saint Venant equations or shallow-water equations (SWEs) based on the finite element method (FEM) over non-structured triangular grids.

For the downstream river and sea domain simulation model, the hydrodynamic simulation is initially performed by TELEMAC-2D, but failing to reach good plume replication results, a three-dimensional model has been implemented. The main reason why the two-dimensional model fails to satisfactorily replicate the river plume is that the main 2D results at each node of the computational mesh are depth-averaged. This is not optimal because the border area between the river mouth and the marine area is influenced by various factors of salinity mixing and instability of the currents at different depths. The 3D simulation is carried out thanks to the TELEMAC-3D software, which uses the same horizontally unstructured mesh as TELEMAC-2D but solves the Navier-Stokes equations in non-hydrostatic mode. Simulation of the three-dimensional model is necessary in order to achieve a reasonable replication of the river plume because it can better account for and reproduce the surface transport of the tracer, the mixing between fresh and salt water and the river and sea temperature. These more reasonable results are possible to get because with TELEMAC-3D the 3D results at each point in the resolution mesh are in all three directions (not depth-averaged as for the two-dimensional model).

Therefore, this thesis aims to evaluate and discuss the benefits of considering the use of satellite data to aid the calibration of computational models for the simulation and prediction of plumes at river mouths that occur due to flood events.

1.3. Geographical context

1.3.1. Ofanto river history

In Ancient Italy, the Ofanto River was known by the name of Aufidus and is famous for various reasons; along the river course, there were ancient cities that were the protagonists of many important historical events, for example, Compsa (now Conza della Campania), Canusium (now Canosa di Puglia), the fortress of Cannae (where the bloody Battle of Cannae was fought) and Venusia (present-day Venosa).

In the last century, the project area was the subject of massive reclamation works which involved the drying up of the Mediterranean marshes and the destruction of the buffer areas consisting of the edges, banks, oxbow lakes, lagoons and marshes. This phenomenon is common to the whole Tavoliere delle Puglie area.

From the traceable bibliographic and cartographic information it can be deduced how these types of wetlands were already mentioned, in Roman times, by Caio Silio Italico who cited the presence of the "stagna Aufida" precisely in correspondence with the Ofanto River mouth area (Aufidum in Latin). Further information can emerge from the account of the presence of the Salpi lagoon whose southern limit corresponded to the alluvial plains near the town of Barletta, including the Ofanto River mouth [Caldara et al., 2002]. One of the most important cartographies that can be useful for locating the lagoon residues present near the mouth of the Ofanto river starting from 1808, is the map compiled by the well-known Paduan geographer Giovanni Antonio Rizzi Zannoni (Figure 1.1).

In addition to the reclamation works, the Ofanto River sediments contribution caused the deposit of solid material transported in suspension by the waters and the closure of the last stretches of water.

1.3.2. Ofanto River nowadays

The Ofanto River originates in Campania and, crossing Basilicata thus bypassing the northern border of Mount Vulture, flows, for a large part, in the area between Tavoliere delle Puglie and Terra di Bari, with a south-west to north-east direction, flowing into the Adriatic Sea between the inhabited centers of Margherita di Savoia and Barletta. The Ofanto River has a basin of about 2790 square kilometers (Figure 1.2), which affects, in fact, the territory of three regions, Campania, Basilicata and Puglia and has an almost trapezoidal shape with a more significant extension on the right side of its basin, in Campania territory, due to the high erodibility of the territory crossed, consisting mainly



Figure 1.1: Extract from the cartography of the Kingdom of Naples in 1808 by G. A. Rizzi Zannoni; focus on the Ofanto River mouth and the nearby town of Barletta.

of loose sedimentary deposits, in correspondence with the part extending towards the south. It is 165 kilometers long (Figure 1.3) and is divided into Alto Ofanto (Irpinia part of the river), Medio Ofanto (Lucanian part and first Apulian part) and Basso Ofanto (second Apulian part of the river). The sediments transported by the Ofanto River find their natural epilogue in forming a low and sandy coast, generally typical of Adriatic and Mediterranean rivers, contributing to the filling of the Manfredonia gulf.

The river is in a juvenile evolutionary stage, therefore the drainage basin is still underdeveloped and therefore subject to expansion [Dellisanti, 2021]. The tributaries, despite being of little consistency in terms of flow, nonetheless play a decisive role, in fact, they ensure the maintenance of a delicate hydrographic and hydrogeological balance within the river through the constant solid and liquid supply, capable of supplying the water to the riverbed throughout the year, which is very important for the life of the river [Orsino, 2020].

Not being dominated by glaciers or snow deposits and being endowed with scarce spring supplies, its power supply depends almost exclusively on the water supplies generated by the rains. Therefore it presents a discontinuous flow regime of a torrential nature with highly variable discharges, depending on the climatic conditions and rainfall with an average at the mouth of 15 cubic meters per second. It is characterized by long periods of low flow in summer, from June to September, while for the remaining months of the year it has considerable flows, being able to reach instantaneous peaks of flow, on the

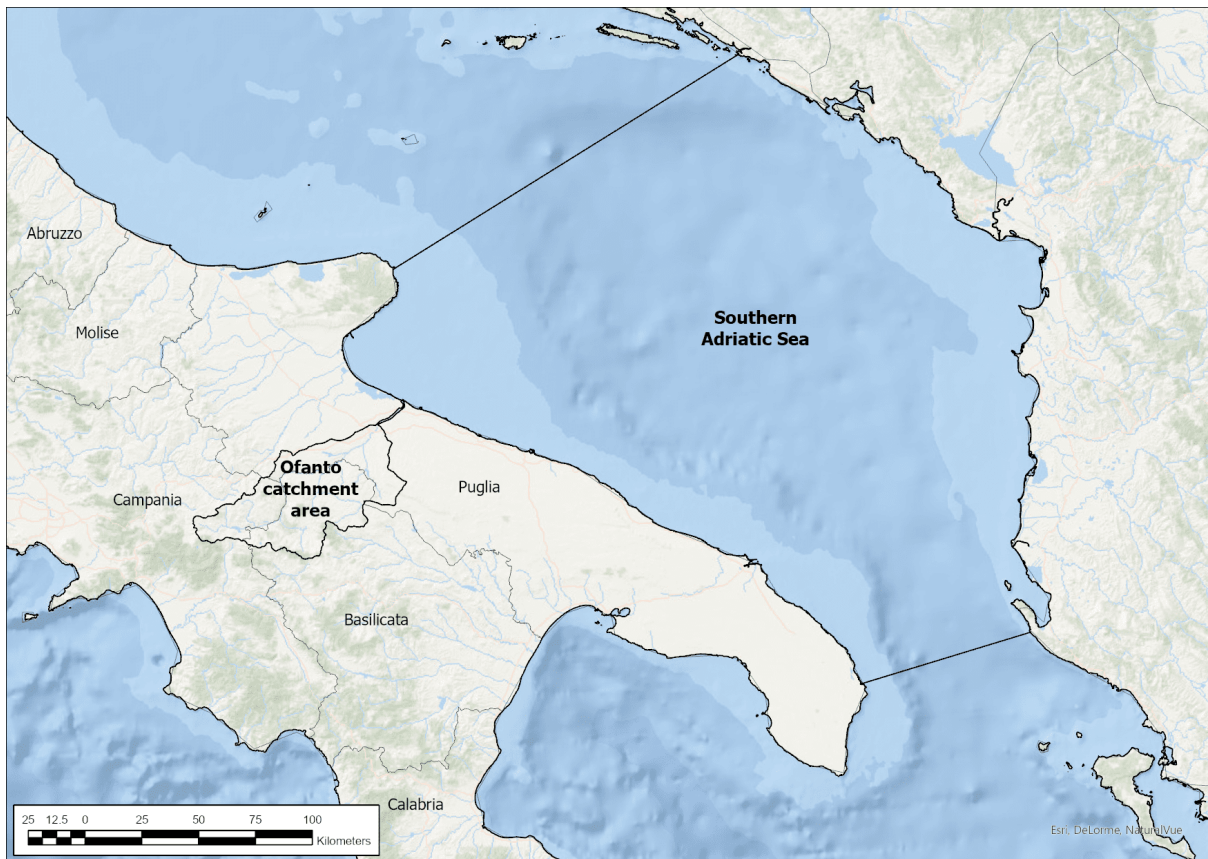


Figure 1.2: Ofanto catchment area and southern Adriatic Sea.

occasion of flood events, of the order of hundreds of cubic meters per second. The lack of vegetation, the presence of loose impermeable soils, the high rainfall and the irregular streambed, give the river a very intense erosive action in the upper basin area and partly in the middle.

As reported by the studies conducted by the Apulian Basin Authority, from the point of view of the solid balance, the Ofanto River is in a state of imbalance. The geological and geomorphological instability in the Municipalities present in the basin is severe; in fact, over 40% of the territory is affected by phenomena of erosion and soil instability with the formation of erosion phenomena, while 17% of the Municipalities present report severe forms of hydrogeological instability [Dellisanti, 2021]. The phenomenon is evident precisely in the mouth section, where for years there has been an intense erosion of the sandy coast, which was formed, over the centuries, with the contributions of sediments from the river. From the analysis of the cadastral maps, it is evident how the river changed its course over the years; this is much more evident at the mouth, where the streambed has moved to the northwest by several hundred meters. At the same time, the coastline underwent an important retreat. The beginning of the coastal erosion phenomenon in

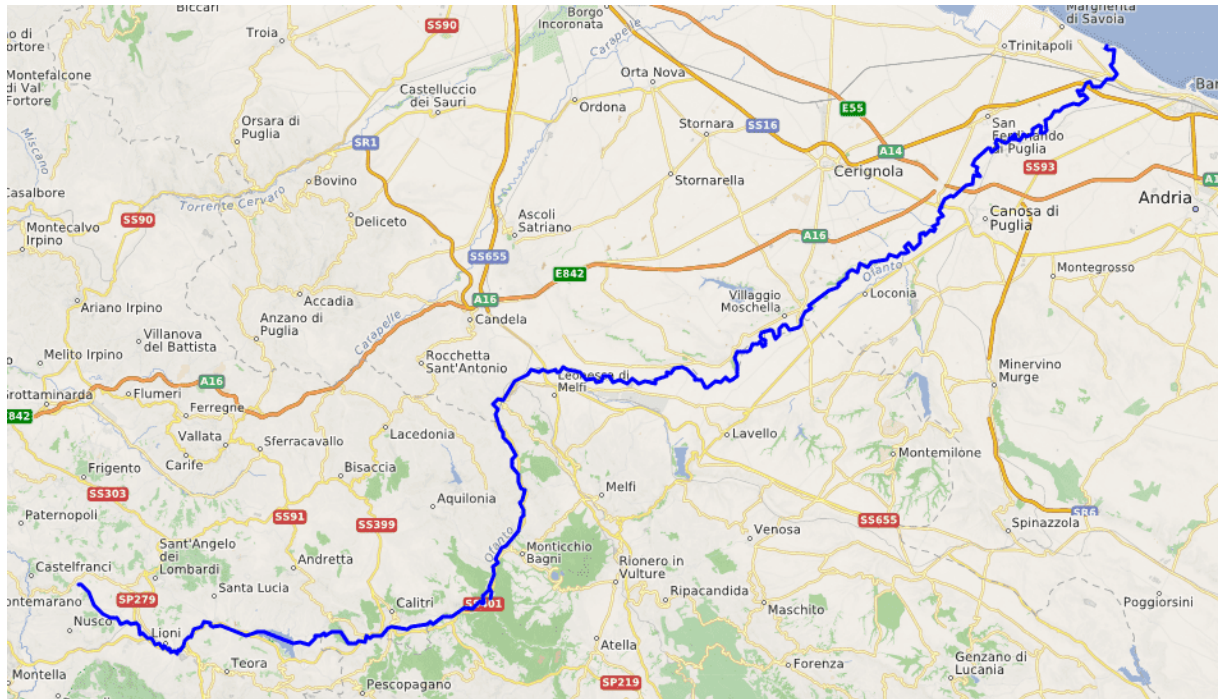


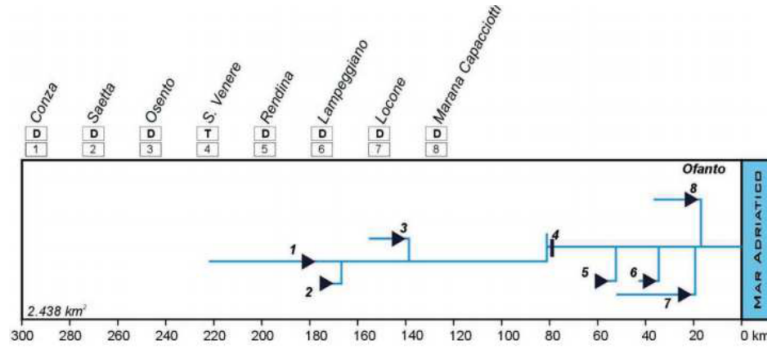
Figure 1.3: Ofanto River map [wik, 2020].

question dates back to the 1920s when the river hydraulic works and the marshy areas reclamation surrounding it started. The retreat of the mouth, already between 1925 and 1984, has been estimated at a few hundred meters, with a peak acceleration of the phenomenon between the years 1964 and 1984. It estimated that from 1992 to 2008 the coast adjacent to the mouth underwent a retreat of about 150 meters (about 9 meters per year). Figure 1.4a and Figure 1.4b, obtained from previous studies, show that the river mouth, from the 1960s to today, has changed considerably, in fact, the coast moved back hundreds of meters.

Figure 1.5 shows a nowadays image of the last two kilometers of the Ofanto River and its estuary mouth.

As reported in the Apulian Regional Coastal Plan (PRC), the retreats in this last river stretch are partly due to a previous artificial diversion of the mouth of the watercourse and, mainly, to the reduction of the solid supply from the river due to human actions in the hydrographic basin and due to the construction of various reservoirs and weirs along the river (Conza, Saetta, Rendina, Marano Capacciotti and Locone dams, in addition to the Santa Venere weir; the quantity of water that can be regulated amounts to approximately 310,000,000 cubic meters per year). In fact, since the second half of the 1900s, in addition to the more intensive use of the land, numerous dams and diversion works have been built along the Ofanto River and its tributaries, as shown in the following simplified diagram

in Figure 1.6a. By way of example, Figure 1.6b and Figure 1.6c show the Conza dam and the Saetta dam, respectively.



(a) Diagram of the dams and weirs built in the Ofanto basin.

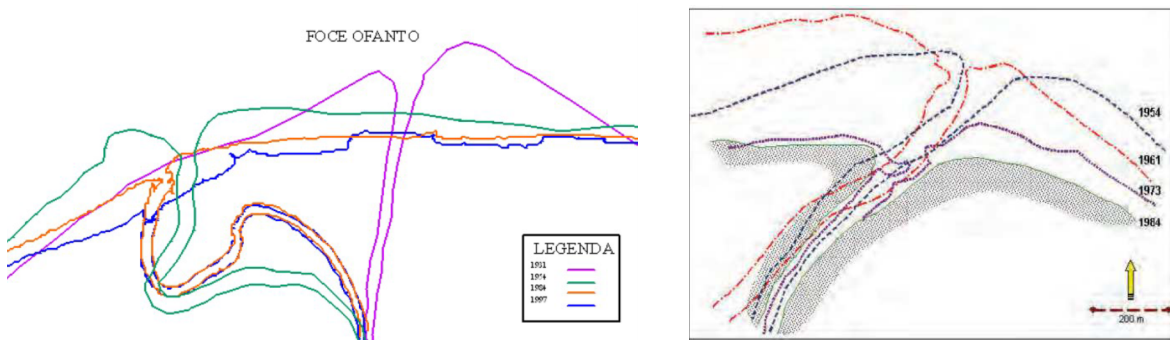


(b) Conza dam (Campania Region).



(c) Saetta dam (Basilicata Region).

Figure 1.6: Dams and weirs in the Ofanto catchment area.



(a) Change of the Ofanto River mouth between 1931 and 1997 (taken from the Apulian Coastal Regional Plan).

(b) Retreat of the Ofanto River mouth based on the IGM surveys [Pennetta, 1988].

Figure 1.4: Change of the river mouth in the last century (according to the two previous studies).



Figure 1.5: Last two kilometers of the Ofanto River and its estuary mouth.

The aforementioned interventions, together with the uncontrolled removal of the river bed material, have drastically reduced the solid flow conveyed by the river towards the coast; all this initially determined the erosion and leveling of the mouth and, subsequently, the erosion of large stretches of coast near the mouth of the Ofanto, both in the Municipality of Margherita di Savoia and in the Municipality of Barletta. This phenomenon is still ongoing today. It is, therefore, quite clear that the final section of the Ofanto River is not in equilibrium from the point of view of the global solid balance.

1.3.3. Coastal area

The coastal area of interest extends for about 15 kilometres, i.e. from the port of Margherita di Savoia to the port of Barletta (Figure 1.7).

The coastline is mostly sandy with a dune belt in formation, low and flat beaches and wetlands of considerable environmental value (Ofanto River mouth). The sandy coast was formed over the centuries by the deposits of sediments by the Ofanto River.

The coastal erosion phenomenon began significantly with the river engineering works regarding the Ofanto River and the reclamation of the marshy areas of the last century. In addition to the hydraulic works (dams, weirs) in the river basin already mentioned, the natural solid contributions to the sea have also decreased because of sand extraction licenses along the entire river. A study by the Institute of Hydraulics and Hydraulic



Figure 1.7: Coastal area between Margherita di Savoia and Barletta (area affected by the Ofanto's fluvial plume phenomenon); image from Sentinel-2A, taken on March 5, 2023.

Constructions of the Faculty of Engineering of Bari (1984) ascertained that the sediments transported to the beaches consist mainly of silts and clays and, to a minimum, of fine sand. The beaches, therefore, lack the contribution of sandy sediments, which replace those subtracted and partly transported by the longitudinal currents [Kobayashi et al., 2000].

2 | Part I - Coastal river plume and satellite data

This chapter aims primarily to introduce the phenomenon and dynamics of fluvial plumes, what affects their size, direction and mixing. Secondly, to introduce remote sensing and to list the features and tools that optical satellites have available and which platform was used to collect satellite images in the period under consideration. Furthermore, the available meteorological and hydrological data are introduced and correlations are advanced between the trend of the fluvial plume and the available data.

2.1. Coastal river plume dynamic description

River plumes are freshened water masses formed in the sea as a result of mixing river discharge and saline seawater. The plumes are therefore generated by the flow of buoyant river water in the coastal area of large water bodies such as seas, oceans and, in certain specific cases, great lakes.

All the rivers of the world carry more than a third of land precipitation to the seas [Trenberth et al., 2007]; at the mouth of each river, therefore, there are freshwater fluxes that flow through narrow coastal outlets to the seas where they significantly influence the properties and circulation of the water [Milliman and Farnsworth, 2013]. These regions around rivers mouths are transition zones, where the rivers' freshwaters merge with the seas' deep, salty waters. In these transition zones, a series of physical processes occur, including stratified-shear mixing, frontal processes, geostrophic transport, and wind forcing, concerning the transport and mixing of buoyant freshwater.

In literature, river plumes are sometimes referred to as regions of freshwater influence (ROFIs). Considering the coastal area of the seas and oceans, the river discharges into the sea form plumes, whose shape, size and orientation vary considerably according to the forcing and geometry of each system. Very different plumes can occur not just considering rivers in different areas of the world but also considering individual river systems, which

can exhibit plumes with distinct characteristics under varied forcing conditions.

The distinguishing dynamical feature of a river plume is the horizontal advection of freshwater from the river mouth that defines the shape and character of the plume [Horner-Devine et al., 2015].

A river plume is composed of dynamically distinct regions, with spatial and temporal scales that can also be very different from each other. It is a multiscale flow structure in which the main parameters that influence the structure and scale of the phenomenon are freshwater river discharge (a factor that enormously influences the phenomenon), bathymetry and the geometry of the coast, wind stress, Earth's rotation, tidal amplitude, ocean currents and water properties (sea salinity and river water features).

Freshwater flow may be the parameter that typically has the most significant variability within a system, especially for torrential rivers; this variability can translate into (at least) an order of magnitude for the same river and up to four orders of magnitude when considering different river systems. All this leads to significant structural and dynamic differences between systems. From the events studied in the literature, it is possible to see how the plumes vary according to the river flow rate. For example, the River Teign (Devonshire, England) has a relatively small average discharge (5 cubic meters per second), it forms a few meters wide plume after each ebb tide and it dissipates within a few hours [Pritchard and Huntley, 2006]; if moderate discharge is considered, such as that of the Merrimack River (Massachusetts, USA, according to [MacDonald et al., 2007], the plume occasionally persists between tides, depending on the wind; with higher discharges Columbia River's example (Washington, USA) is found, with an average discharge of about 10,000 cubic meters per second, where the plume is strongly influenced by the tide near the estuary, but the plume is persistent and governed by other processes well beyond this region at the mouth [Horner-Devine et al., 2009] and [Hickey et al., 2010]; considering instead one of the longest rivers in the world, the Mississippi River (USA), with an average discharge of 30,000 cubic meters per second, [Cochrane and Kelly, 1986], [Murray, 1998] and [Zhang and Hetland, 2012] show that the river creates a huge persistent plume dominating the coastal circulation of Louisiana and Texas.

Studying plume phenomena is important because they can impact marine circulation and ecosystem health. River waters carry terrigenous material and sometimes even polluting materials, arriving in coastal waters, which are often ecologically sensitive. The dilution rate and transport processes within the plume have the most significant influence on circulation and ecosystem health. Vertical mixing mainly controls plume dilution: as the salinity of the plume increases, the concentrations of materials carried by the river de-

crease. Horizontal advection is the phenomenon that primarily controls plume transport: it is driven primarily by plume buoyancy and hence by mixing [Horner-Devine et al., 2015].

2.1.1. The dynamic regions of river plumes

A river plume can be divided into different dynamical regions: the source region, the near-field, the mid-field and the far-field plume [Horner-Devine et al., 2015].

The first zone, the source region, is the estuarine region, inside the river mouth, where the initial buoyancy and momentum of the river plume are set. In this area, estuarine processes determine buoyancy and momentum that initiate the river plume. The [Nash et al., 2009] study of the aforementioned Columbia River suggests that the competition between river flow and the mixing provided by tidal energy within the estuary determine the median salinity, thickness and turbulent mixing rates of the river plume. In strongly forced systems, the water flow rate leaving the estuary forms a buoyancy layer separating itself from the riverbed near the river mouth. This phenomenon is called the liftoff point; it is the location of the bottom attached salt front where the buoyant outflow loses contact with the bottom. This point is usually observed where bottom depths begin to increase.

The second zone is called the near-field region: this is a jet-like region of initial plume expansion where the momentum of the plume layer dominates over its buoyancy, resulting in intense mixing. The near-field region begins at liftoff or river mouth, and since the momentum in this region exceeds the buoyancy of the plume, there is a Froude number higher than 1 (supercritical flow). Generally, the near-field boundary is where the flow stops to be supercritical, i.e. when the Froude number is less than or equal to 1 [Hetland, 2010]. The near-field momentum balance is dominated by barotropic and baroclinic pressure gradients, turbulent interfacial stress between the discharging plume layer and the underlying ambient water, and flow acceleration [McCabe et al., 2008], with the interfacial stress as the primary driver of plume deceleration under low discharge conditions and peak ebb tide [Kilcher et al., 2012]. In those areas of the Earth where large tides occur, the near-field plume is referred to as the tidal plume; in these cases, the tide plays the primary role and the dynamics of the near-field region become strongly time-dependent [Horner-Devine et al., 2009]. There may be exceptional cases in which the near-field plume leaves the estuary as a far-field plume: it is attached to the right bank in the northern hemisphere or the left bank in the southern hemisphere. This phenomenon happens when the river mouth is very extensive.

In Figure 2.1 the plume liftoff process and the near-field plume region are schematized;

this image is taken from [Horner-Devine et al., 2015].

The third zone is called the mid-field region, where Earth's rotation begins to dominate, arresting plume spreading and turning the plume in the downcoast direction. Here, the inflowing river water transitions from the inertial near-field into a geostrophic or wind-dominated far-field plume [Horner-Devine et al., 2015]. In this region, the Earth's rotation dominates the dynamics of the plume, while the incoming momentum due to the river flow is progressively lost. Here, the Coriolis force, centripetal acceleration, and transverse internal pressure gradient dominate the momentum equilibrium [Yankovsky and Chapman, 1997]. For most of the studies reported in the literature, these actions involved cause the

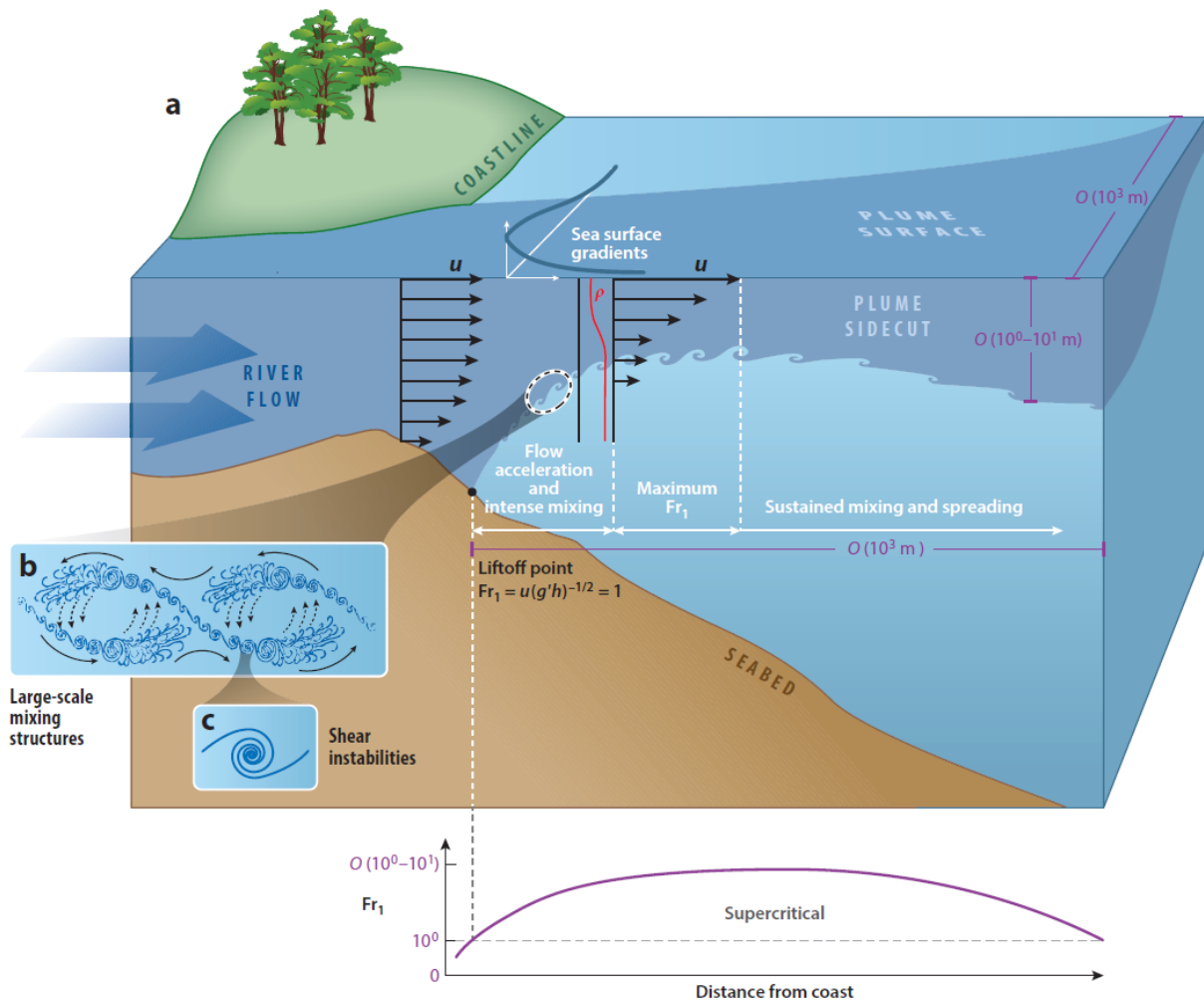


Figure 2.1: (a) Schematic representation of the plume liftoff process and the near-field plume region. (b) Large-scale mixing structures in the flow acceleration region. Panel (b) adapted from [Geyer et al., 2010]. (c) Shear instabilities comprising the large-scale mixing structures. Image and description from [Horner-Devine et al., 2015].

plume to change direction (initially directed offshore), forming a coastal current parallel to the coast [Garvine, 1987].

The fourth zone is called the far-field region: this is the region beyond the mid-field where the plume water has lost all memory of the inflow momentum of the river discharge but is still distinct from the ambient receiving water. This region can extend even for hundreds of kilometres from the river mouth. In this region, the plume dynamics are mainly governed by the Earth's rotation, buoyancy, wind stress and sometimes bottom stress. If the wind is not particularly strong to force the plume offshore, a geostrophic current is formed, which carries the water from the river along the coast. The coastal current is also dependent on the shelf slope and the bottom (if the plume is in contact with it); these factors influence the far-field region structure and propagation speed [Lentz and Helfrich, 2002].

Figure 2.2 shows a so-called prototypical plume, i.e. a plume composed of all four regions just described.

In Figure 2.3, from [Rijnsburger et al., 2021] concerning the evolution of plumes fronts in the Rhine Region of freshwater influence, it can be seen that two fronts bound the entire plume: one called the outer front (OF) and the other one called the inner front (IF). The outer front delimits the entire plume, marking the boundary between the mixed fluvial

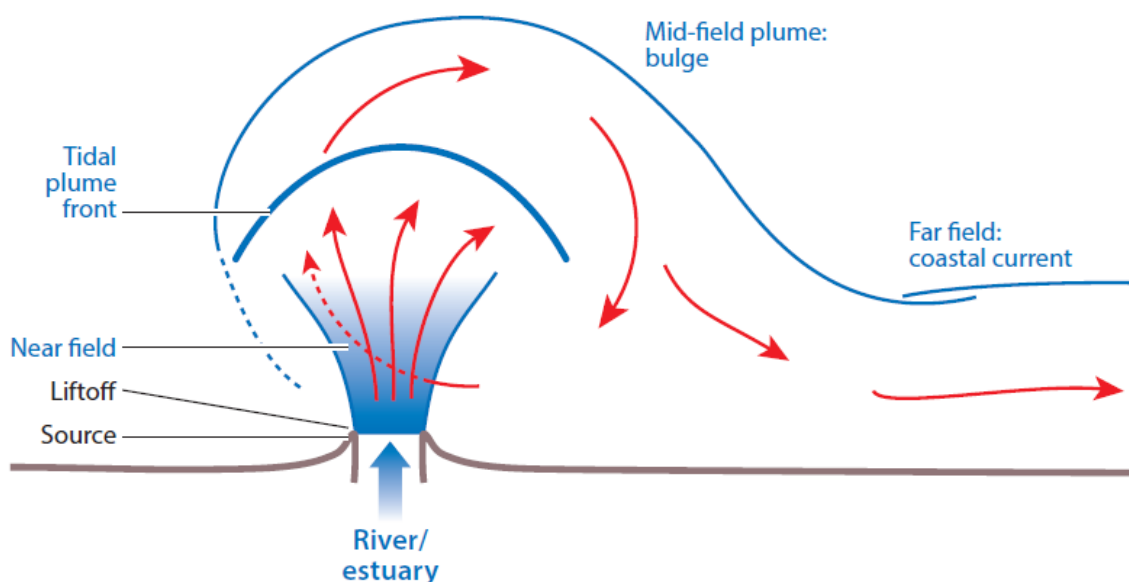


Figure 2.2: Schematic representation of the prototypical plume comprising all dynamical regions. Image and description from [Horner-Devine et al., 2015].

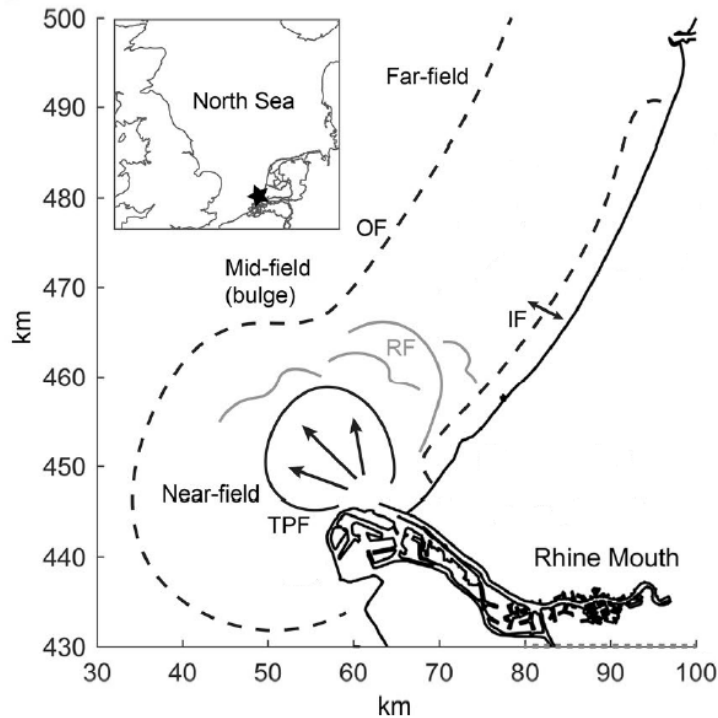


Figure 2.3: Schematic of the Dutch coast with different types of river plume fronts: tidal plume front (TPF), inner front (IF) of entire plume, outer front (OF) of entire plume, and relic tidal plume fronts (RF). Image and description from [Rijnsburger et al., 2021].

and saline water with the denser seawater. Wind intensity and persistence significantly influence the on- and offshore displacement of this front [Fong and Geyer, 2001]. OF boundary is mainly seen in large-scale plumes, such as the Columbia River, Delaware Bay, Chesapeake Bay, and Hudson River plumes [Horner-Devine et al., 2015]. The inner front, which usually extends from the mouth to the far-field, separates the shallow coastal waters from the fluvial plume, extending along the entire length of the fluvial plume. Its extension can reach very high distances; in the River Rhine's example of Figure 2.3, the inner front can reach more than 100 kilometres [Rijnsburger et al., 2021]. IF has been observed to move offshore under upwelling favourable winds by [Fong and Geyer, 2001] and by tidal straining by [de Boer et al., 2009].

In Figure 2.3 it is possible to see a possible tidal plume front (TPF). As previously mentioned, TPF is a near-field plume in which the tide (usually with high amplitudes) modulates the outflow and the dynamics of the area become highly time-dependent. The persistence of the tidal plume is related to the freshwater discharge released from the river mouth at each ebb tide. Still considering the examples of the Columbia River [Kilcher and Nash, 2010] and the Teign River [Pritchard and Huntley, 2006], the first river TPF

(average flow of 10,000 cubic meters per second) lasts for about 6-9 hours after ebb tide, but is sometimes still visible after 12-14 hours when a new TPF forms; while the second river TPF (average flow rate of 5 cubic meters per second) dissipates after 4-5 hours. Therefore, if the river discharge is not excessively large, the modulation of the river outflow by the semidiurnal tide determines the formation of a new TPF at each ebb [Hessner et al., 2001].

2.1.2. Plume mixing

As it evolves, the plume becomes more and more diluted; this is due to the addition of salt into the plume by mixing. It happens that there is an ever-smaller difference in density between the waters of the plume and the oceanic ones.

It is not always possible to catch the plume in all its potential evolutionary stages, i.e. near-field, mid-field (bulge) and far-field (along the coast); this is because the dilution path can end in any stage due to the strength of the mixing processes respect to the initial flow rate. In many cases, a slight initial discharge leads to the dilution of the entire plume before it reaches all its evolutionary stages [Horner-Devine et al., 2015].

Mixing in the near-field region

Some of the plume's most intense turbulence and mixing occur in the near-field region. Turbulence is most intense in the shoaling region immediately seaward of the liftoff point and decreases throughout the near field [MacDonald et al., 2007].

Mixing in fluvial plumes in the near-field region is dominated by stratified-shear flow instabilities [Horner-Devine et al., 2015], in particular Kelvin-Helmholtz (KH) instabilities. In the near-field plume, a strong shear, of the order of $0.5\text{--}1\text{ s}^{-1}$, is often present at the base of the plume, with density differences of 15–20 kilogram per cubic meter between the plume and ambient waters. These conditions lead to the development of Kelvin-Helmholtz billows [Smyth et al.] and subsequent turbulent mixing.

According to [Hetland, 2010], the Froude number in the near-field at some point starts to decrease due to the effect of low-momentum salt water entering the plume (salt water density decelerates the plume). This results in a decrease in mixing. The trend of the Froude number in this situation is described by [Hetland, 2010] as follows:

$$\frac{\partial Fr_1}{\partial x} = \frac{\frac{\partial W}{\partial x} hu(Fr^2 + 2) - 3w_e Fr^2 W}{2WhFr(Fr^2 - 1)}, \quad (2.1)$$

where Fr_1 is the critical Froude number, h is the interface depth, u is the upper-layer velocity, W is the plume width, w_e is an entrainment velocity of ambient fluid across the base of the plume, and x is in the streamwise direction. Thus, the seaward evolution of Fr_1 results from competition between the acceleration associated with spreading and the deceleration associated with mixing, the left and right terms in the numerator, respectively.

Wind mixing

Compared to the turbulence levels just described for the near-field, which are very energetic, wind stress generally results in lower turbulence levels. [Houghton et al., 2009] on the simulation of the release of a dye in the plume in the far-field and the measurement of the variation of the salt fluxes, shows that the action of the wind acts with average dissipation rates that are one or two orders of magnitude lower than at the rates observed in the near-field.

Mixing of the plume by the wind relies primarily on shear in the surface Ekman layer [Horner-Devine et al., 2015]. The Ekman layer is the layer in a fluid where there is a force balance between pressure gradient force, Coriolis force and turbulent drag. Vagn Walfrid Ekman first described it. Ekman layers occur both in the atmosphere and in the ocean. The Ekman layer occurs at the surface of the ocean and is forced by surface winds, which act as a drag on the surface of the ocean. Thus the Ekman transport in the surface layer will be constant for a given wind stress, but the velocity of the flow is inversely proportional to the depth of the plume.

According to [Fong and Geyer, 2001], the action of the wind in the far-field plume modifies the mixing response: if there is an upwelling wind, the plume tends to thin in depth; if there is a downwelling wind, the plume tends to thicken deep. The plume mixes to a certain critical depth, depending on wind stress and freshwater thickness.

Mixing in the bottom boundary layer

Plumes can interact with the seafloor, especially when tidal phenomena are very accentuated: plume mixes from seafloor due to bottom stresses and tidal flow [Horner-Devine et al., 2015]. This phenomenon occurs mainly in wide and shallow seas, with strong tides, as in the North Sea (Northern Europe).

Tidal action can periodically increase and decrease vertical stratification [de Boer et al., 2008], can cause periodic separation of the plume from the coast [de Boer et al., 2009], and can promote mixing.

2.1.3. Plume transport

The previous section described plume mixing processes, which play an essential role in plume transport because baroclinic pressure gradients, proportional to internal density gradients, drive plume transport [Horner-Devine et al., 2015]. This section describes the dominant parameters affecting coastal transport.

What dominates the transport can vary from case to case; the main parameters influencing the plume transport are buoyancy, wind stress, coastal currents, bottom slope along the coast and Earth's rotation.

The importance of the wind is typically considered weaker in the near field, where the inertia of the river flow is dominant, while it is more crucial in the mid-field and far-field. The wind, especially if strong, plays a decisive role in transporting the plume; it is often the dominant driver of transport in a plume. When an upwelling wind (i.e. a coastal wind blowing against the coastal current) acts on the plume, creating an offshore flow, the transport along the coast decreases; when a downwind (i.e. a coastal wind blowing in the same direction as the coastal current) acts on the plume, creating an onshore flow, coastal transport improves [Fong and Geyer, 2001].

Similarly, coastal currents affect plume transport in two possible ways: if the coastal current is in the same direction as the plume, it increases transport; if the coastal current opposes the plume, it will decrease the transport.

2.1.4. Types of plumes

As previously described, the plume can be composed of: a near-field region (typically of the order of kilometres from the river mouth), in which the supercritical condition is satisfied until the outflow conditions become sub-subcritical; a mid-field region (transition region), where active processes in the near-field switch to geostrophic dynamics active in the far-field; a far-field region, where the plume is diluted and has become geostrophic. Every region listed can be influenced by winds, waves, coastal currents and tidal currents, but each factor has a different weight depending on the river and the geographical region in which the phenomenon occurs. However, in particular, the external forcing is the wind that often predominantly changes the shape and dilution path of the plume.

In [Horner-Devine et al., 2015] different morphologies of fluvial plumes are shown and thoroughly described; Figure 2.4, taken from their work, shows six possible types of plumes.

Plume A, called the prototypical plume, includes all previously analysed dynamic regions. A narrow mouth usually characterises it; often, a relatively high river discharge is required to create this plume. The Earth's rotation strongly modifies its dynamics.

Plume B, called the non-rotational plume, includes the near-field region and, at most, the mid-field region. It is created in areas with no strong coastal current and where the Earth's rotation is less influential (at the equator). It is characterised by a supercritical flow condition and is often considered analogous to an engineering jet [Jones et al., 2007].

Plume C, called the wide estuary plume, manifests as a plume without near-field and mid-field regions with a bulge plume, but only with the far-field region. Large river mouth areas characterise this type of plume, in which the freshwater separates from one side due to the Earth's rotation inside the estuary.

Plume D, called the angled inflow plume, may occur when the river mouth is angled with the coast. It typically shows only the far-field region, but plume transport is greatly influenced by whether the inflow is lined up or opposite the direction of the coastal current.

E plume, called the delta plume, occurs especially for the largest river systems of the world, such as the Nile River (Egypt), Mekong River (Vietnam), Yangtze River (China) and Mississippi River (USA). As the name implies, large river deltas are the lead actor for this plume, where freshwater flows through a branching channel and reaches the ocean usually without creating near-field and mid-field regions; indeed, the plume is located along the coast.

Plume F, called the region of freshwater influence plume, occurs in regions such as Northern Europe, for example, in the Rhine River [Simpson et al., 1993] and Liverpool Bay [Verwey et al., 2009]. In this case, the seas are shallow and the plume interacts directly with the sea bottom, becoming more irregular, but in any case, always conditioned by forces such as wind and tide, which can change its shape and direction.

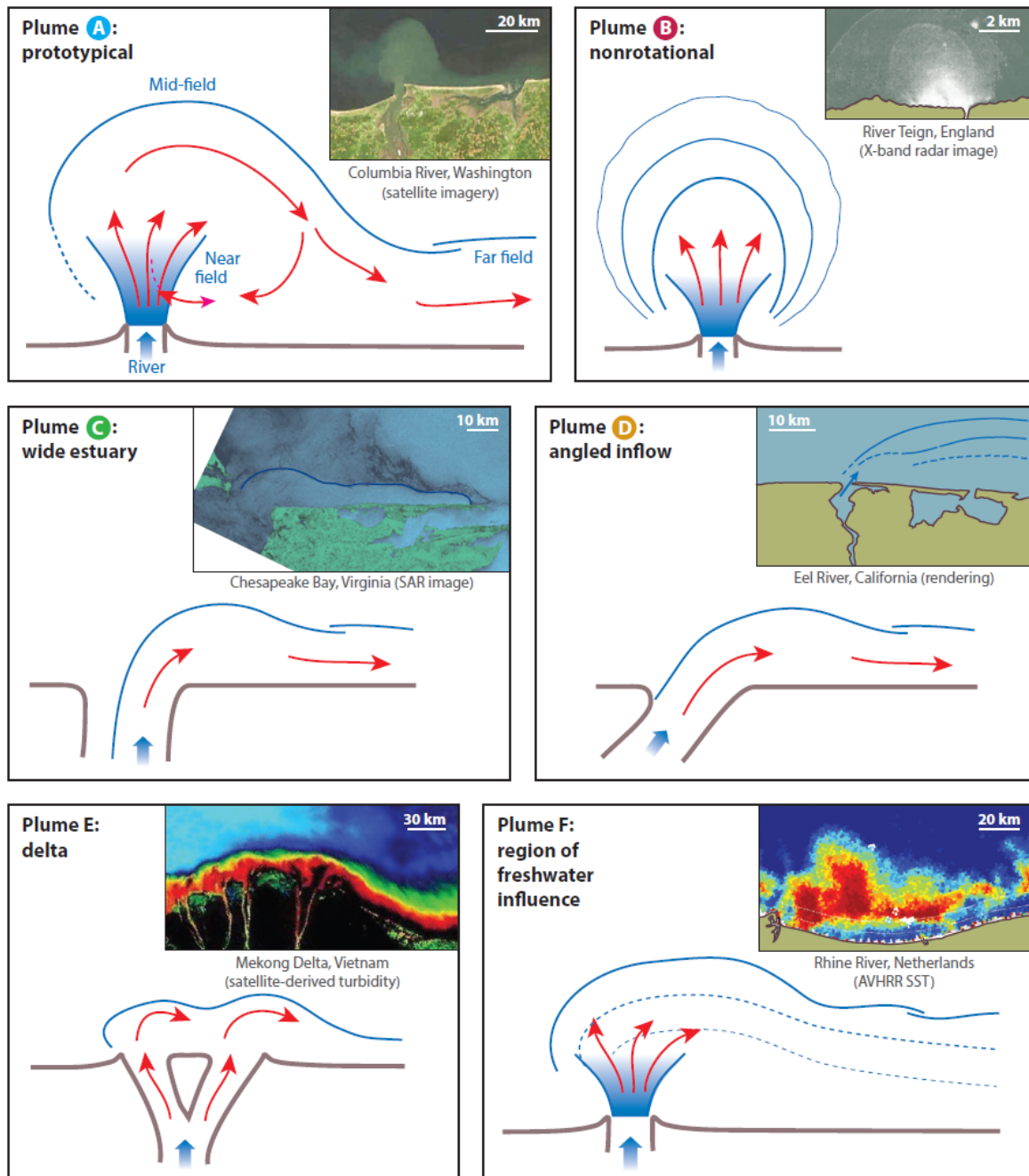


Figure 2.4: River plume morphologies: prototypical (plume A); nonrotational (plume B); wide estuary (plume C); angled inflow (plume D); delta plume (plume E); and region of freshwater influence (plume F). Inset images show examples of each plume type: (plume A) the Columbia River, (plume B) River Teign, (plume C) Chesapeake Bay, (plume D) Eel River, (plume E) Mekong River, and (plume F) Rhine River. Image and description from [Horner-Devine et al., 2015].

2.2. Satellite data - Remote sensing

Remote sensing is defined as the technical-scientific discipline that brings together techniques, devices and interpretative means capable of emphasizing the qualitative and quantitative characteristics of objects placed on the Earth's surface through the acquisition, processing and interpretation of data collected from platforms land, air or satellite without direct contact with the object under investigation.

Since there is no contact between the object and the device, remote sensing is based on the electromagnetic propagation emitted or reflected by the object.

In general, the device that allows the measurement of the emitted or reflected energy is called sensor, while the vehicle on which the sensor is mounted, such as an aircraft, satellite or drone, is called platform.

Remote sensing platforms, especially satellite platforms, guarantee repetitive measurements, which is essential for both short- and long-term monitoring; in particular, the most important applications are: environmental and territorial monitoring, environmental resources management, meteorology, climate change monitoring, land use monitoring, agriculture and military applications.

The mission that marked the modern development of remote sensing is the Landsat Multispectral Scanner System (MSS), launched in 1972. This first mission was followed by several others which were able to satisfy the various remote sensing applications, such as: Envisat, RADARSAT, RapidEye, MODIS, Copernicus, with its Sentinels, and many more. The basic principles of their operation and data acquisition are the same: the object on the Earth's surface is characterized according to its ability and mode of emitting or reflecting electromagnetic energy.

2.2.1. Electromagnetic energy

Maxwell's law describes electromagnetic radiation as a wave phenomenon composed of an electric field (E) and magnetic field (B), which propagates, in the absence of perturbations, along a straight line. The two fields are perpendicular to each other and normal to the direction of propagation (Figure 2.5).

Three parameters completely describe the wave: wavelength (λ), amplitude (α) and phase (φ). They are, in order, the distance between two crests, the height of the peak and the fraction of deviation of the wave from the origin at the initial time (Figure 2.6).

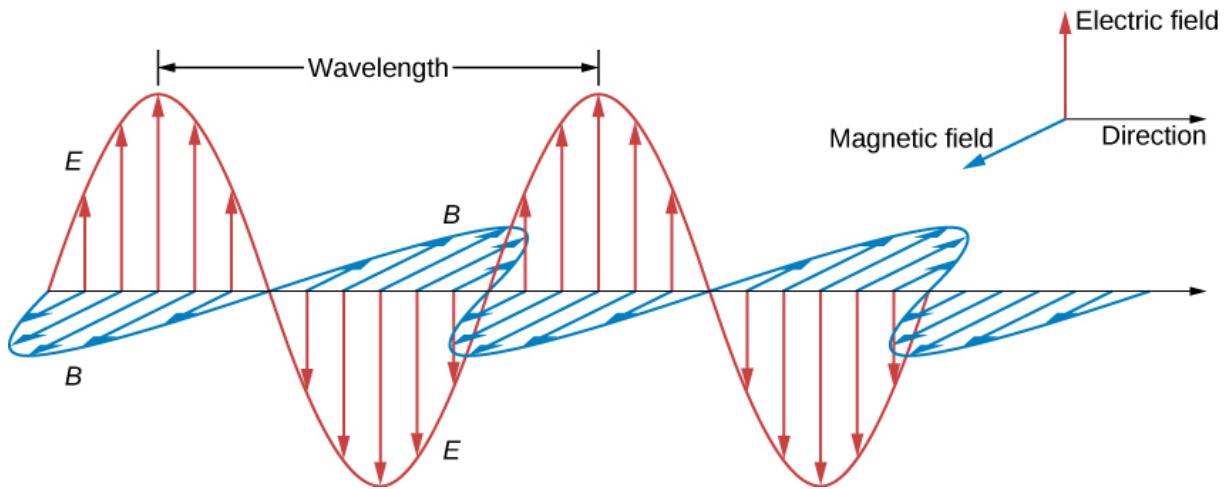


Figure 2.5: The plane wave solution of Maxwell's equations has the B field directly proportional to the E field at each point, with the relative directions shown.

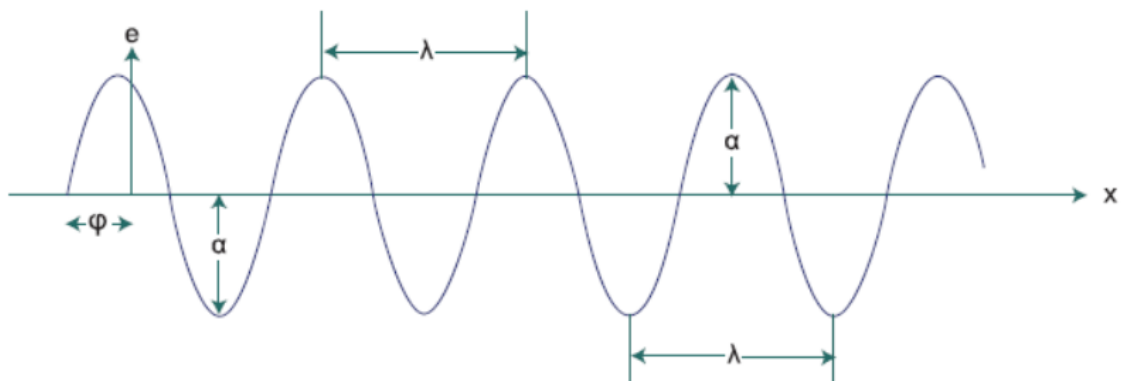


Figure 2.6: Characteristic parameters of the electromagnetic signal.

2.2.2. Electromagnetic spectrum

The wavelength plays a fundamental role in remote sensing: it is according to the characteristics of emission, absorption and transmission of the different wavelengths that it is possible to define the characteristics of an object.

By definition, the electromagnetic spectrum is the set of all possible electromagnetic radiation ordered according to wavelength or frequency. Even if the spectrum is defined as continuous, operationally, a discretization is necessary, i.e. a subdivision into spectral classes identified as: gamma ray, X-ray, ultraviolet ray, visible (a short portion of the electromagnetic spectrum, which corresponds to that perceived by the human eye and is divided into the colours of the rainbow), infrared, microwave and radio waves (Figure 2.7).

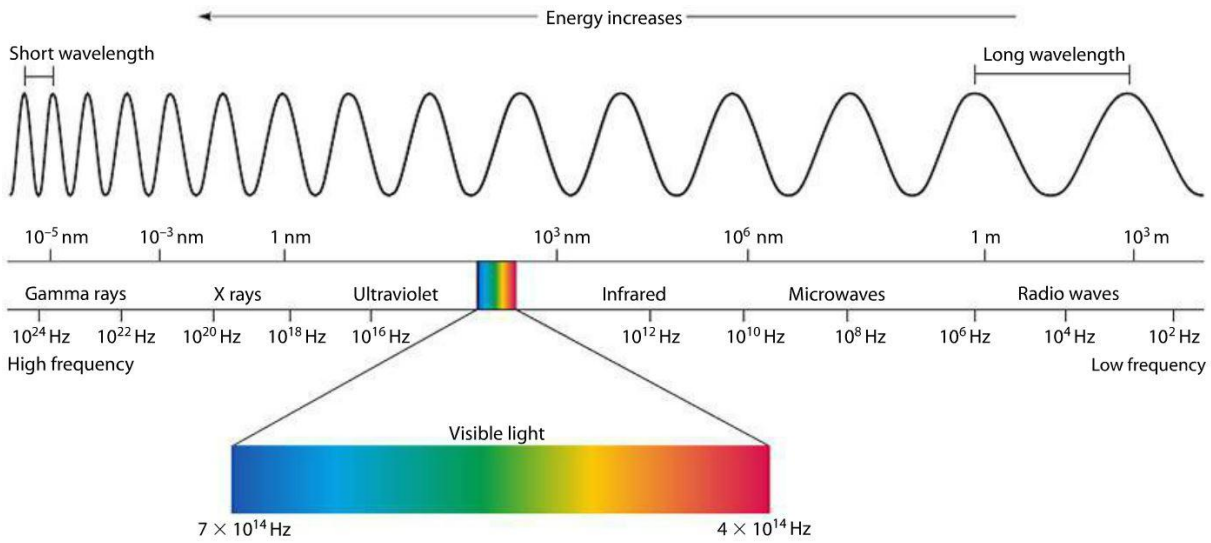


Figure 2.7: Electromagnetic spectrum

2.2.3. Characteristic radiometric parameters for remote sensing

The quantification of the energy emitted or reflected by an object is a fundamental aspect of satellite Earth observation applications.

Kirchoff's law allows quantifying the energy emitted, absorbed and transmitted by a body which, due to the principle of conservation of energy, is:

$$\alpha + \rho + \tau = 1, \quad (2.2)$$

where the parameters are the coefficient of absorption (α), reflection (ρ) and transmission (τ).

The reflection coefficient, or reflectance, is the ratio of reflected radiation (R_s) to incident radiation (I):

$$\rho = \frac{R_s}{I} \quad (2.3)$$

Reflectance makes it possible to identify a specific material uniquely; it is, therefore, a fundamental parameter for remote sensing because it is linked to the chemical-physical characteristics of the surface.

2.2.4. Interaction between solar radiation and the Earth's atmosphere

The Sun is the main source of electromagnetic radiation for the Earth and therefore plays an essential role in remote sensing. With its temperature of 5777 K, it emits electromagnetic radiation in all wavelengths, but mainly in the bands: ultraviolet (UV), visible, near-infrared (NIR), short-wavelength infrared (SWIR), and mid-wavelength infrared (MWIR).

The atmosphere is not homogeneous in altitude but varies in composition, density and temperature, influencing its ability to absorb, transmit and reflect electromagnetic radiation from the Sun. All gas particles and aerosols in the atmosphere interact with solar radiation differently depending on their physical characteristics. The atmospheric effect defines all the phenomena that occur in the atmosphere that modify the propagation speed of the radiation, wavelength, spectral distribution, intensity and path.

The main phenomena to which solar radiation is subjected during its path through the atmosphere are atmospheric refraction, atmospheric absorption and atmospheric dispersion.

Atmospheric refraction is the phenomenon whereby solar radiation undergoes a deviation from its propagation direction due to the passage through the interface with a medium of different density.

Atmospheric absorption is the process by which electromagnetic radiation from the Sun is absorbed by atoms and molecules and transformed into other forms of energy, primarily heat. Every substance in the atmosphere interacts differently with the radiation; for this reason, the absorption bands of the different atoms and molecules have a different and characteristic absorption spectrum. Hence, in some regions of the electromagnetic spectrum, the atmosphere is unclear to the passage of radiation; this is a strong limitation for remote sensing.

Dispersion (scattering) is the phenomenon whereby molecules, particles and water vapour spread electromagnetic radiation in the atmosphere; this mainly depends on the size of the particles and the wavelength.

2.2.5. Interaction between solar radiation and natural surfaces

From a physical point of view, natural surfaces have very different behaviours when hit by electromagnetic radiation. The proportion of absorbed, transmitted and reflected energy

varies according to the chemical-physical characteristics of the materials; the behaviour can be different depending on the wavelength of the radiation to which they are exposed. Land cover identification with remote sensing is based on this principle, which allows the determination of the material based on its spectral signature, i.e. its ability to absorb and reflect the electromagnetic spectrum.

2.2.6. Sensors

The first classification for sensors is based on the acquisition method: if the instrument detects radiation naturally reflected or emitted by the Earth's surface, it is defined as passive; devices that emit a signal and record its return echo are defined as active, such as the SAR (Synthetic Aperture Radar). Given the dependence of the measurements on sunlight, passive sensors can only acquire during the day and, for this reason, are often sun-synchronous; on the contrary, active sensors, by emitting energy themselves, can collect data regardless of the presence of solar energy.

Optical remote sensing works in a range of the electromagnetic spectrum, from the visible (0.4 μm) to the near-infrared, up to the thermal infrared (15 μm). The relevant spectral characteristics for an optical sensor are the number of bands, the width of the bands, the central wavelength of the bands and the sensitivity at the edges of the bands.

Optical sensors are generally described according to their spectral, radiometric and geometric properties.

The radiometric resolution of a sensor is the ability to perceive, encode and distinguish different levels of radiant flux intensity emitted or reflected by the target for a given wavelength. The sensor converts this energy into an electric current, making it possible to determine the level of energy intensity for a single wavelength.

Geometric resolution determines the ability of the sensor to discern between two objects and define their geometry. It varies according to the dimensions of the elementary area on the ground in which the electromagnetic energy is detected.

Each satellite also has a specific temporal resolution, i.e. the period between two successive shots of the same area.

2.3. Satellite data - Overview of Planet Labs satellites

The search for satellite images regarding the mouth of the Ofanto River was carried out through the web Planet platform. Planet Labs PBC is an American public Earth imaging company based in San Francisco, California. Their web platform provides daily satellite images from 2013 to the present day.

As previously said, satellite images have different purposes (mapping, deep learning, environmental and territorial monitoring and many others), so the images are collected and processed in different formats to serve the various use cases.

Planet operates the PlanetScope (PS) and SkySat (SS) Earth-imaging constellations and, before its withdrawal, also the RapidEye (RE) constellation. In addition, the Planet web platform provides access to two other freely available datasets: Landsat 8, managed by the National Aeronautics and Space Administration (NASA) and the United States Geological Survey (USGS); and Sentinel-2, managed by the European Space Agency (ESA). The Planet dataset is also replenished with these additional images provided by third parties because they want to make these products easily available to users to increase their analyses.

2.3.1. PlanetScope satellite constellation

PlanetScope satellite constellation consists of multiple launches of groups of individual satellites. Since the beginning of the mission in 2013, the in-orbit capability has been steadily improving, with technology advancements being implemented at a rapid pace.

The PlanetScope satellites are CubeSat 3U form factor (10 cm by 10 cm by 30 cm). CubeSats are nanosatellites developed since 1999 by California Polytechnic State University and Stanford University; they are miniaturized satellites having a cubic shape with a volume of about 1 cubic decimeters and a mass of about 5.8 kilograms. The PlanetScope constellation has about 130 satellites; they can visualize the entire land surface of the Earth every day (daily collection capacity of approximately 200 million square kilometers per day). This acquisition capacity varies during the seasons due to increased or decreased solar hours; furthermore, they use a sun-synchronous orbit to ensure that the sunlight angle at the Earth's surface is constantly maintained.

PlanetScope satellite images are captured as a continuous strip of single-frame images known as scenes. The first generation of these satellites (called DOVE-C or PS2) captured

a single RGB (red, green, blue) frame. Starting with the November 2018 missions, new satellite generations have sensor characteristics that allow better spectral resolutions. The satellites known as DOVE-R (or PS2.SD) are the second generation of PlanetScope satellites (operational from March 2019 until April 2022), while the SuperDove (or PSB.SD) satellites are the third generation (operational from mid-March 2020). These last ones produce daily images with eight spectral bands (coastal blue, blue, green I, green, red, yellow, red border and near-infrared). All these PlanetScope satellites provide imagery with a resolution of 3–5 meters on the ground; therefore, they have a very high image resolution, allowing them to be employed for many purposes.

Table 2.1 provides an overview of the characteristics of PlanetScope satellites, while Figure 2.8 shows a SuperDove satellite.

Table 2.1: PlanetScope satellite characteristics.

	PlanetScope			
	DOVE-C (PS2)	DOVE-R (PS2.SD)	SuperDove (PSB.SD)	
Operator	Planet Labs	Planet Labs	Planet Labs	
Number of satellites	130+ active now between DOVE-C, DOVE-R and SuperDove (growing)			
Design spacecraft lifetime	2 - 3 years	2 - 3 years	2 - 3 years	
Mass	5.8 kg	5.8 kg	5.8 kg	
Dimensions	0.1 m x 0.1 m x 0.3 m	0.1 m x 0.1 m x 0.3 m	0.1 m x 0.1 m x 0.3 m	
Orbit altitude	450 - 580 km	450 - 580 km	475 - 525 km	
Sun-synchronous orbit	Yes	Yes	Yes	
Global revisit time	Daily at Nadir	Daily at Nadir	Daily at Nadir	
Spatial resolution	3 - 4.1 m	3 - 4.1 m	3.7 - 4.2 m	
Spectral bands	Coastal blue	-	-	431 - 452 nm
	Blue	455 - 515 nm	464 - 517 nm	465 - 515 nm
	Green I	-	-	513 - 549 nm
	Green	500 - 590 nm	547 - 585 nm	547 - 583 nm
	Yellow	-	-	600 - 620 nm
	Red	590 - 670 nm	650 - 682 nm	650 - 680 nm
	Red - Edge	-	-	697 - 713 nm
	NIR	780 - 860 nm	846 - 888 nm	845 - 885 nm

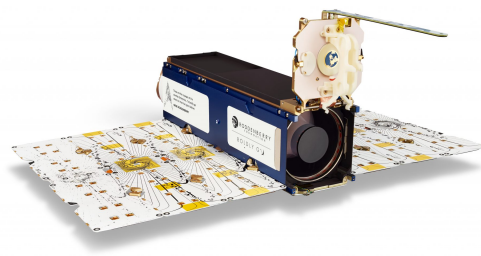


Figure 2.8: SuperDove satellite.

2.3.2. SkySat satellite constellation

SkySat-C generation satellites are very high-resolution Earth imaging satellites; the first SkySat satellite was launched into orbit in 2016. The SkySat-C17, SkySat-C18 and SkySat-C19 satellites are the latest released and were launched into orbit in 2020. The total number of SkySat-C satellites launched amounts to 21.

The SkySat satellites are based on the CubeSat concept, but they are bigger (60 cm by 60 cm by 95 cm) and weigh up to 110 kilograms. According to Planet, their optical instruments produce images of Earth with a resolution of 50 centimetres. All SkySats contain Cassegrain telescopes with a focal length of 3.6 meters, with three 5.5 megapixel CMOS image detectors forming the focal plane. Most of these are sun-synchronous satellites, but six of the C-Generation SkySat satellites (from SkySat-16 to SkySat-21) were launched into non-sun-synchronous orbits to increase the image cadence between 52 degrees northern and southern latitude up to 6-7 times per day on worldwide average, with a maximum of 12 (ESA website).

Table 2.2 provides an overview of the characteristics of SkySat satellites, while Figure 2.9 shows a SkySat satellite.

Table 2.2: SkySat satellite characteristics.

	SkySat		
	SkySat-C 1-15	SkySat-C 16-21	
Operator	Planet Labs	Planet Labs	
Number of satellites	15	6	
Design spacecraft lifetime	6 years	6 years	
Mass	110 kg	110 kg	
Dimensions	0.6 m x 0.6 m x 0.95 m	0.6 m x 0.6 m x 0.95 m	
Orbit altitude	450 km	400 km	
Sun-synchronous orbit	Yes	No	
Global revisit time	4 - 5 days	4 - 5 days	
Spatial resolution	0.5 m	0.5 m	
Spectral bands	Blue	450 - 515 nm	450 - 515 nm
	Green	515 - 595 nm	515 - 595 nm
	Red	605 - 695 nm	605 - 695 nm
	NIR	740 - 900 nm	740 - 900 nm
	PAN	450 - 900 nm	450 - 900 nm



Figure 2.9: SkySat satellite.

2.3.3. RapidEye satellite constellation

Rapid Eye was a five-satellite that Planet acquired from the German company BlackBridge in 2015 and retired officially in April 2020.

Their dimensions were less than 1 cubic meter and they weighed about 150 kilograms. All these satellites orbited at the same altitude of 630 kilometres above the Earth; they could travel 4 million kilometres per day with an image resolution of 5 meters on the ground. They were equipped with a multi-spectral sensor that enabled them to acquire 5-band colour imagery every day.

Table 2.3 provides an overview of the characteristics of RapidEye satellites, while Figure 2.10 shows a RapidEye satellite.

Table 2.3: RapidEye satellite characteristics.

RapidEye		
Operator	Retired	
Number of satellites	5	
Design spacecraft lifetime	7 years	
Mass	156 kg	
Dimensions	0.8 m x 0.9 m x 1.2 m	
Orbit altitude	630 km	
Sun-synchronous orbit	Yes	
Global revisit time	Daily (off-nadir) / 5.5 days (at nadir)	
Spatial resolution	5 m	
Spectral bands	Blue	440 – 510 nm
	Green	520 – 590 nm
	Red	630 – 685 nm
	Red - Edge	690 – 730 nm
	NIR	760 – 850 nm

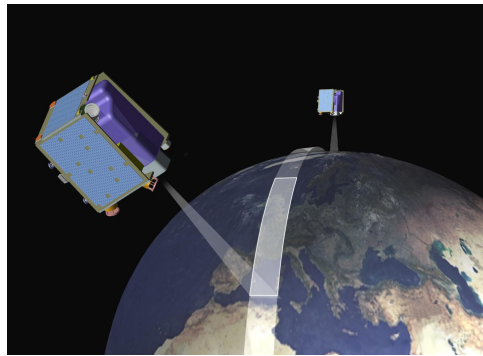


Figure 2.10: RapidEye satellite.

2.3.4. Landsat 8 satellite

The American Landsat satellite was launched into orbit in February 2013 and began operating in March of the same year. It is the eighth (of nine) satellites in the NASA and USGS Landsat program. The American Landsat program began in 1972 and has provided fundamental data for numerous scientific initiatives, particularly for monitoring climate change.

Landsat 8 is a sun-synchronous satellite which orbits at an altitude of 705 kilometres from

the Earth and takes 99 minutes to complete the whole orbit. In this way, he manages to acquire about 740 scenes per day.

The satellite carries the Operational Land Imager (OLI) and the Thermal Infrared Sensor (TIRS) instruments. The OLI measures in the visible, near-infrared, and shortwave infrared portions (VNIR, NIR, and SWIR) of the spectrum. The TIRS measures land surface temperature in two thermal bands with a new technology that applies quantum physics to detect heat.

Landsat 8 images have 15-meter panchromatic and 30-meter multi-spectral spatial resolutions; instead, as regards the images obtained by TIRS, they have a spatial resolution of 100 meters.

Table 2.4 provides an overview of the characteristics of the Landsat 8 satellite, while Figure 2.11 shows the Landsat 8 satellite.

Table 2.4: Landsat 8 satellite characteristics.

Landsat 8	
Operator	NASA - USGS
Number of satellites	1
Design spacecraft lifetime	> 10 years
Mass	2071 kg
Length	3 m
Diameter	2.4 m
Orbit altitude	705 km
Sun-synchronous orbit	Yes
Global revisit time	16 days
Spatial resolution	15 - 30 - 100 m
	Coastal blue 430 - 450 nm
	Blue 450 - 510 nm
	Green 530 - 590 nm
	Red 640- 670 nm
Spectral bands	NIR 850 - 880 nm
	SWIR 1 1570 - 1650 nm
	SWIR 2 2110 - 2290 nm
	PAN 500 - 680 nm
	Cirrus 1360 - 1380 nm



Figure 2.11: Landsat 8 satellite.

2.3.5. Sentinel-2 satellite constellation

The Copernicus Sentinel-2 mission is based on a constellation of two identical satellites in the same orbit. The Copernicus programme, formerly known as Global Monitoring for Environment Security (GMES), was born in 1998 as an initiative of the European Commission, European Space Agency (ESA) and European national space agencies. Copernicus is overseen by the European Commission, which defines and develops the political vision of the program and coordinates it in order to maintain the correct and adequate functioning of the system. The European Commission is also responsible for the long-term financing of the project.

The Sentinel-2 mission began in June 2015 with the launch of the optical imaging satellite called Sentinel-2A; in March 2017, a second satellite, Sentinel-2B, was launched into orbit. A third satellite, Sentinel-2C, is currently undergoing testing in preparation for launch in 2024.

Both satellites are sun-synchronous and orbit around the Earth at about the same altitude of 786 kilometres, but 180° apart. The ensured coverage of the mission includes all continental lands between latitudes 56° S and 84° N, the seas up to 20 kilometres from the coasts, the Mediterranean Sea and all enclosed seas.

The two satellites are equipped with multi-spectral optical sensors with 13 bands at different spatial resolutions. The span of 13 spectral bands, from the visible and the near-infrared to the shortwave infrared (VNIR, NIR, and SWIR) at different spatial resolutions ranging from 10 to 60 meters, takes land monitoring to an unprecedented level. Table 2.5 provides an overview of the characteristics of the Sentinel-2 satellites, while Figure 2.12 shows the Sentinel-2A satellite.

Table 2.5: Sentinel-2 satellite characteristics.

	Sentinel-2		
	Sentinel-2A	Sentinel-2B	
Operator	ESA	ESA	
Number of satellites	1	1	
Design spacecraft lifetime	> 7 years	> 7 years	
Mass	1016 kg	1016 kg	
Dimensions	3.4 m × 1.8 m × 2.35 m	3.4 m × 1.8 m × 2.35 m	
Orbit altitude	786 km	786 km	
Sun-synchronous orbit	Yes	Yes	
Global revisit time	10 days	10 days	
Spatial resolution	10 - 20 - 60 m	10 - 20 - 60 m	
Spectral bands	Coastal blue	432 - 453 nm	432 - 453 nm
	Blue	459 - 525 nm	459 - 525 nm
	Green	542 - 578 nm	542 - 578 nm
	Red	649 - 680 nm	649 - 680 nm
	Red - Edge	697 - 792 nm	697 - 792 nm
	NIR	780 - 886 nm	780 - 886 nm
	SWIR 1	1568 - 1659 nm	1563 - 1657 nm
	SWIR 2	2115 - 2290 nm	2094 - 2279 nm
	Cirrus	1358 - 1389 nm	1362 - 1392 nm



Figure 2.12: Sentinel-2A satellite.

Table 2.6 shows a summary of the different spatial resolutions of the five satellite classes described.

Table 2.6: Various spatial resolutions of the described satellites.

	Spatial resolution [m]
PlanetScope	3 - 4.2
SkySat	0.5
RapidEye	5
Landsat 8	15 - 30 - 100
Sentinel-2	10 - 20 - 60

2.4. Satellite images and plume patterns for the case study

2.4.1. Satellite images research

For the case study, the images at the mouth of the Ofanto River, which showed the phenomenon of the river plume into the sea, were searched on the Planet website. The agreed time period of the research goes from July 1 2019 to March 31 2021; therefore, the images available from this period were checked day by day. The Planet website allows to select a specific area of interest over the whole Earth's map and the time interval to search for images. Figure 2.13 shows an example of an image search by location and date on the Planet website. In the image, it can be seen that in the selected search area (in this specific case, it is a quadrangular area with the site of interest in the centre) the satellite image available day by day appears. Furthermore, the images are described in detail because they report: the satellite they come from, their spatial resolution, the snapping time (UTC+0), the percentage ratio between the selected area and the area covered by the image available, the percentage of cloud cover and the elevation of the Sun (in degrees).

The main problems when carrying out searches based on satellite images are two: the first one is the passage or not of satellites over the area of interest in the specified time, and the second one, especially as regards the search for images using satellites with passive optical sensors, the presence of clouds in the sky above the area of interest. The first problem is much less frequent because more and more research satellites are in the skies nowadays. On the other hand, the problem of cloud cover is widespread, especially in the search for events such as the one dealt with in this thesis.

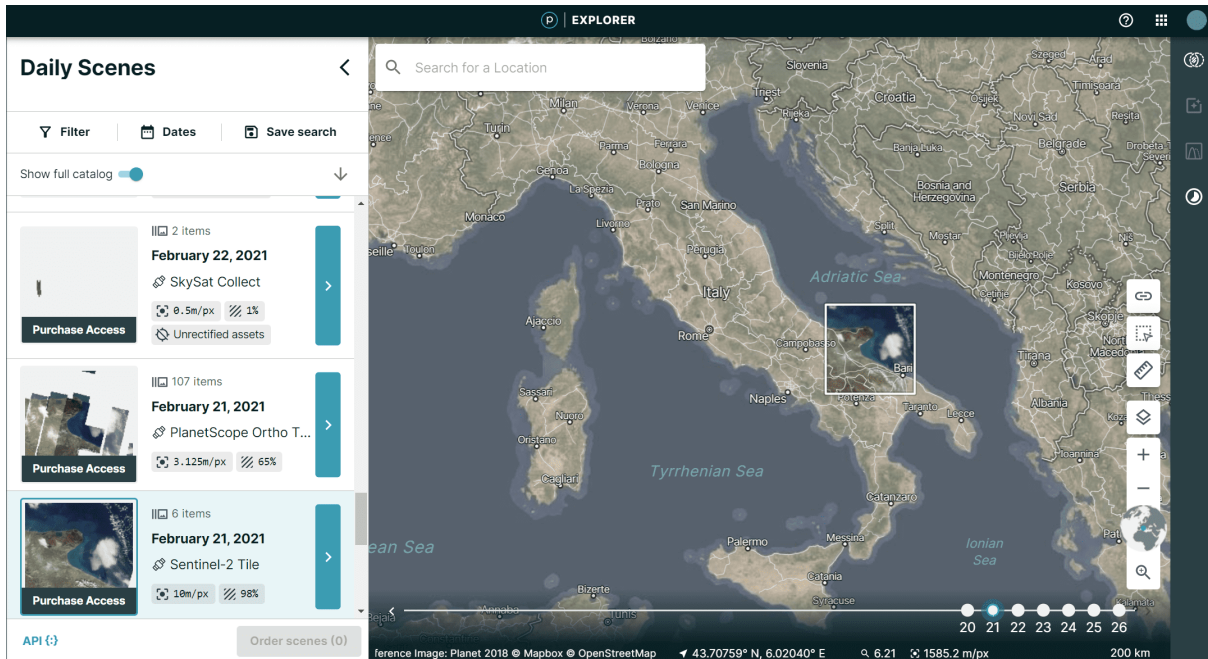


Figure 2.13: Example of image search on the Planet website.

As mentioned in the previous paragraphs, the fluvial plume mainly occurs because of the triggering of the transport of solids in suspension caused, most of the time, by high river flow rates. The Ofanto River has a torrential nature and is not fed by glaciers, therefore, its flow rate depends exclusively on atmospheric precipitation. Thus, the phenomenon of the plume for the Ofanto River occurs only after a period of rain or when the flow rates increase and the suspended solid transport of the soil material starts. It has been verified that a highly developed and persistent plume is created only after extreme precipitation events; therefore, for this river, the plume's extension, size and duration over time are related to its flow rate.

In the reference period (July 1, 2019 - March 31, 2021), the clear images of the river plume events are not several, both because it is possible that the satellites did not acquire images on the days of the phenomenon and because of clouds cover the Earth's surface in the area of interest (mainly for this reason).

In the reference period, 19 plumes were found at the mouth of the Ofanto River. In most cases, the plumes are not very extensive, but persist for a period ranging from 2 to 4 days, especially in the near-field area of the plume. There are two main reasons why the plumes at the mouth of the Ofanto River are almost always not very extensive but persistent:

1. There are very few images of the river plume after high rainfalls (which consequently result in high flows), because at the most extreme events, almost always, the clouds

of the perturbation cover the Earth's surface in the area of interest; consequently, many images portray plumes caused by not excessively high and long-lasting rainfalls.

2. The tidal phenomenon in this area of the Southern Adriatic Sea (Apulian coast) is not excessively strong (Figure 2.20, Section 2.4.2); therefore, it does not decisively affect the plume, i.e. it does not act dispersion and dismantling of the plume at each change of tide.

The 17 images showing the fluvial plume phenomenon are reported in Appendix A, with attached image documentation (time, satellite, spatial resolution). Figure 2.14 shows an example of a medium-small fluvial plume of the Ofanto River (image taken by Dove Classic (PS2) on December 16, 2019). In this image, the Tidal Plume Front (area near the mouth) and the mid-field area (beyond the TPF) are clearly distinguishable.



Figure 2.14: Example of satellite image capturing the Ofanto River plume (image taken by Dove Classic (PS2) on December 16, 2019, with a pixel resolution of 3 meters).

2.4.2. Hydro-meteorological data

Rainfall data

To understand when the precipitation events occurred, the rainfall data (provided by Arpa Puglia) of the measurement station closest to the Ofanto River mouth (i.e. that of Barletta) are downloaded.

The Arpa Puglia Weather Service collects and validates the weather data of the Telemeasurement Network, made up of 5 automatic stations located at its provincial offices of Arpa Puglia and 19 weather stations belonging to the Regional Air Quality Network (RRQA). The temperature and precipitation parameters are validated according to "Guidelines for checking the validity of hydro-meteorological data", elaborated within the Italian National System for the Protection of the Environment.

Figure 2.15 shows the 24 weather stations of Arpa Puglia, in particular, the Barletta weather station is drawn in red.

The graph in Figure 2.16 shows the daily rainfall recorded by the Barletta weather station rain gauge from July 1, 2019, to March 31, 2021, in which intense rainfall events are noted interspersed with long periods of absence of rain (especially in 2020). The average daily rainfall on these dates is 1.36 millimetres, with a maximum of 20 millimetres occurring

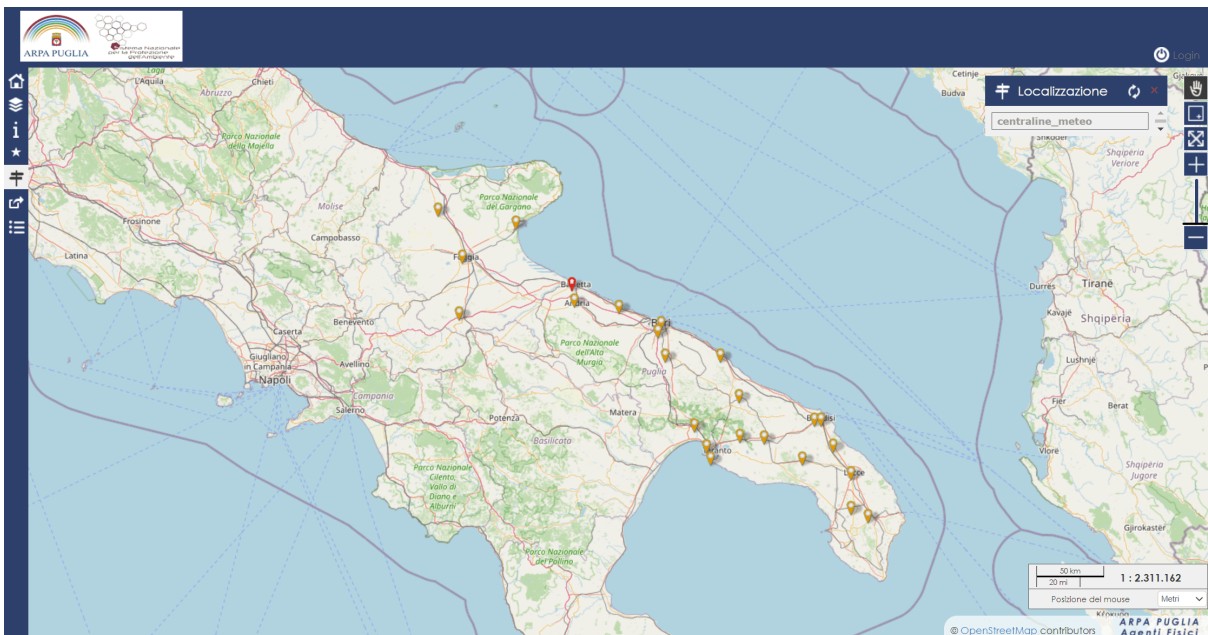


Figure 2.15: Location map of Arpa Puglia weather station (Barletta weather station in red).

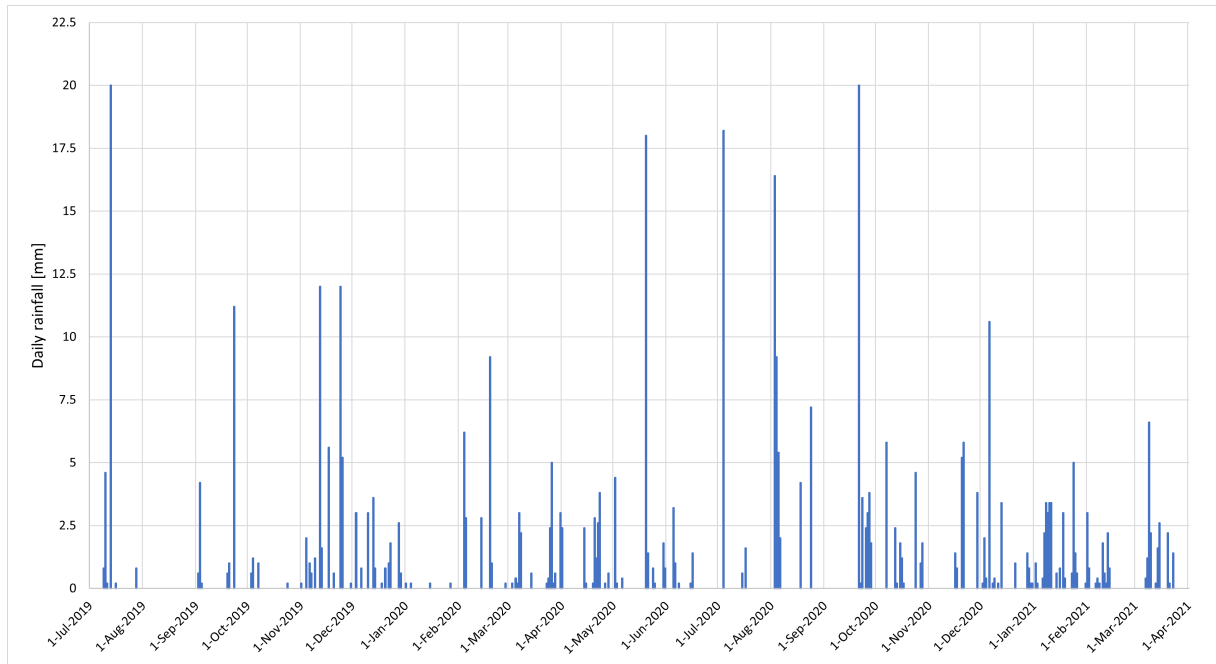


Figure 2.16: Barletta weather station (daily rainfall).

on July 13, 2019, and September 21, 2020. From this preliminary data, it was possible to understand the days on which a possible fluvial plume phenomenon should or should not have been expected.

Ofanto River discharge

The fluvial flow rate is crucial data for the realisation or otherwise of the fluvial plume phenomenon because, as reported in the literature, it is the determining factor for mobilising suspended solids and plume formation. In most cases, and also for the Ofanto River plume, as will be seen, larger discharges create more prominent and more persistent fluvial plumes, while smaller discharges can create small fluvial plumes (or not at all).

The Decentralised Functional Center (CFD), hinged on the Civil Protection Section of the Puglia Region, makes available to the public, upon request, the hydrological data not yet published in the Annals; they are distributed free of charge to public institutions, research centres, universities.

The stream gauging stations available in the Puglia Region are shown in Figure 2.17; in particular, those on the Ofanto River are marked in red.

The stream gauging station of San Samuele di Cafiero is the closest to the river mouth, about 18 km inland. For this measuring station, the flow rate and water level were requested for the entire time interval of the study. These data are reported in the graph

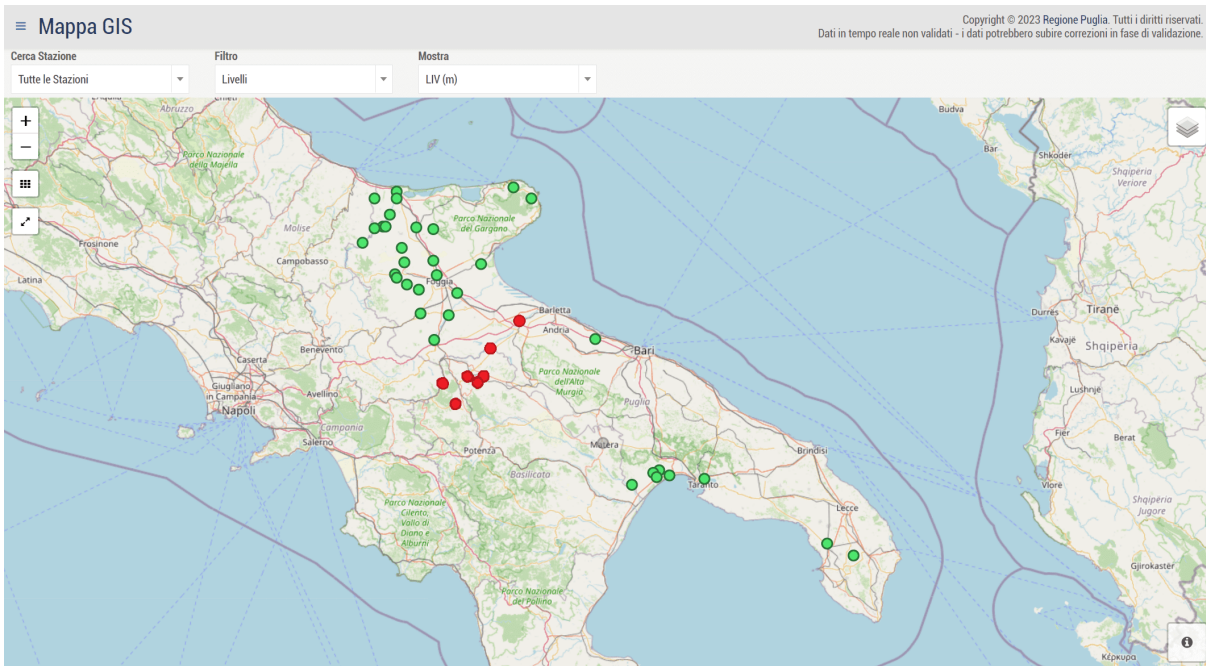


Figure 2.17: Puglia Civil Protection stream gauging stations (Ofanto River stations in red).

of Figure 2.18. In this period, the average flow rate was 8.13 cubic meters per second, while the average water level was 0.71 metres.

Figure 2.18 shows that the highest flow rate, equal to 262 cubic meters per second, corresponding to a water level of 4.56 metres, was recorded on September 13, 2020, at 09:30 in the morning. However, data reported for this event are probably affected by measurement errors because the September 12-13-14, 2020 satellite images show clear skies and no fluvial plume shapes. This data is also confirmed by the rainfall data from the Barletta weather station, which did not record any rain on those days. Furthermore, the flow rate data for September 13, 2020, records this sudden peak, after which it does not report any data again for two consecutive days.

The second largest flow rate value reported in the graph of Figure 2.18 is that of March 11, 2021, caused by the rain event of March 9, 2021. The maximum flow recorded for this event is 203.2 cubic meters per second (March 11, 2021, at 02:00), corresponding to a water height of 4.14 metres. The best fluvial plume image of the entire analysed period is linked to this event, and the fluvial models developed in this thesis were based on that.

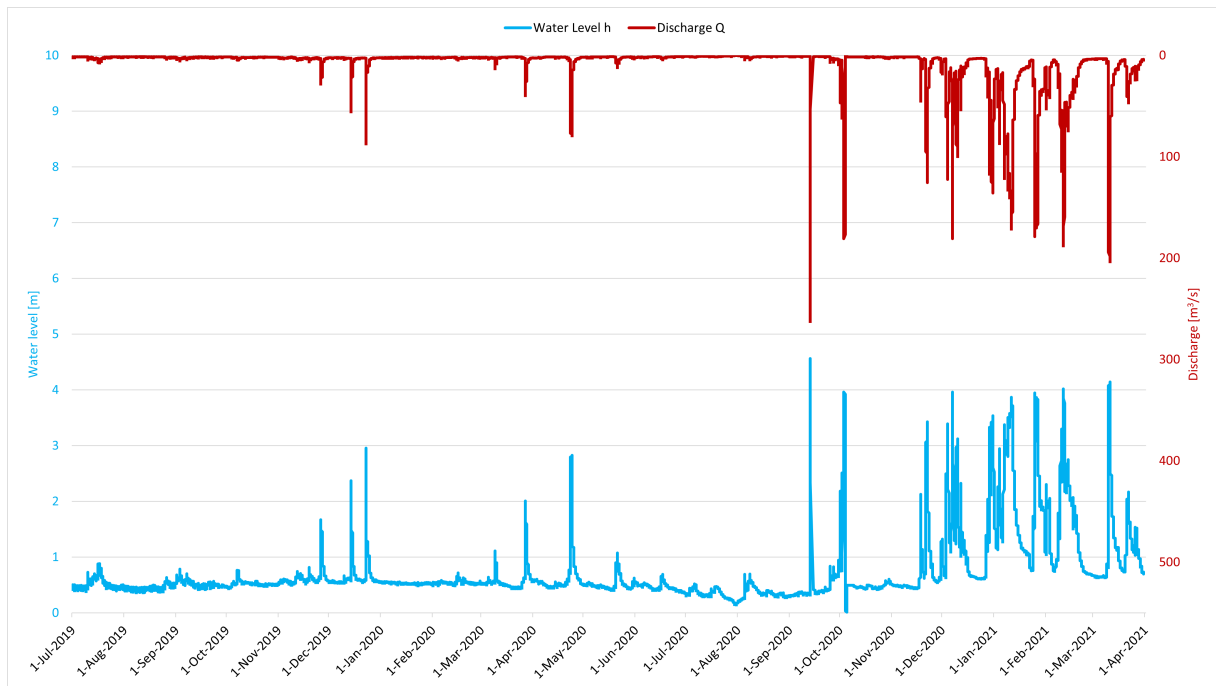


Figure 2.18: Water level and discharge recorded at the San Samuele di Cafiero stream gauging station from 1 July 2019 to 31 March 2021.

Tidal data

The tide affects the formation and persistence of the plume; in particular, it can play a fundamental role in the hydraulic phenomena that occur in the near-field area. In some cases, the ebb and flood tide trend can also influence the far-field area, as explained in Section 2.1.

In Italy, the National Mareographic Service (Servizio Mareografico Nazionale, SMN) manages tidal data, which has the task of carrying out the systematic survey and processing data relating to the maritime climate, the state of the coasts and sea water levels, to provide for the systematic publication of the elements observed and elaborated elements, and cartography, and to prepare criteria, methods and standards for the collection, analysis and consultation of data. The SMN provides data, opinions and advice to anyone who requests it and supports local and public authorities.

In the maritime field, the SMN has taken over the management of the National Wave Measurement Network (Rete Ondametrica Nazionale, RON), created by the Ministry of Public Works, and has provided for the development and strengthening of the new National Mareographic Network (Rete Mareografica Nazionale, RMN). The National Mareographic Network comprises 36 measuring stations uniformly distributed throughout the country and mainly located within the port structures (Figure 2.19). The tidal stations



Figure 2.19: Rete Mareografica Nazionale measuring stations (Bari in orange and Vieste in greenish).

closest to the case study area are those of Vieste and Bari. The Vieste tidal station is 59 km north of the mouth of the Ofanto river, while the measurement station of Bari is 61 km South.

As shown in Figure 2.20, the mean tidal range in the Southern Adriatic Sea between Bari and Vieste is about 0.5 meters, consequently, it is a non-negligible value for the study. This weaker tide does not decisively affect the Ofanto River plume, i.e. it does not act dispersion and dismantling of the plume at each change of tide as instead happens in specific examples of literature (River Teign at the English Channel, Columbia River on the coast of the Pacific Ocean) reported in Section 2.1, in which the mean tidal ranges were larger and, therefore, the tide played a key role in the dispersion of the river plume.

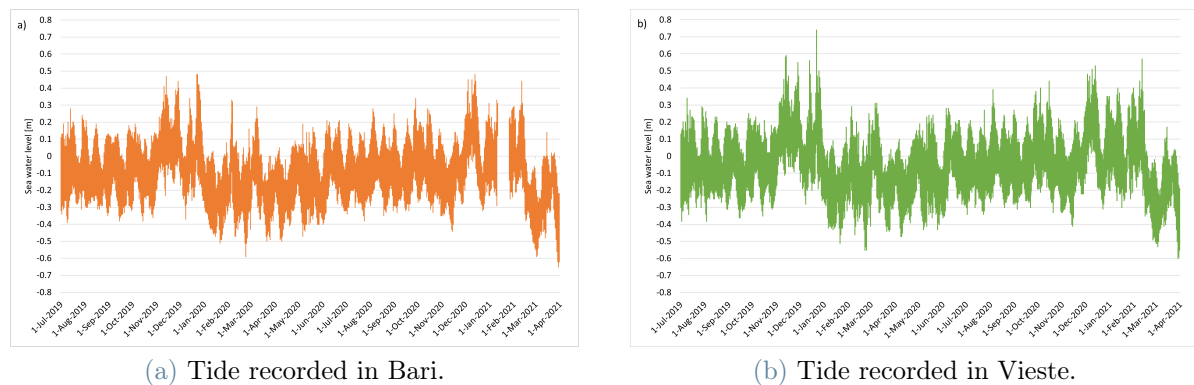


Figure 2.20: Tides recorded in Bari and Vieste from 1 July 2019 to 31 March 2021.

ECMWF re-analysis data (ERA5)

Further useful data to understand the development of the fluvial plume are wind data, wave height and direction and seawater temperature.

Wind data are available and distributed upon request by the Decentralised Functional Center of the Civil Protection of the Puglia Region, but the closest measuring station (in Barletta) has started recording anemometric data since May 2022, while the other anemometric stations nearby (Andria, Bisceglie and Manfredonia) have data that do not cover the whole period.

The data regarding the waves and the sea temperature are not available through wave measurement stations (managed by the National Mareographic Network) because the only reference station for the Southern Adriatic Sea is in Monopoli, however active only since May 2021.

These missing data were acquired thanks to the ERA5 re-analysis product, released by ECMWF (European Center for Medium-Range Weather Forecasts) as part of Copernicus Climate Change Services. ERA5 is the fifth generation ECMWF re-analysis for the global climate and weather.

To carry out the re-analysis, a principle called data assimilation is performed, which, relying on the laws of physics, combines the model data with observations from all over the world in a complete and globally coherent dataset. Numerical weather forecasting centres are based on this method: they combine a previous forecast (of previous hours) with new observations available in an optimal way to produce a new, more acceptable, estimate of the state of the atmosphere, called analysis, from which an updated and improved forecast is given. Re-analysis works in the same way, but it does not have to issue timely forecasts and therefore has more time to collect observations, all to the

advantage of the quality of the final product.

ERA5 provides hourly estimates for a large number of atmospheric, ocean waves and land surface quantities. Data has been gridded to a regular lat-lon grid of 0.25 degrees for the re-analysis and 0.5 degrees for the uncertainty estimate.

Wind, wave height, wave direction, and sea temperature data were downloaded from the ERA5 website. These correspond to data extracted 10 km offshore the Ofanto River mouth. The data are distributed in NetCDF format; therefore, an algorithm (Appendix A.18) was developed in Matlab environment to make them readable on a text document.

Wind data are downloaded as "10m u-component of wind" and "10m v-component of wind":

- u is the eastward component of the 10m wind, it is the horizontal speed of air moving towards the east, at the height of ten meters above the surface of the Earth, in meters per second;
- v is the northward component of the 10m wind, it is the horizontal speed of air moving towards the north, at the height of ten meters above the surface of the Earth, in meters per second.

The data concerning the waves are downloaded as "Significant height of combined wind waves and swell" (H_0) and "Mean wave direction" (θ_m):

- H_0 (in meters) is the average height of the highest third of surface ocean/sea waves generated by wind and swell; it represents the vertical distance between the wave crest and the wave trough. The ocean/sea surface wave field combines waves with different heights, lengths and directions (known as the two-dimensional wave spectrum). The wave spectrum can be decomposed into wind-sea waves, which are directly affected by local winds, and swell, the waves generated by the wind at a different location and time. This parameter takes account of both. More strictly, this parameter is four times the square root of the integral over all directions and all frequencies of the two-dimensional wave spectrum.
- θ_m is the average ocean/sea surface wave direction. The units are degrees true, which means the direction relative to the geographic location of the north pole; it is the direction that waves are coming from, so 0 degrees are waves that are coming from the north and 90 degrees are waves that are coming from the east.

Sea temperature data are downloaded as "Sea surface temperature", expressed in kelvin

(K).

2.4.3. Plume patterns and correlations

Thanks to the acquired data and the satellite images found, it is possible to understand how the flow rate, winds, tides and waves influence the plume of the Ofanto River.

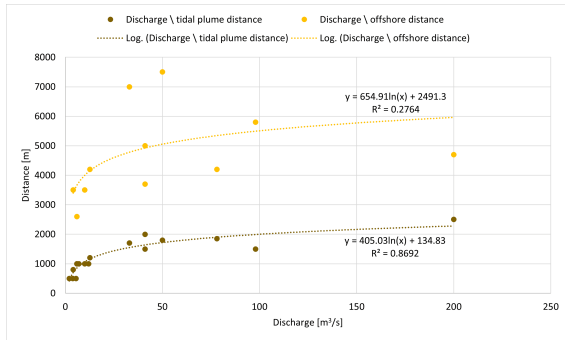
Table 2.7 shows the indicative direction of the plume and the correlations with the acquired data. Figure 2.21a and Figure 2.21b show the correlations between plume distance and flow rate (the first one) and plume distance and water level (the second one).

By measuring the tidal distance plume front, a good logarithmic correlation ($R^2 = 0.869$) was found with the river discharge, i.e. the more the discharge increases, the more the distance and the size of the plume increase, above all it is evident with not excessively high flows. The same result can be found by considering the water level ($R^2 = 0.866$) instead of the flow rate.

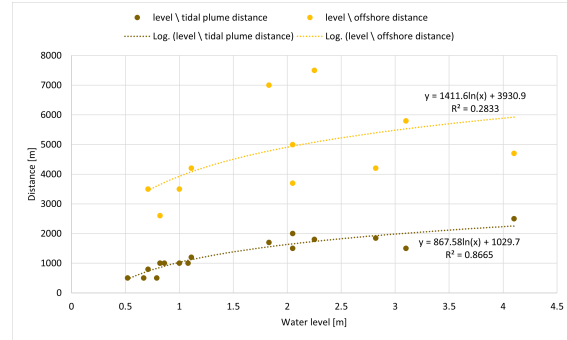
By measuring the plume offshore distance (the most offshore point that the plume can reach in the image), a correlation was not found with the river discharge or with the water

Table 2.7: Plumes directions and correlations with acquired data.

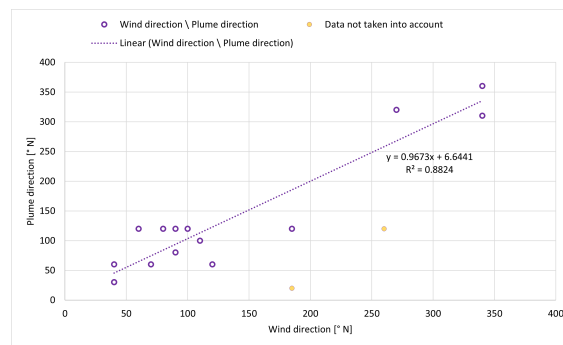
Date	Plume direction [°N]	Tidal plume front distance [m]	Offshore distance [m]	Discharge [m ³ /s]	Water level [m]	Wind direction [°N]	Tide	Mean wave direction [°N]
16/12/2019	310° ↖	1000	2600	6	0.82	340° ↖	ebb	300° ↖
25/12/2019	60° ↗	1000	3500	10	1	120° ↘	ebb	150° ↘
29/3/2020	120° ↘	1000	-	6	0.82	100° →	ebb	140° ↘
24/4/2020	120° ↘	1850	4200	78	2.82	80° →	ebb	300° ↖
25/4/2020	120° ↘	1000	-	12	1.08	90° →	ebb	90° →
26/4/2020	120° ↘	500	-	5.5	0.79	60° ↗	ebb	70° →
27/4/2020	120° ↘	500	-	3.8	0.67	260° ←	ebb	270° ←
22/5/2020	20° ↗	1000	-	7	0.86	185° ↓	flood	185° ↓
23/5/2020	320° ↖	800	3500	4	0.71	270° ←	flood	160° ↓
25/5/2020	120° ↘	500	-	2	0.52	185° ↓	ebb	185° ↓
5/12/2020	360° ↑	1800	7500	50	2.25	340° ↑	ebb	320° ↖
10/12/2020	30° ↗	1500	5800	98	3.1	40° ↗	flood	40° ↗
14/1/2021	60° ↗	1700	7000	33	1.83	40° ↗	flood	200° ↓
19/1/2021	60° ↗	1200	4200	12.7	1.11	70° ↗	ebb	170° ↓
3/2/2021	30° ↗	2000	5000	41	2.05	40° ↗	ebb	340° ↖
18/2/2021	80° →	1500	3700	41	2.05	90° →	ebb	150° ↘
11/3/2021	100° →	2500	4700	200	4.1	110° ↘	ebb	190° ↓
						15 out of 17	13 out of 17	10 out of 17



(a) Correlations between discharge and plume distances.



(b) Correlations between water level and plume distances.



(c) Correlation between wind direction and plume direction.

Figure 2.21: Correlations between acquired data and plume direction.

level; this is because the wind plays a fundamental role in the mid-field and the far-field, therefore many results can be affected by more decisive wind action in an offshore or inshore direction. However, it is possible to note a poor correlation ($R^2 = 0.276$) which confirms that the discharge (and water level) affects the plume size. It is clear, therefore, that the discharge plays a fundamental role in the size and distance of the Ofanto River plume.

Table 2.7 and Figure 2.21c show the correlation between plume direction and wind direction. By analysing the direction of each plume and relating it to the wind data, it is found the confirmation of what was previously reported in the literature in Section 2.1, i.e. that the wind strongly influences the direction of the plume. In the cases under examination, the wind plays the leading role in the direction of the plume, which is always directed like the blowing wind. A linear correlation was found between the direction of the fluvial plume and the direction of the wind. Only twice out of the seventeen did the wind blow in the opposite direction; moreover, on these two occasions (in yellow in Figure 2.21c), the plumes were very small and did not have mid-field and far-field but only near-field;

thus, it was the tide that played the leading role in those cases.

From these analyses, it is clear that the wind plays a fundamental role in the direction of the Ofanto River plume.

The tide does not often influence the direction of the plume, although it always plays a fundamental role in the near-field and in the creation of tidal plume front. It plays a more significant role in dispersing plumes when flow rates are relatively low. It was noted that the Ofanto River plume thirteen times out of seventeen changed direction according to ebb or flood tide. Ebb tides tended to affect by setting a Southeast direction to the plume, while flood tides a North-West direction. However, the tide does not condition the direction of the more extensive plumes, in which the wind and the action of the Earth's rotation dominate.

It can therefore be seen that the tide (not excessively strong in this area of the Adriatic Sea) plays a secondary role as regards the direction of the Ofanto River plume; however, it is essential to consider it because it affects the plume near-field.

As for the mean wave direction, the data confirm the literature, i.e., the direction of the waves does not predominantly affect the plume, even if further studies in the literature need to be performed.

April 24, 2020, event

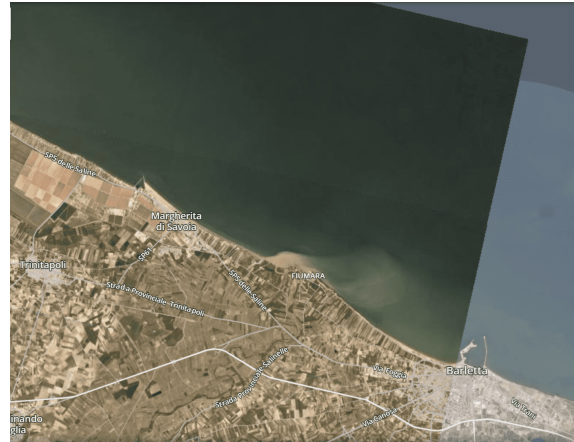
An example of the Ofanto River plume is shown in Figure 2.22 in which the evolution of the plume over a period of four consecutive days (24-25-26-27 April 2020) is visible. Discharges, tides, wind direction and mean wave direction data are shown in the graphs of Figure 2.23.

On April 24, 2020, the plume was very extended offshore due to the precipitation event that occurred between April 20 and 23, 2020, which caused an increase in river discharge with the consequent mobilisation of suspended solid sediments. The peak discharge (78.7 cubic meters per second), linked to this precipitation event, occurs on April 24 2020, at 02:00 at San Samuele di Cafiero's stream gauging station (about 18 kilometres inland), after which the flow rate decreases until it stabilised at about 3.5 cubic meters per second over the next few days.

From the satellite image of this day, it can be seen how the plume can be identified as a prototypical plume: the tidal plume front, the mid-field area and the far-field area in which the inner front and the outer front are well identifiable. The plume extends up to 4 kilometres offshore and the far-field extends in a southeast direction well beyond the port



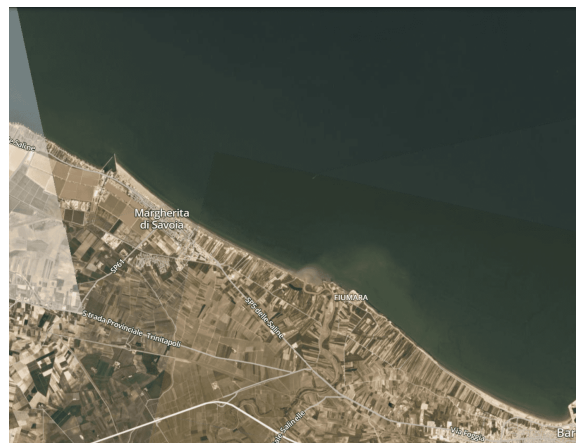
(a) Date: April 24, 2020, at 09:40. Instrument: Sentinel-2B. Pixel resolution: 10 meters.



(b) Date: April 25, 2020, at 09:27. Instrument: Dove Classic (PS2). Pixel resolution: 3 meters.



(c) Date: April 26, 2020, at 09:25. Instrument: Dove Classic (PS2). Pixel resolution: 3 meters.



(d) Date: April 27, 2020, at 09:27. Instrument: Dove Classic (PS2). Pixel resolution: 3 meters.

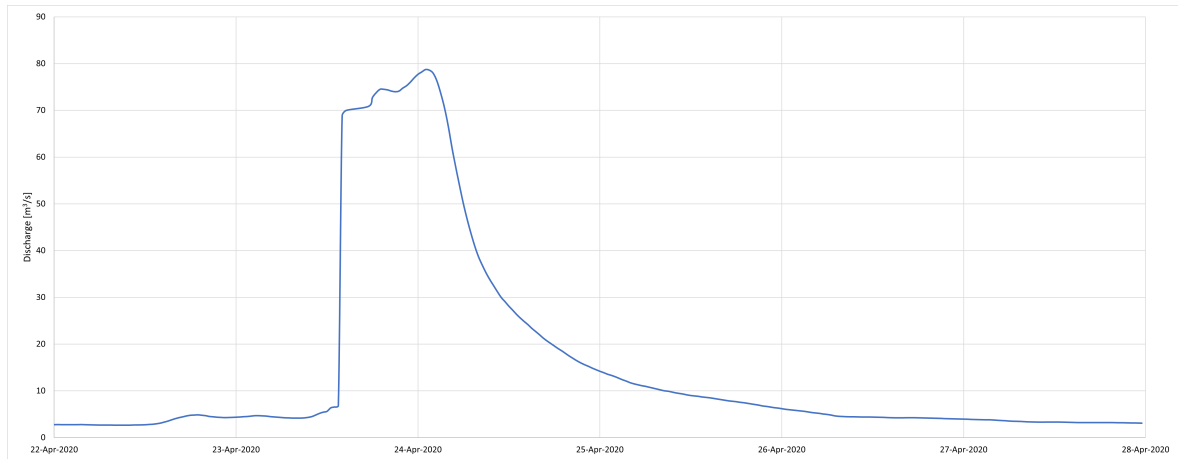
Figure 2.22: Satellite images captured on 24, 25, 26, 27 April 2020.

of Barletta (a distance greater than 10 kilometres); this direction is strongly conditioned by the wind, in fact, that morning it blew in an easterly direction (about 60° N).

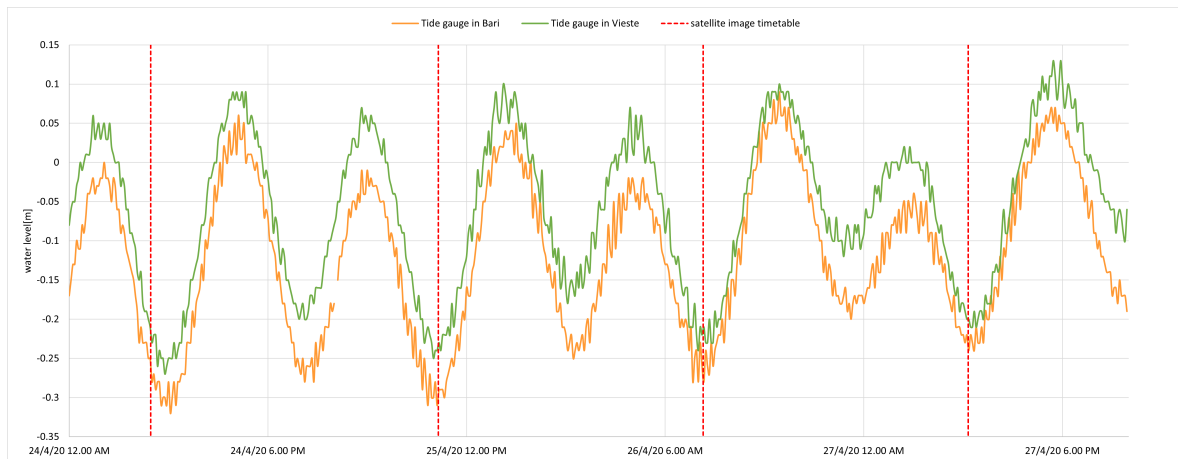
On the other hand, the direction of the waves does not seem to play a crucial role in this event.

During 25-26-27 April 2020, after the rainfall event, the discharge started to drop; hence the freshwater arrived in the near-field area of the plume with too little energy to be able to reach the mid-field (dominated by higher salinity concentrations). The decrease in flow rate caused the suspended sediments to remain more concentrated in the near-field area (near the river mouth) without undergoing a consistent effect of the tide, which in those days was relatively weak (mean tidal range of 0.3 meters or less). The concentration and extent of the plume continued to decrease because of lower discharges (less suspended

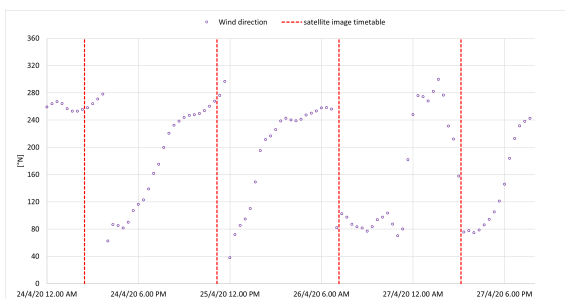
solid material), wind and alongshore current effects, which dispersed the fluvial plume in a south-easterly direction (toward the port of Barletta and the neighbouring coastal areas).



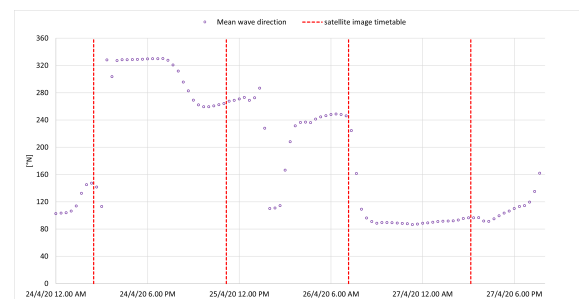
(a) Discharge at San Samuele di Cafiero from April 22, 2020 to April 27, 2020.



(b) Tides recorded in Bari and Vieste.



(c) Wind direction near the river mouth (data from ERA5).



(d) Mean wave direction near the river mouth (data from ERA5).

Figure 2.23: Discharge, tides, wind direction and mean wave direction referring to the river plume event of April 24, 2020.

March 11, 2021, event

A second example of a river plume is shown in Figure 2.24; it represents the most significant event of the entire research, which occurred on March 11, 2021. No additional images of this river plume are available because, in the days before and after March 11 2021, the clouds are too thick to observe the image on the ground.

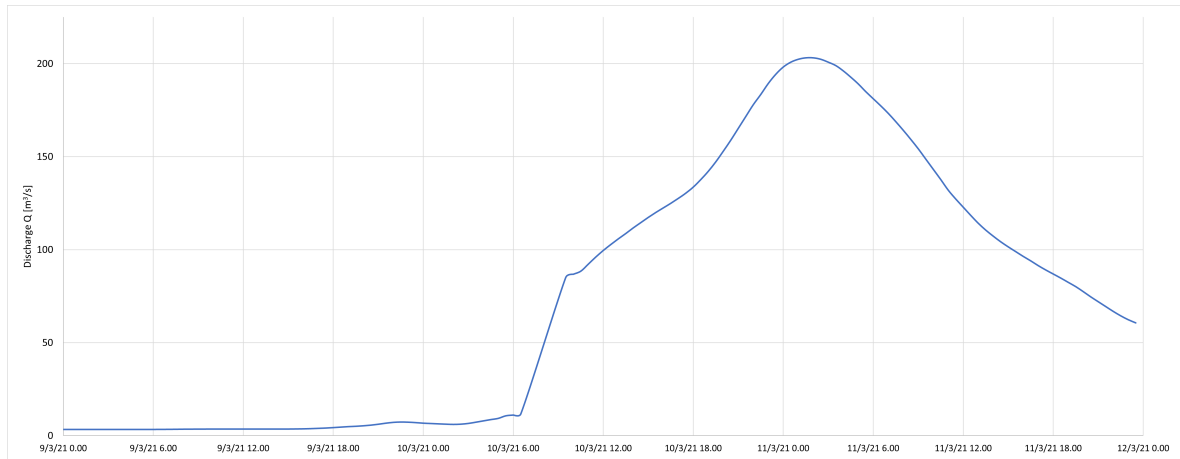
Flow, tide, wind direction and mean wave direction data are shown in the graphs of Figure 2.25. For this event, the anemometric data recorded every 10 minutes by the measurement station located in the coastal town of Bisceglie (28 kilometres south of the Ofanto River mouth) was available. The data are obtained through a request to the Decentralised Functional Center of the Civil Protection of the Puglia Region.

The rainfall event that caused the increase in discharges occurred between 9 and 10 March 2021, while the satellite image was taken on March 11 at 09:50. At that time, the flood wave started to decline after reaching a peak of 203.2 cubic meters per second, recorded on March 11, 2021, at 02:00 at the San Samuele di Cafiero's stream gauging station.

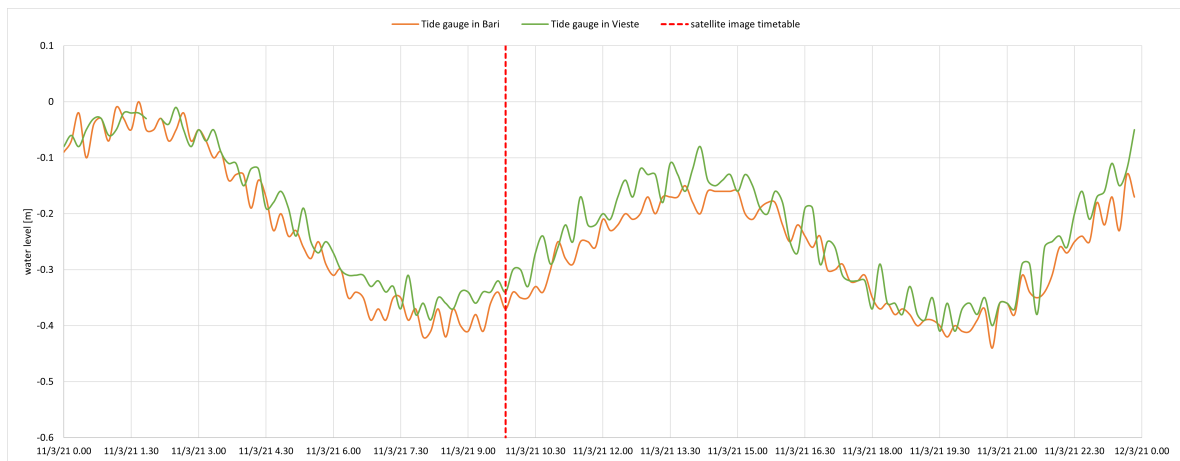
From the satellite image of this day, it can be seen how the plume can be identified as a prototypical plume: the tidal plume front (ebb tide at the time of the satellite shot), the mid-field area and the far-field area in which the inner front and the outer front are well identifiable. The plume extends up to 5 kilometres offshore and the far-field extends in



Figure 2.24: Plume of March 11, 2021.



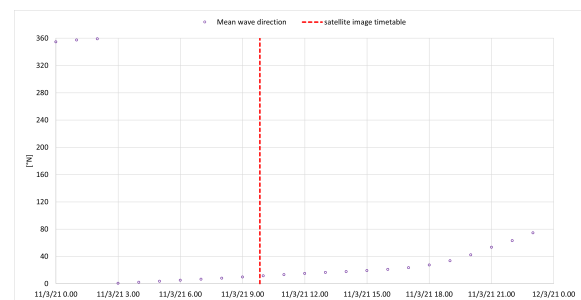
(a) Discharge at San Samuele di Cafiero from March 9, 2021 to March 11, 2021.



(b) Tides recorded in Bari and Vieste.



(c) Wind direction in Bisceglie.



(d) Mean wave direction near the river mouth (data from ERA5).

Figure 2.25: Discharge, tides, wind direction and mean wave direction referring to the river plume event of March 9, 2021.

a south-easterly direction well beyond the port of Barletta. The extent of the far-field is more than ten kilometres but cannot be fully measured due to the lack of satellite images southeast of Barletta. The wind greatly influences the direction; in fact, that morning, it

was blowing in a south-easterly direction (about 110° N).

On the other hand, the direction of the waves does not seem to play a key role in this event either.

3 | Part II - The hydraulic model for coastal river interaction

This chapter has the ultimate goal of simulating through finite element computational models the coastal flow field and, consequently, the direction and mixing of the river plume. Firstly, the TELEMAC-2D software is introduced, after which two-dimensional river and coastal models are developed. Failing to obtain satisfactory replicas of the coastal river plume in 2D, the TELEMAC-3D software is subsequently introduced and a three-dimensional coastal model is developed that can better simulate the flow field, direction and mixing of the river plume over long distances. Figure 3.1 shows the workflow chart which represents the methodology of the simulations performed; starting from the flood events with the related satellite images available representing the fluvial plumes, the process to obtain the simulation of the plume through the computational models is shown with the different 2D and 3D models and with the corresponding inputs.

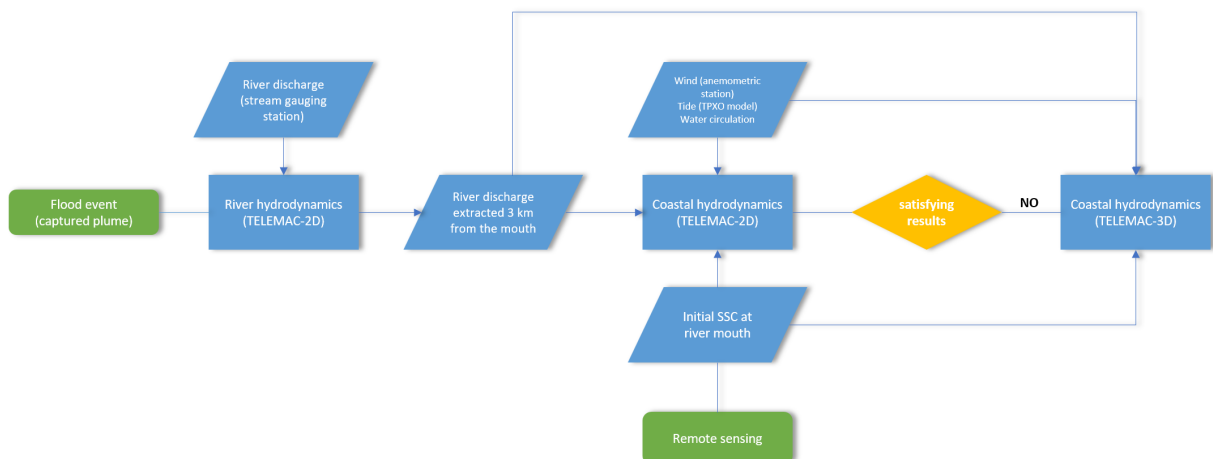


Figure 3.1: Methodology workflow chart.

3.1. 2D hydraulic model

3.1.1. TELEMAC-2D

The open TELEMAC-MASCARET system is a suite of finite element computer program owned by the Laboratoire National d'Hydraulique et Environnement (LNHE), part of the R&D group of Électricité de France. Now managed by a consortium of other consultants and research institutes, more information can be found on their website (www.opentelemac.org). All the simulation modules are written in FORTRAN 90. Its 2D hydrodynamics module, TELEMAC-2D, solves depth-averaged free surface flow equations, known as Shallow Water Equations, first derived by Barré de Saint-Venant in 1871 (also known, therefore, as Saint-Venant equations).

The main application of TELEMAC-2D is in free surface marine or river hydraulics. In the maritime field, it can be used for sizing structures ports, studying the effects of building submersible dykes or dredging, studying the impact of waste discharged from a coastal outfall or simulating thermal plumes. In the river environment, it can be used for studies relating to the impact of construction works (bridges, weirs, tubes), dam breaks, flooding or the transport of decaying or non-decaying tracers.

The program can be used in these areas because it can take into account the following phenomena: propagation of long waves (including nonlinear effects), bed friction, the effect of the Coriolis force, the effects of meteorological phenomena (atmospheric pressure, rain or evaporation and wind), turbulence, supercritical and subcritical flows, the influence of horizontal temperature and salinity gradients on density, transport and diffusion of a tracer by currents, treatment of singularities (weirs, dykes, culverts), dyke breaching, drag forces created by vertical structures, and several other phenomena.

Theoretical aspects

The TELEMAC-2D code solves the following four hydrodynamic equations simultaneously (continuity, momentum along x, momentum along y and tracer conservation):

$$\left\{ \begin{array}{l} \frac{\partial h}{\partial t} + \mathbf{u} \cdot \nabla(h) + h \operatorname{div}(\mathbf{u}) = S_h, \\ \frac{\partial u}{\partial t} + \mathbf{u} \cdot \nabla(u) = -g \frac{\partial Z}{\partial x} + S_x + \frac{1}{h} \operatorname{div}(h \nu_t \nabla u), \\ \frac{\partial v}{\partial t} + \mathbf{u} \cdot \nabla(v) = -g \frac{\partial Z}{\partial y} + S_y + \frac{1}{h} \operatorname{div}(h \nu_t \nabla v), \\ \frac{\partial T}{\partial t} + \mathbf{u} \cdot \nabla(T) = S_T + \frac{1}{h} \operatorname{div}(h \nu_T \nabla T), \end{array} \right. \quad \begin{array}{l} (3.1a) \\ (3.1b) \\ (3.1c) \\ (3.1d) \end{array}$$

where Equation 3.1a is the continuity equation, Equation 3.1b is the equation of the momentum along x , Equation 3.1c is the equation of the momentum along y and Equation 3.1d is the tracer conservation equation, in which:

- h (m) is the water depth;
- u, v (m/s) are the velocity components;
- T (e.g.: g/l, °C or no unit) is the passive (non-buoyant) tracer;
- g (m²/s) is the gravity acceleration;
- ν_t, ν_T (m²/s) are the momentum and tracer diffusion coefficients;
- Z (m) is the free surface elevation;
- t (s) is the time;
- x, y (m) are the horizontal space coordinates;
- S_h (m/s) is the source or sink of fluid;
- S_T (g/l/s) is the source or sink of tracer;
- h, u, v and T are the unknowns.

Inputs and outputs

TELEMAC-2D uses a set of files as input or output. Some files are mandatory, while others are optional and depend on the type of model to implement.

The main input files are the following (many input files are not reported because they are very specific, for further information, see the TELEMAC-2D manual):

- The steering file (mandatory) contains the configuration of the computation and represents the control panel: all keywords are defined in a "dictionary" file which is specific to each simulation module and if a keyword is not contained in this file, TELEMAC-2D will assign it the default value defined in the dictionary file of in the appropriate FORTRAN subroutine.
- The geometry file (mandatory) is a binary file containing all the information concerning the mesh, i.e. the number of mesh points, the number of elements, the number of nodes per element, two arrays containing the coordinates of all the nodes and an array containing the connectivity table. This file may also contain information on the bottom topography, water depth, free surface, friction coefficient, and

initial conditions of tracers. TELEMAC-2D stores geometry information at the beginning of the result file. For this reason, the results file can be used as a geometry file if a new simulation has to be performed on the same mesh, which resumes the previous results.

- The boundary conditions file (mandatory) contains the description of the type of each boundary; that is, for each point, it is indicated whether it represents a Closed boundary (wall), an Open boundary with prescribed depth, an open boundary with free depth, an open boundary with prescribed flowrate, an Open boundary with prescribed velocity or an Open boundary with free velocity. Even for tracers, it is indicated whether it represents a Closed boundary (wall), an Open boundary with prescribed tracer, or an open boundary with free tracer. Each row of the file is dedicated to a point on the mesh boundary, numbered from the bottom left corner of the mesh.
- The previous computation file (optional) gives the initial state of the computation (case of a restart computation).
- The liquid boundaries file (optional) enables the user to specify values for time-dependent boundary conditions (flow rate, depth, velocity, and tracers' concentration).
- The FORTRAN file (optional) contains some specific programming the user performs.
- The tidal model file (optional) contains data used for tidal simulation to prescribe the boundary conditions of a coastal boundary subject to tidal evolution.
- The ASCII database (optional) for tide (databases of harmonic constants are interfaced with TELEMAC-2D: JMJ, TPXO-type from OSU, LEGOS-NEA, FES, PREVIMER).

The output files are as follows:

- The results file, containing the graphical results: the information on the mesh geometry, the names of the stored variables, the time for each time step and the values of the different variables for all mesh points.
- The listing printout, which is the "log file" of the computation, is a formatted file created by TELEMAC-2D during the computation containing the report of a TELEMAC-2D running.

Physical parameter definition – Modelling of turbulence

The modelling of turbulence is a delicate problem. TELEMAC-2D offers the user six options of different complexity: a constant viscosity coefficient model, an Elder model, a $k - \epsilon$ model, a Smagorinski model, a mixing length model and a Spalart-Allmaras model. The default model is the constant viscosity coefficient model, while the model which is generally more accurate, but with more significant computational burdens, is the $k - \epsilon$ model.

Using the constant viscosity coefficient model the turbulent viscosity is constant throughout the domain. The overall viscosity coefficient (molecular and turbulent viscosity) has a default value of 10^{-6} meters squares per second (corresponding to the molecular viscosity of water).

The $k - \epsilon$ model is used if constant viscosity is not sufficient. The overall viscosity coefficient has its real physical value (10^{-6} meters squares per second for molecular diffusion of water), as this is used as such by the turbulence model. Turbulent viscosity may be given by the user or determined by a model simulating the transport of turbulent quantities k (turbulent kinetic energy) and ϵ (turbulent dissipation), for which the equations are the following:

$$\left\{ \begin{array}{l} \frac{\partial k}{\partial t} + \mathbf{u} \cdot \nabla(k) = \frac{1}{h} \text{div} \left(h \frac{\nu_t}{\sigma_k} \nabla k \right) + P - \epsilon + P_{k\nu}, \\ \frac{\partial \epsilon}{\partial t} + \mathbf{u} \cdot \nabla(\epsilon) = \frac{1}{h} \text{div} \left(h \frac{\nu_t}{\sigma_\epsilon} \nabla \epsilon \right) + \frac{\epsilon}{k} (c_{1\epsilon} P - c_{2\epsilon} \epsilon) + P_{\epsilon\nu}. \end{array} \right. \quad (3.2a)$$

$$\left\{ \begin{array}{l} \frac{\partial k}{\partial t} + \mathbf{u} \cdot \nabla(k) = \frac{1}{h} \text{div} \left(h \frac{\nu_t}{\sigma_k} \nabla k \right) + P - \epsilon + P_{k\nu}, \\ \frac{\partial \epsilon}{\partial t} + \mathbf{u} \cdot \nabla(\epsilon) = \frac{1}{h} \text{div} \left(h \frac{\nu_t}{\sigma_\epsilon} \nabla \epsilon \right) + \frac{\epsilon}{k} (c_{1\epsilon} P - c_{2\epsilon} \epsilon) + P_{\epsilon\nu}. \end{array} \right. \quad (3.2b)$$

The right-hand side terms of these equations represent the production and destruction of turbulent quantities (energy and dissipation).

Physical parameter definition – Wind influence

In TELEMAC-2D, the wind is an optional parameter and can be used to simulate flow taking into account the influence of a wind blowing on the water surface. In TELEMAC-2D, the force induced by wind is considered in the same way as the friction effect on the bottom. The following force is consequently added to the right-hand side term of the momentum equation:

$$\left\{ \begin{array}{l} F_x = \frac{1}{h} \frac{\rho_{air}}{\rho_{water}} a_{wind} U_{wind} \sqrt{U_{wind}^2 + V_{wind}^2}, \\ F_y = \frac{1}{h} \frac{\rho_{air}}{\rho_{water}} a_{wind} V_{wind} \sqrt{U_{wind}^2 + V_{wind}^2}. \end{array} \right. \quad (3.3a)$$

$$\left\{ \begin{array}{l} F_x = \frac{1}{h} \frac{\rho_{air}}{\rho_{water}} a_{wind} U_{wind} \sqrt{U_{wind}^2 + V_{wind}^2}, \\ F_y = \frac{1}{h} \frac{\rho_{air}}{\rho_{water}} a_{wind} V_{wind} \sqrt{U_{wind}^2 + V_{wind}^2}. \end{array} \right. \quad (3.3b)$$

The wind can be introduced in input as: constant in time and space, variable in time and constant in space or variable in time and space (suitable for large domains).

The influence of the wind depends on the smoothness (or lack of it) of the free surface and the distance over which it acts (called the "fetch"). The coefficient value can be obtained from many different formulas. Recommended the manual is the formula used by the Institute of Oceanographic Sciences (United Kingdom):

$$\begin{cases} \textit{if} & \|U_{wind}\| < 5 \text{ m/s} & a_{wind} = 0.565 \times 10^{-3} \\ \textit{if} & 5 < \|U_{wind}\| < 19.22 \text{ m/s} & a_{wind} = (-0.12 + 0.137 \|U_{wind}\|) \times 10^{-3} \\ \textit{if} & \|U_{wind}\| > 19.22 \text{ m/s} & a_{wind} = 2.513 \times 10^{-3} \end{cases}$$

Coefficient of wind influence asked for by TELEMAC-2D is: a_{wind} times the ratio between air density ρ_{air} (1.2 kg/m³) and water density ρ_{water} (1000 kg/m³). Thus it is necessary to divide the value of a_{wind} by 1000 to obtain the value of the TELEMAC-2D keyword.

3.1.2. Ofanto River flood modeling

Since the stream gauging station closest to the Ofanto River mouth is located near San Samuele di Cafiero (about 18 kilometres inland), a fluvial model of this final stretch of the river has been developed in order to have flow rate data at the mouth in the right time and to consider possible flooding downstream of the stream gauging station. The study area of the entire project is shown in Figure 3.2, where there are: the river model (yellow outline) for the simulation of downstream flows, the coastal model (white outline) for the simulation of the plume and the area of extraction of the river model discharges (used as input in the coastal model).

The roughness coefficients were calibrated by analyzing the satellite image of March 11 2021 (09:50), which reported an extensive river overflow. To carry out the calibration, the flooded areas of the satellite image taken at 09:50 were compared with the flooded areas (again at 09:50 of that day) of the models with different roughness coefficients.

In order to have precise data on the terrain and the river bed, a request was made to the Ministry of Ecological Transition - National Geoportal for DTM LiDAR data with 1-meter ground resolution of the area of interest. This is a Digital Terrain Model (DTM) with 1-meter ground resolution deriving from LiDAR scanning on an aerial platform, acquired by the Ministry of the Environment and the Protection of the Territory and the Sea under the Extraordinary Plan for Environmental Remote Sensing and the Project PON-MIADRA. It is dated July 4, 2013, and refers to the geodetic system WGS84 (World Geodetic

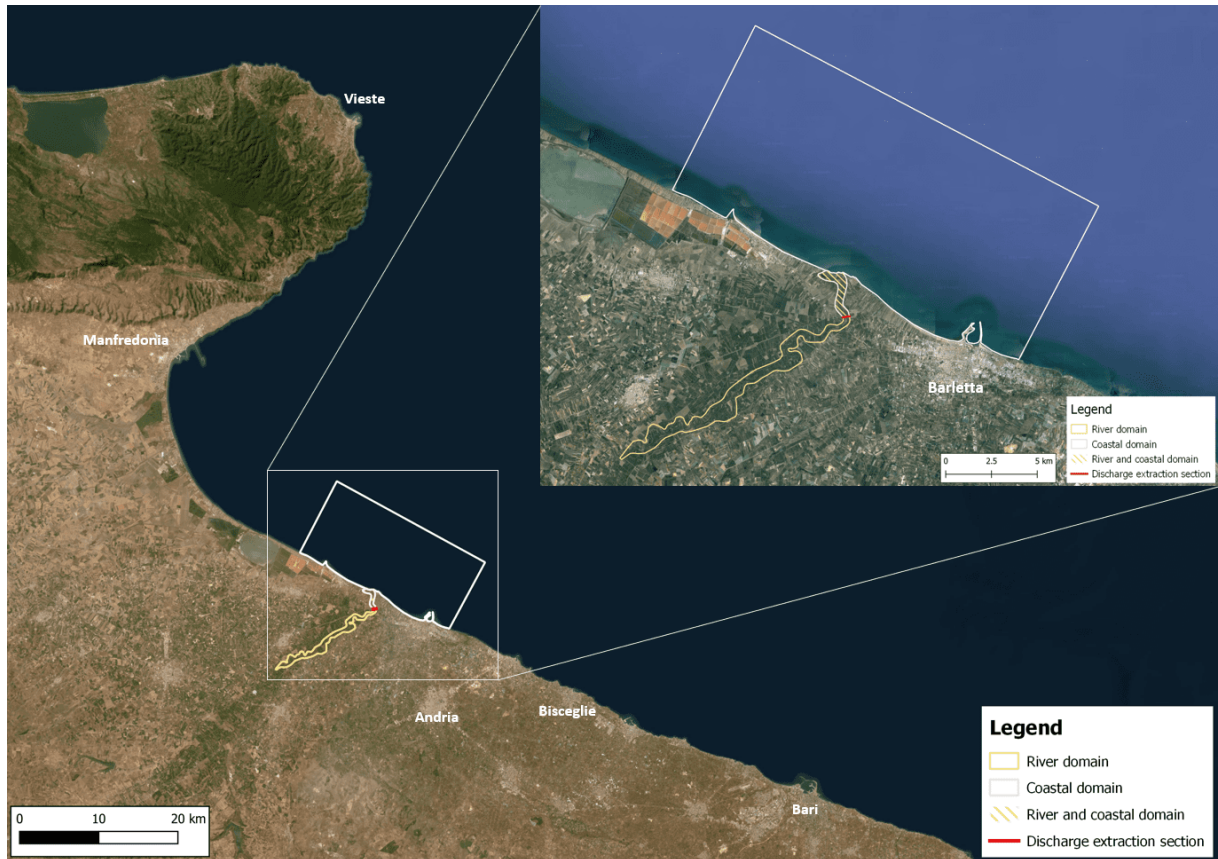


Figure 3.2: River and coastal domains.

System 1984). All data are projected in UTM zone 33N (Universal Transverse Mercator) and cartographically represented in WGS84–UTM zone 33N.

Mesh and boundary conditions

The Bluekenue software, developed by the Canadian Hydraulics Center of the National Research Council, was used to carry out the pre-processing: to make the mesh, to impose the boundary conditions, to assign the bottom and roughness coefficients.

The fluvial model domain is built upstream from the stream gauging station of San Samuele di Cafiero, following the right and left banks of the river up to the sea (downstream edge). Its area is equal to 11.4 square kilometres, while the length of the river branch is approximately 25 kilometres.

In order to better simulate the flow of water inside the riverbed, an exclusive, more specific mesh of the riverbed has been built; it contains 63161 nodes, with along channel nodes spaced 6 meters and with fourteen cross channel nodes between one bank and the other. Then the mesh of the entire domain was created (implementing it also that of the fluvial

branch only), which is very dense; in fact, it has a total of 218576 nodes, of which 215346 are internal nodes and 3230 are external nodes; the latter spaced evenly 15 meters from each other. In Figure 3.3, the mesh of the river domain is shown, in which it is noted that, in the area of the river branch, the mesh is thickened; as an example to show it more defined, the mesh is shown more enlarged in the central area of the domain.

In order to create the geometry file the values (in meters) of the available DTM are assigned to the mesh, while the roughness coefficients, the values are assigned using Manning's coefficient (n). The values of Manning's coefficient (object of model calibration) are assigned by distinguishing the riverbed area from the floodplain area. The illustrative images of the bottom and the values of Manning's coefficient are listed in the Appendix B.1.

The boundary conditions file is set by assigning the following values:

- Closed boundary (wall) on lateral boundaries, i.e. a no-flow boundary condition;
- Open boundary with prescribed flowrate (without tracer) on the upstream boundary;



Figure 3.3: Mesh with illustrative zoom in the central area of the domain.

- Open boundary with prescribed depth on the downstream edge.

These boundary conditions are necessary in order to impose, upstream, the flow rates recorded by the stream gauging station of San Samuele di Cafiero and to obtain, downstream, a water flow that can fall out of the domain.

Flood modelling simulation and calibration

The objective of the simulation is to replicate the river overflow and extract the discharges downstream, about 3 km from the coast. This discharge extraction point (red line in Figure 3.2) is precisely the river section where the upstream river boundary conditions have been imposed for the coastal model developed for the simulation of the river plume.

The simulation begins on March 9, 2021, at 00:00 and ends on March 11, 2021, at 12:00. Since the mesh is very thick, especially in the riverbed area, the time step was set to 0.5 seconds, and the number of time steps was, therefore, 518400 to simulate 60 hours. Such a short time step does not create problems with Courant's number. To make the model reach stability quickly and obtain a discharge extracted downstream with stable and precise values as possible, an initial condition was derived from a simulation carried out on March 8, 2021.

The input flow rates are those already shown in Figure 2.25a, in which a peak of 203 cubic meters per second can be seen on March 11, 2021, at 02:00.

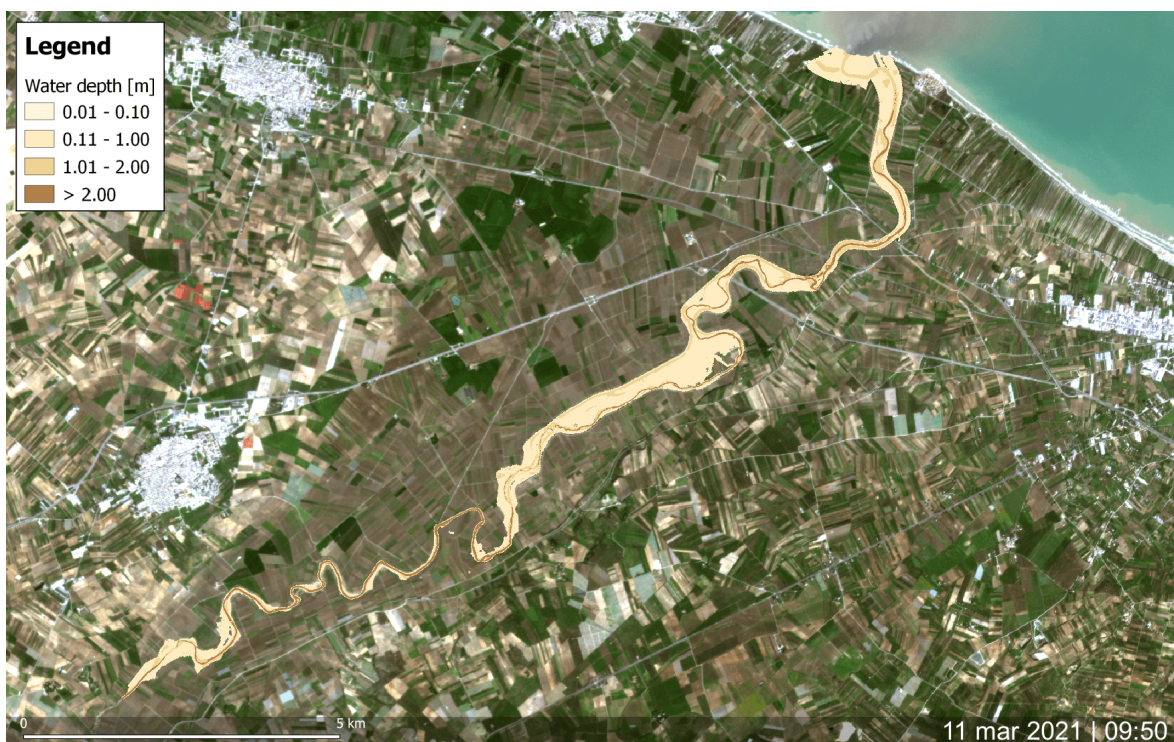
In order to have a very accurate simulation of the event, the $k - \epsilon$ turbulence model was used, even if this required long computational times.

In order to calibrate the model, reference was made to the image taken on March 11, 2021, at 09:50 from a SuperDove satellite, shown in Figure 3.4a, in which the flooded areas of the Ofanto River can be seen. Three runs of the model were performed, assigning different Manning's roughness coefficients. By comparing the flooded areas in the image with those simulated by the model, it was concluded that the best Manning's coefficients (n) are $0.04 \text{ s/m}^{1/3}$ for the riverbed and $0.06 \text{ s/m}^{1/3}$ for the floodplains (Simulation 3). These coefficients were chosen by looking at Planet and Google Earth satellite images, noting a thick expanse of trees near the river banks and cultivated fields and shrubs in the floodplains.

The images in Figure 3.4a and Figure 3.4b show on March 11 2021, at 09:50, in order, the flooded areas snapped by satellite and the flooded areas simulated by the model (Simulation 3). The model simulates flooded areas well, especially in the upstream and central areas, while it simulates the downstream area less well. This last part of the river



(a) Flooded areas taken from satellite.



(b) Flooded areas simulated by the river model (Simulation 3).

Figure 3.4: Comparison between flooded areas taken from satellite and simulated by the river model.

is less critical for calibrating this model because the areas less coherent with the satellite image are located downstream of the discharge extraction section. This inconsistency with the satellite image is because the Manning coefficients are lower in the downstream area of the river; in fact, there are no plants and shrubs, but only fields with short grass and the river banks seem very clean.

Appendix B.1 shows the same images but enlarged in the upstream area, in the central area and in the downstream area.

Figure 3.5 shows the maximum discharges extracted at approximately 3 kilometres from the mouth for each simulation. Table 3.1 summarizes the Manning coefficients used in the simulations, the maximum discharges extracted at about 3 kilometres from the mouth and when they happened. There is a difference of 3158 seconds (about 53 minutes) between the time in which the maximum flow occurs in Simulation 3 and that of Simulation 1, while there is a difference of 1183 seconds (about 20 minutes) between the time in which the maximum discharge occurs in Simulation 3 and that of Simulation 2. This is because the roughness of Simulation 3 is greater than the others. Furthermore, in Simulation 3, the maximum discharge at the section at 3 kilometres from the mouth occurs 197102 seconds after the start of the computation, i.e. on March 11, 2021, at 06:45, while at the stream gauging station of San Samuele di Cafiero, the peak discharge occurred on March 11, 2021, at 02:00.

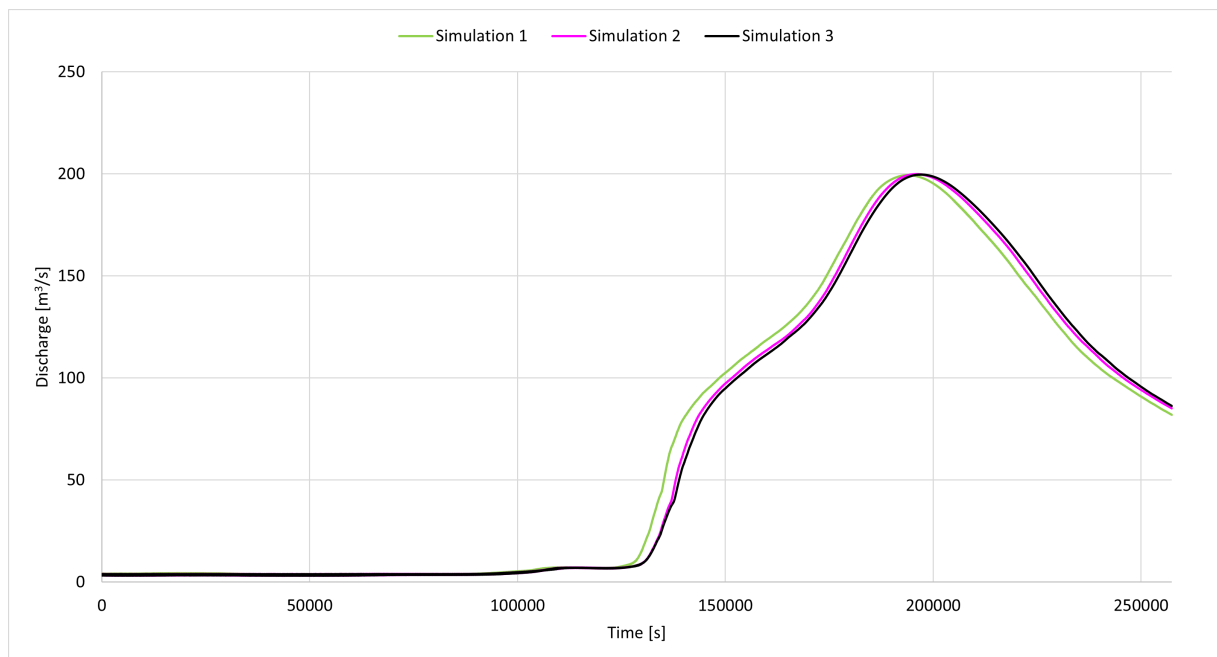


Figure 3.5: Simulated discharges with different Manning's coefficients, extracted at 3 kilometres from the mouth.

Table 3.1: Manning’s coefficients used and simulation results extracted 3 kilometers from the mouth.

	Simulation 1	Simulation 2	Simulation 3
n_{riverbed} [s/m ^{1/3}]	0.3	0.4	0.4
$n_{\text{floodplain}}$ [s/m ^{1/3}]	0.4	0.5	0.6
Q_{MAX} [m ³ /s]	199.38	199.90	199.68
T_{MAX} [YYYY/MM/dd HH : mm]	2021/03/11 05:52	2021/03/11 06:25	2021/03/11 06:45
$T_{3 \text{ MAX}} - T_{1 \text{ MAX}} = 53 \text{ min}$			
$T_{3 \text{ MAX}} - T_{2 \text{ MAX}} = 20 \text{ min}$			

3.1.3. Coastal zone modelling

The coastal model aims to simulate the plume phenomenon caused by the suspended solid transport of the Ofanto River, reproducing a flow field that can emulate what actually happened, verifying it through satellite images. Not having available samplings in situ of the river sediments, it was not possible to implement a hydro-morphodynamic model because the diameter of the sediments at the mouth and their characteristics are not known. Alternatively, the plume is simulated with a dye-like tracer. Similarly, the sea concentrations of suspended solids are not available; therefore, a spectral band-based formula is applied, taken from the literature, which allows to estimate the surface concentrations by analyzing the spectral bands of the image. The formula calibrated and validated by [Zhang et al., 2014] in their study on suspended solid concentrations in Hong Kong bay is based on water reflectance:

$$SSC = 0.0242 \cdot \exp \left[6.3466 \cdot \frac{R_{ss}(645)}{R_{ss}(555)} \right] \quad (3.5)$$

where SSC denotes the suspended sediment concentration (in mg/L) and $R_{ss}(645)$ and $R_{ss}(555)$ denote the water reflectance on bands 645 nanometers and 555 nanometers, respectively. Therefore, having the satellite image available with the corresponding spectral bands (as it is possible to obtain from Planet Lab), it is possible to estimate approximately the concentrations of solid in suspension.

To get a new image of the event, which highlights the solid concentrations in suspension, Sentinel Application Platform (SNAP) software was used, made available free of charge by the European Space Agency (ESA), developed by Brockmann Consult, Skywatch, Sensar and CS, and ideal for Earth observation (EO) processing and analysis. SNAP allows to explore, analyze and process remotely data, facilitating scientific research, education and training activities and the development of a wide range of operational applications.

In SNAP, it is possible to perform mathematical operations using the spectral bands of the images; it is, therefore, possible to obtain a new image with the concentrations by applying the SSC formula from [Zhang et al., 2014]. Figure 3.6 shows the SNAP control panel, in which it is possible to manage the satellite data and perform operations between the spectral bands of the image. Indeed, in the example, it is possible to note the spectral bands of the image produced by Sentinel-2B on April 24, 2020, and the suspended solids by applying the SSC formula.

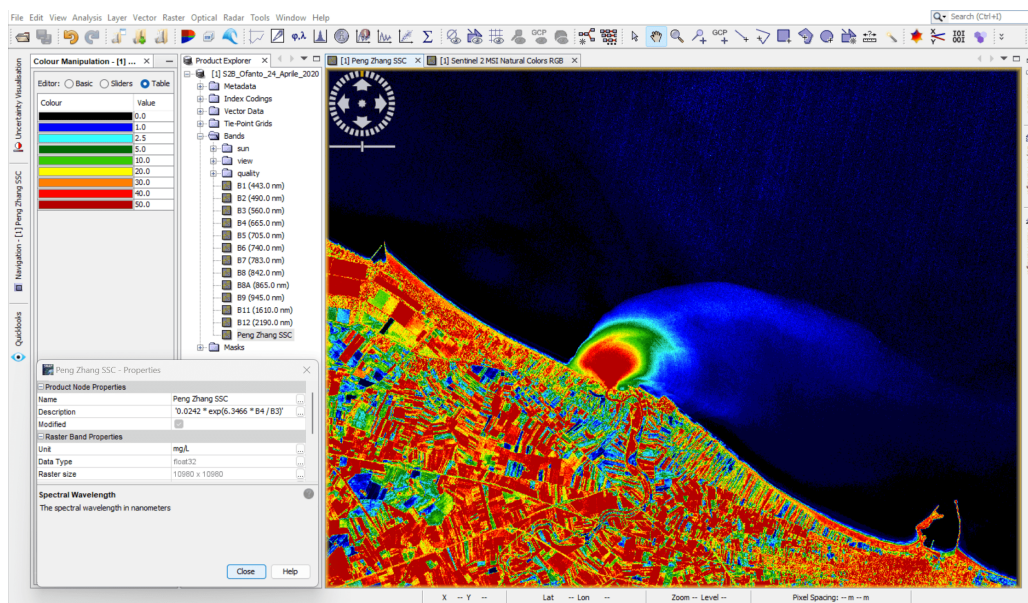


Figure 3.6: SNAP control panel.

Mesh and initial and boundary conditions

Thanks to the Bluekenue software, it is possible to perform the pre-processing: to make the mesh, to impose the boundary conditions, to assign the bottom and roughness coefficients.

The coastal model domain (outline in white), shown in Figure 3.2, is built from the downstream extraction area of the river model indicated in red line, following the right and left banks of the river (about 3 kilometres) up to the sea (river mouth), continuing for 10 kilometres to the South-East up to beyond the port of Barletta and 10 kilometres to the North-West up to beyond Margherita di Savoia; meanwhile, the marine area extends offshore for 10 kilometres and reaches a maximum depth of about 30 meters. The coastal domain area is equal to 212 square kilometres.

In order to better simulate the flow of water inside the riverbed, an exclusive, more specific mesh of the riverbed has been built; it contains 4380 nodes, with along channel nodes spaced 8 meters and with ten cross channel nodes between one bank and the other. Then

the mesh of the entire domain was created (implementing it also that of the fluvial branch only), which is dense, especially in the river area and around the mouth, while it reaches lower densities on the marine border of the domain. The finite element numerical grid has a total of 43384 nodes, of which 42309 are internal and 1075 are external. In Figure 3.7, the mesh of the coastal domain is shown, in which it is noted that, in the area of the river branch, the mesh is thickened; as an example, the mesh is shown more enlarged in the river mouth area.

In order to create the geometry file, as regards the bottom, the values (in meters) of the available DTM are assigned to the mesh in the fluvial area; while in the marine area the bottom is based on bathymetric data digitized from NAVIONICS nautical charts. As regards the roughness coefficients, the values are assigned using Manning's coefficient (n). The values of Manning's coefficient are assigned by distinguishing the riverbed area ($0.028 \text{ s/m}^{1/3}$) from the floodplain area ($0.04 \text{ s/m}^{1/3}$) and the seabed ($0.025 \text{ s/m}^{1/3}$); these values are similar to those used in a previous study for the Puglia Region, carried out at the Ofanto River mouth. The illustrative images of the bottom and the values of Manning's coefficient are listed in the Appendix B.2.

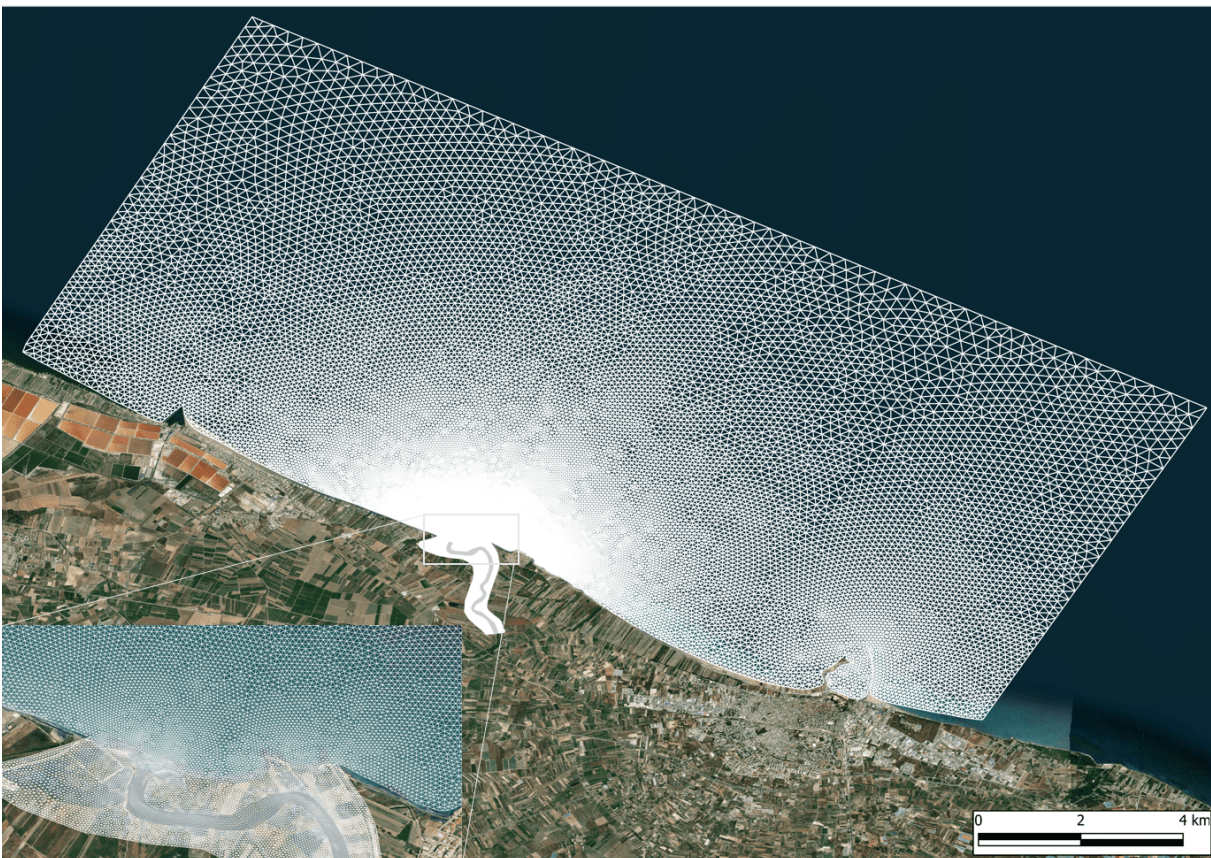


Figure 3.7: Mesh with illustrative zoom in the river mouth area of the domain.

In the river area, the initial conditions in the model are the initial flow rate obtained from the river model at 3 kilometres from the coast, a river water level equal to 0.5 metres. At the sea boundary, the initial conditions are the elevations and regional tide velocity fields obtained by the Oregon State University (OSU) Tidal Inversion System (OTIS [Egbert and Erofeeva, 2002]), internally coupled to TELEMAC (Topex Poseidon —TPXO). At the surface boundary, ERA5 wind data with 1-hour temporal resolution are used, or, if available, the wind data from the nearest anemometric stations are used (10 minutes temporal resolution in Bisceglie, Andria or Manfredonia). These data are interpolated in time and space for every point of the numerical mesh. The initial tracer concentration is zero mg/L throughout the domain, with a constant enforced concentration at the river boundary.

The boundary conditions file is set by assigning the following values:

- Closed boundary (wall) on lateral boundaries, ie a no-flow boundary condition;
- Open boundary with prescribed flow rate (with tracer) on the river boundary;
- Open boundary with prescribed velocities and depth on the marine edges.

These boundary conditions are necessary in order to impose upstream the flow rates extracted by the fluvial model and a constant injection of tracer concentration and reproduce the flow field in the maritime domain where the fluvial plume will extend.

Appendix B.2 shows the imposed boundary conditions, where Closed boundary (wall) nodes are brown, Open boundary with prescribed Q nodes are blue, and Open boundary with prescribed UV and H nodes are orange (Q is volumetric flow rate, U and V are the velocities and H is water depth).

3.1.4. Coastal modelling simulations and calibrations

March 11, 2021, event

The goal of coastal modelling is to replicate the coastal flow field in order to obtain a river plume as similar as possible to those captured by satellites. The plume event of March 11, 2021 (Figure 3.8a) is simulated, which results as the most extensive in the researched period. By applying the SSC formula [Zhang et al., 2014] using SNAP, the suspended solid concentrations are found in order to be able to calibrate the model (Figure 3.8b). This image also shows the offshore distance reached by the tidal plume front and its area, the distance of the mid-field area and the far-field outer front near the port of Barletta.

The simulation begins on March 9, 2021, at 00:00 and ends on March 11, 2021, at 12:00.

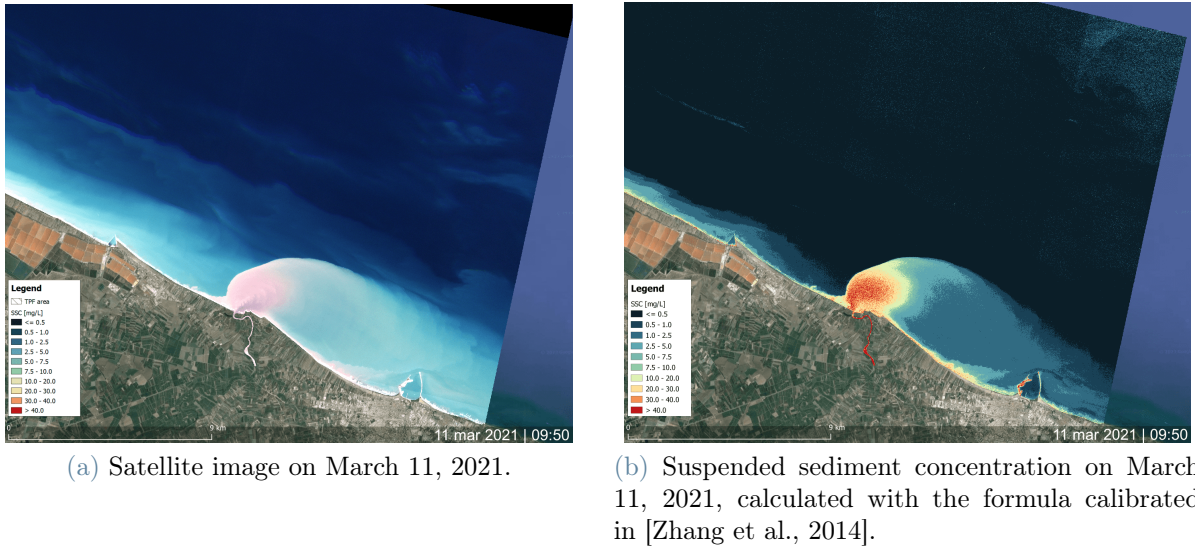


Figure 3.8: Satellite image on March 11, 2021, and the same with suspended sediment concentration (SSC).

Since the mesh is very dense, especially in the riverbed area, the time step is set to 1 second, and the number of time steps is, therefore, 259200 to simulate 60 hours. Such a short time step does not create problems with Courant's number.

The input flow rates are those already shown in Figure 3.5, in particular, that corresponding to the model river calibrated (Simulation 3) with a peak of 199 cubic meters per second. The tracer is also inserted in the river upstream border, with a concentration of 55 mg/L (value taken from the image of Figure 3.8b in the upstream area. The wind that reproduces the best result is that recorded by the anemometric station of Bisceglie, while the tide is reproduced from the TPXO data and compared with that of Vieste and Bari (Figure 3.9).

Since all river plumes are greatly influenced by the mixture of freshwater and sea salt water, simulations are done both considering sea salt water with an average water temperature of 12 degrees (data taken from ERA5), and considering the entire domain without salinity and water temperature (the latter, in TELEMAC-2D, can only be implemented simultaneously with salinity). In the 2D model, the best results are obtained by omitting the salinity; this omission is due to the fact that the 2D model fails to effectively simulate the mix of fresh and saltwater at the river mouth. Salinity becomes fundamental, however, in the 3D model, which is able to simulate the mixture between freshwater and saltwater better.

The turbulence model used is the constant viscosity turbulence model, which is a method

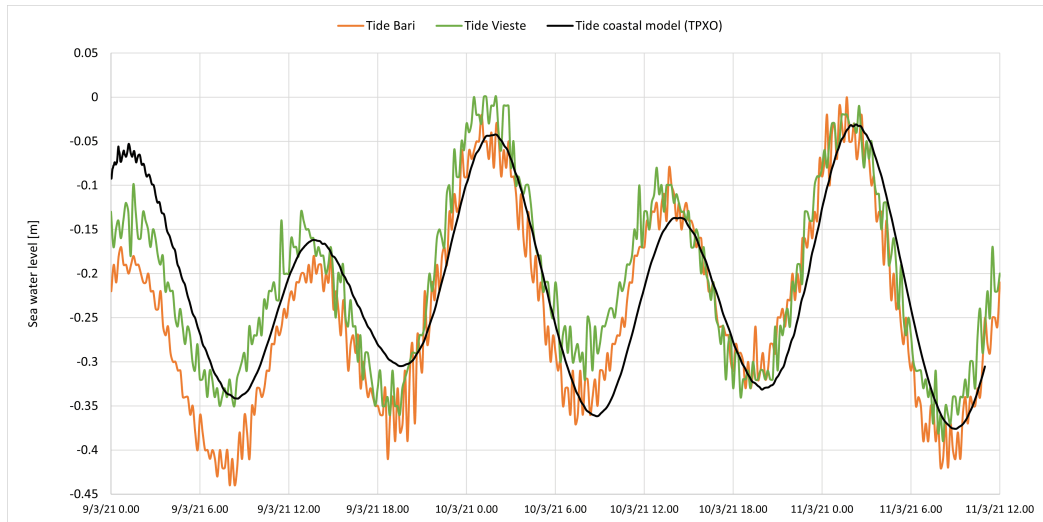


Figure 3.9: Comparison of the tides recorded in Bari and Vieste with the one simulated in the coastal model with the TPXO database.

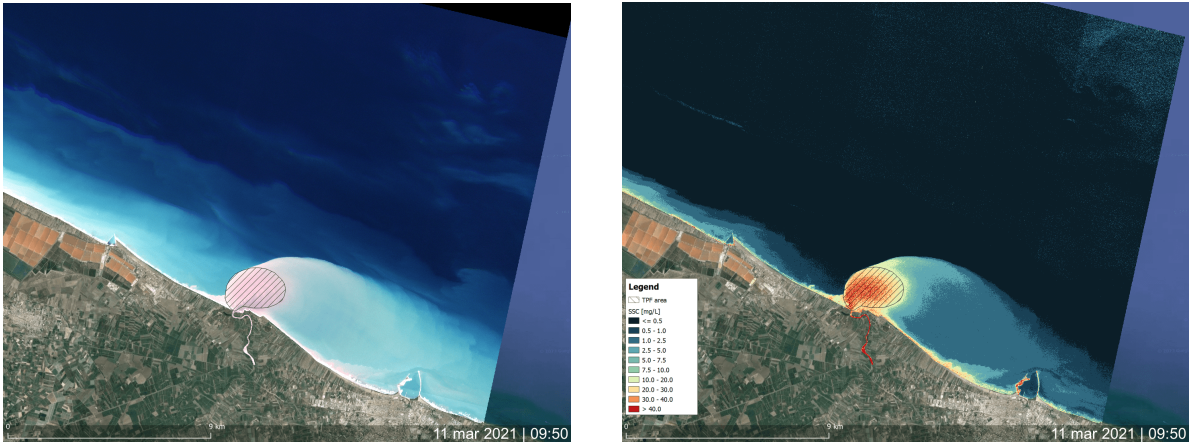
that requires less computational effort and, therefore, shorter computation times than the $k - \epsilon$ model.

The best set of physical parameters resulting from the calibration exercise of the TELEMAC-2D model (comparing the satellite image processed with SNAP with the product of the simulations) are shown in Table 3.2.

The main results computed at each node of the computational mesh are the depth-averaged velocity components, the water depth, the free surface and the tracer concentrations.

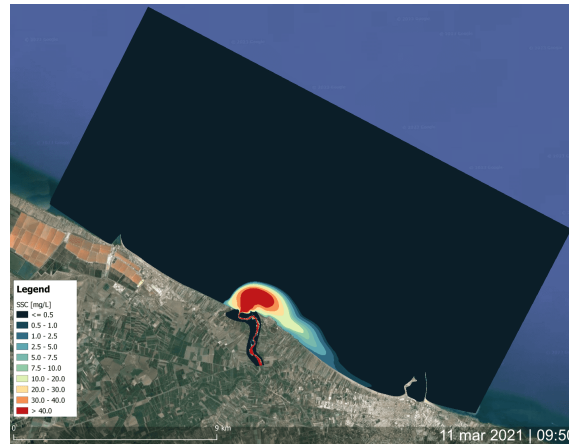
Table 3.2: The best set of physical parameters resulting from the calibration exercise of the TELEMAC-2D model.

Coriolis coefficient	9.5×10^{-5}
Turbulence model	Constant viscosity
Tidal flats	Yes
Time step	1 s
Seabed Manning's coefficient	0.025
River Manning's coefficient	0.028; 0.04
Tide (TPXO) at the shooting time	ebb
Coefficient of wind influence	variable with wind speed
Constant inflow tracer concentration	55 mg/L
Salinity	No



(a) Satellite image on March 11, 2021, with the tidal plume front (TPF) outlined.

(b) Suspended sediment concentration on March 11, 2021, calculated with the formula calibrated in [Zhang et al., 2014].



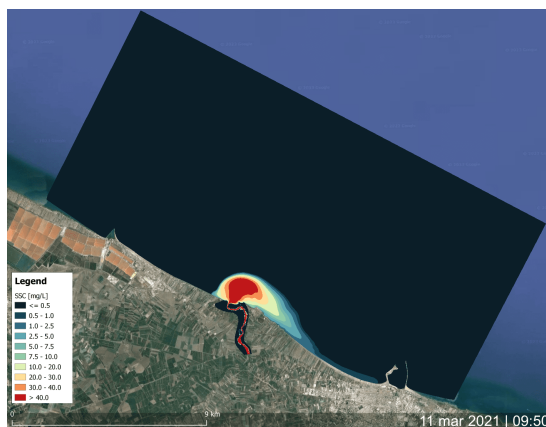
(c) 2D simulation of the March 11, 2021, plume (reproduction using a tracer as dye and wind recorded in Bisceglie).

Figure 3.10: Satellite image of March 11, 2021, the same with suspended sediment concentration (SSC formula) compared with the simulated 2D model, using the wind recorded by the Bisceglie anemometric station.

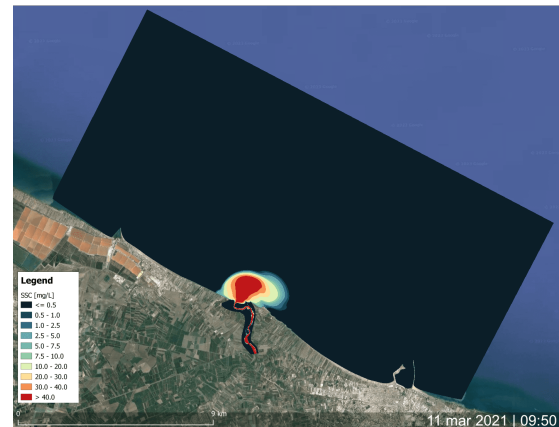
The satellite image of March 11 2021, at 09:50 (Figure 3.10a) and the relative image of the solid concentrations in suspension (Figure 3.10b) can be compared with the best result obtained with TELEMAC-2D by calibrating the parameters according to the satellite image (Figure 3.10c). The numerical result simulates the near-field area well: it extends for about 2300 meters offshore with an area of about 4 square kilometres in the satellite image and about 2000 meters offshore with an area of about 3 square kilometres in the simulated model. However, the model fails to simulate the mid-field and far-field plume areas. It is mainly due to the exclusion of salinity from the simulations, which, in the

literature, is always indicated as a decisive factor for the surface buoyancy of suspended solids.

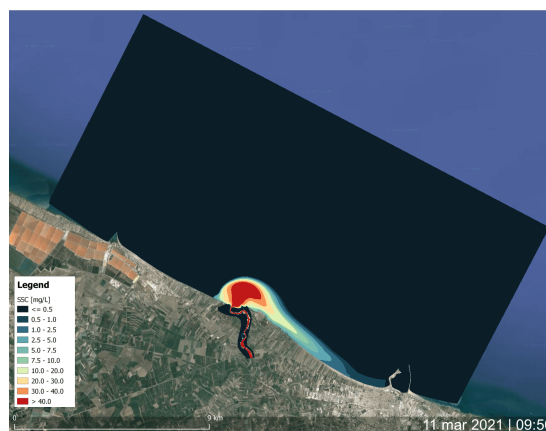
Knowing that the mid-field and the far-field are mainly conditioned by wind forcing, tests are carried out with anemometric data from measuring stations further inland or further away from the study area, such as Andria and Manfredonia; moreover, a simulation is also carried out with the ERA5 wind data. The results are shown in Figure 3.11: the simulation applying the wind recorded in Andria does not satisfactorily replicate the event; probably, this is because this station is located 20 kilometres inland and the winds are different from those on the coast. The simulations using the wind recorded in Manfredonia (city on the coast) and the wind obtained from the ERA5 data simulate the result in an almost analogous way. Therefore, the plume replica is influenced by the effect of the wind, particularly if the wind is not recorded near the coast.



(a) Simulation of tracer dispersion with Manfredonia wind.



(b) Simulation of tracer dispersion with Andria wind.



(c) Simulation of tracer dispersion with ERA5 wind.

Figure 3.11: 2D simulations of the same event, applying different wind recordings.

The anemometric station located in Barletta has been active since May 2022, which is positioned near the south-eastern border of the domain. This new wind data, considering events after May 2022, should improve plume simulation in the mid-field and far-field area.

April 24, 2020, event

Validation of the 2D model, at least as regards the identification of the near-field of the plume, is carried out by reproducing the plume event captured by the Sentinel-2B satellite on April 24, 2020, at 09:40. The parameters of the model used are the same as reported in Table 3.2. The discharge entering the model is calculated using the river model, simulating the flow from 00:00 on April 22 2020, until 12:00 on April 24 2020; the graph of Figure 3.12 shows the discharge extracted at 3 kilometres from the river mouth and used as input in the coastal model.

The wind that reproduces the best result is the one recorded by the anemometric station of Manfredonia, since the stations of Barletta and Bisceglie (both on the coast and much closer) were not in operation in these dates. The tide is simulated using TPXO data and compared with Vieste and Bari's (Figure 3.13).

The satellite image of April 24 2020, at 09:40 (Figure 3.14a) and the relative image of the solid concentrations in suspension (Figure 3.14b) can be compared with the best result obtained with TELEMAC-2D (Figure 3.14c). Also in this case, the mid-field and far-field zones are not reproduced by the model; instead, once again, the tidal plume front is well

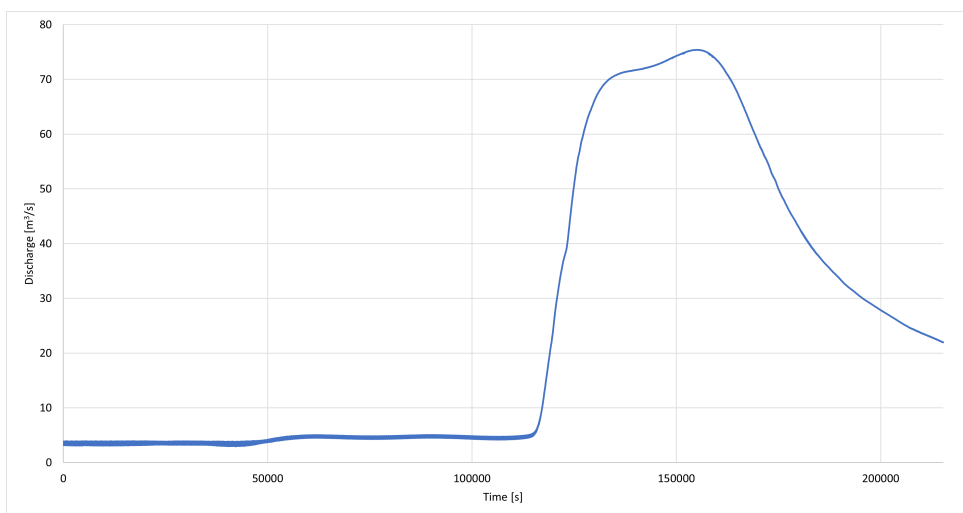


Figure 3.12: Discharge extracted 3 kilometers from the river mouth, simulated with the river model.

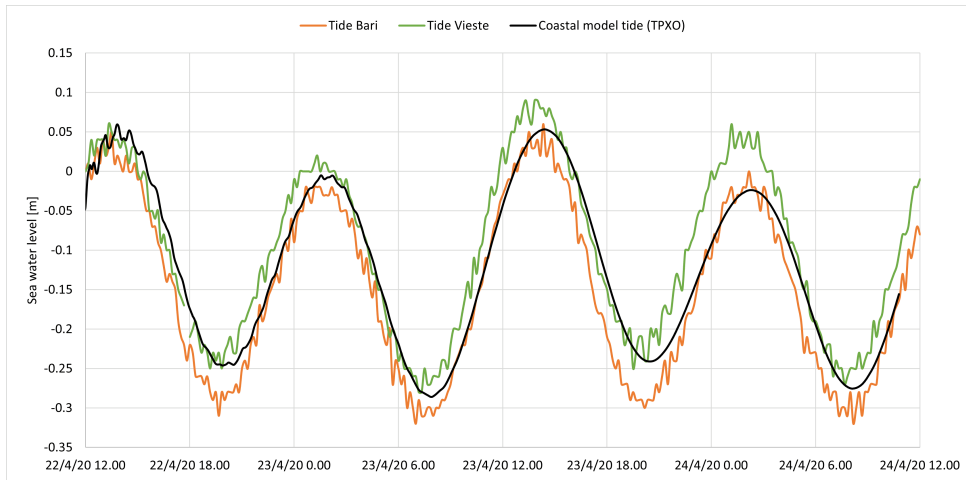
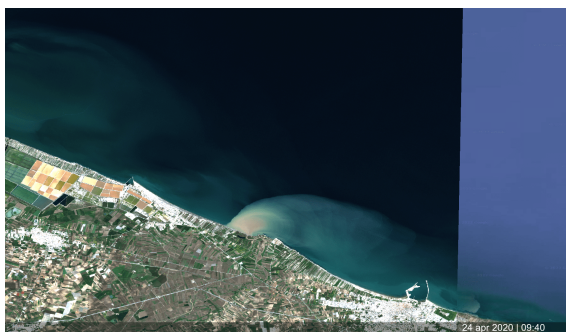
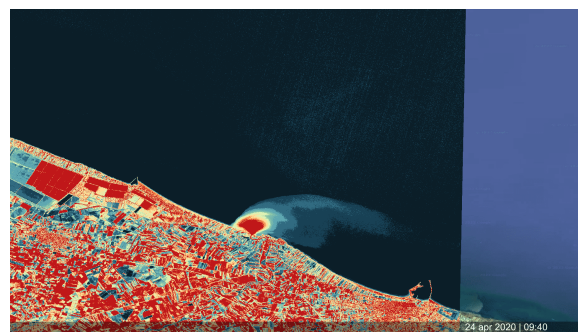


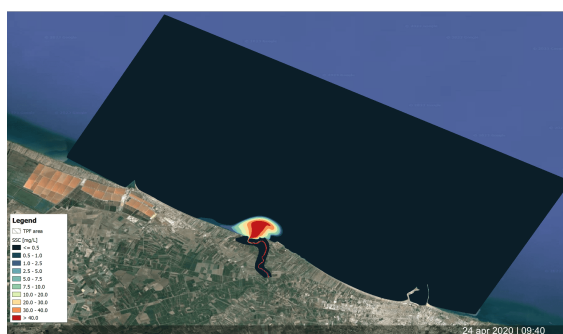
Figure 3.13: Comparison of the tides recorded in Bari and Vieste with the one simulated in the coastal model with the TPXO database.



(a) Satellite image on April 24, 2020.



(b) Suspended sediment concentration on April 24, 2020, calculated with the formula calibrated in [Zhang et al., 2014].



(c) 2D simulation of the April 24, 2020, plume (reproduction using a tracer as dye and wind recorded in Manfredonia).

Figure 3.14: Satellite image of April 24, 2020, the same with suspended sediment concentration (SSC formula) compared with the simulated 2D model, using the wind recorded by the Manfredonia anemometric station.

simulated, being about 1500 meters offshore with an area of 1.7 square kilometres for the satellite image and 1500 meters offshore with an area of 1.8 square kilometres for the 2D model.

The results obtained by calibrating the two-dimensional model reproduce well the tidal plume front, but not the mid-field and far-field; this can be due to many factors, such as:

- The lack of wind data from the Barletta anemometric station, which is located on the South-East border of the model and, therefore, it is the station that can record the wind values closest to the area of interest, considering that the wind plays the main role in the plume areas that are not simulated well by the model.
- The omission of the salinity because the mixture of freshwater and saltwater in the river mouth area is poorly reproduced in 2D.
- The lack of data on the sediments transported by the river, which have their own density and their own buoyancy, unlike the tracer used, which behaves like a dye.
- The lack of a model that simulates wind-generated water wave and their breaking ashore, even if from the correlation analysis of the direction of the plume with the mean wave direction, carried out in Section 2.4.3, no particular connections are found.

3.2. 3D hydraulic model

3.2.1. TELEMAC-3D

The open TELEMAC-MASCARET system, in its 3D hydrodynamics module (TELEMAC-3D code), solves such three-dimensional equations as the free surface flow equations (Navier-Stokes equations) and the transport-diffusion equations of intrinsic quantities (temperature, salinity concentration). At each point in the resolution mesh in 3D, its main results are the 3D velocity field (U , V , W) and the water depth H and, from the bottom depth, the free surface S at each time step. It also solves the transport of tracers, which are classified by the software into two different categories: active tracers, such as salinity and temperature, which affect the water density and, therefore, also modify the flow field; passive tracers, such as a dye, do not affect the water density and do not affect the flow.

The major applications of TELEMAC-3D are related to the simulation of free surface flow, both for seas and rivers. The software allows representing better complex phenomena that cannot be reproduced effectively in 2D because it can take the following processes into

account:

- influence of temperature and/or salinity on density;
- bottom friction;
- influence of the Coriolis force;
- influence of weather elements: air pressure, rain or evaporation and wind;
- sources and sinks for fluid moment within the flow domain;
- simple or complex turbulence models ($k - \epsilon$) taking the effects of the Archimedean force (buoyancy) into account;
- dry areas in the computational domain: tidal flats.

The main ones are related to the marine environment through the investigations of currents induced by tides or density gradients, with or without the influence of such an external force as the wind or air pressure. It can be applied to large extent areas (on a sea scale) or smaller domains (coasts and estuaries) for the impact of sewer effluents, the study of thermal plumes or sedimentary transport. As regards the continental waters, the study of thermal plumes in rivers, the hydrodynamic behaviour or natural or artificial lakes can be mentioned as well.

The main input and output files and the wind influence in the model are the same as described in Section 3.1.1.

Theoretical aspects

The TELEMAC-3D code solves the three-dimensional hydrodynamic equations simultaneously; the following system (with an equation for W which is similar to those for U and V) is then to be solved:

$$\left\{ \begin{array}{l} \frac{\partial U}{\partial x} + \frac{\partial V}{\partial y} + \frac{\partial W}{\partial z} = 0, \quad (3.6a) \\ \frac{\partial U}{\partial t} + U \frac{\partial U}{\partial x} + V \frac{\partial U}{\partial y} + W \frac{\partial U}{\partial z} = -\frac{1}{\rho} \frac{\partial p}{\partial x} + \nu \Delta(U) + F_x, \quad (3.6b) \\ \frac{\partial V}{\partial t} + U \frac{\partial V}{\partial x} + V \frac{\partial V}{\partial y} + W \frac{\partial V}{\partial z} = -\frac{1}{\rho} \frac{\partial p}{\partial y} + \nu \Delta(V) + F_y, \quad (3.6c) \\ \frac{\partial W}{\partial t} + U \frac{\partial W}{\partial x} + V \frac{\partial W}{\partial y} + W \frac{\partial W}{\partial z} = -\frac{1}{\rho} \frac{\partial p}{\partial z} - g + \nu \Delta(W) + F_z. \quad (3.6d) \end{array} \right.$$

Where:

- h (m) is the water depth;
- U, V, Z (m/s) are three-dimensional components of velocity;
- s (s) is the time;
- g (m/s²) is the gravity acceleration;
- ν (m²/s) is the cinematic viscosity and tracer diffusion coefficients;
- x, y (m) are the horizontal space components;
- z (m) is the vertical space component;
- p (X) is the pressure;
- F_x, F_y are source terms denoting the wind, the Coriolis force and the bottom friction (or any other process being modelled by similar formulas);
- h, U, V, W and T are the unknown quantities, also known as computational variables.

The pressure is split up into a hydrostatic pressure and a dynamic pressure term:

$$p = p_{atm} + \rho_0 g (Z_S - z) + \rho_0 g \int_z^{Z_S} \frac{\Delta\rho}{\rho_0} dz + p_d \quad (3.7)$$

Where:

- p (X) is the pressure;
- p_{atm} (X) is the atmospheric pressure;
- ρ_0 (X) is the reference density;
- $\delta\rho$ (X) is the variation of density around the reference density;
- g (m/s²) is the gravity acceleration;
- Z_S (m) is the bottom depth;
- z (m) is the vertical space component;
- p_d (X) is the dynamic pressure term.

As mentioned, the tracer can be either active (temperature, salinity and, in some cases, sediment) or passive (dye) in TELEMAC-3D. The tracer evolution equation is formulated as follows:

$$\rho = \rho_{ref} [1 - (7(T - T_{ref})^2 - 750S) 10^{-6}] \quad (3.8)$$

In which: ρ_{ref} is the reference density at that temperature when the salinity S is zero, then $\rho_{ref} = 999.972 \text{ kg/m}^3$; T_{ref} is the reference temperature equal to $4 \text{ }^\circ\text{C}$. This law can only be applied if $0 \text{ }^\circ\text{C} < T < 40 \text{ }^\circ\text{C}$ and $0 \text{ g/L} < S < 42 \text{ g/L}$.

In TELEMAC-3D, the mesh structure is made up of prisms. A two-dimensional mesh is formed as in TELEMAC-2D, after which the mesh is duplicated along the vertical direction in a number of curves surfaces known as planes. Prisms are formed through the links between the meshed triangles between two planes. The computational variables are defined at every point of the three-dimensional mesh, including the bottom and surface, so these are three-dimensional variables; instead, water depth and bottom depth are defined only once along a vertical line, therefore, these are two-dimensional variables.

Physical parameter definition – Modelling turbulence

The implementation of TELEMAC-3D requires defining two models of horizontal and vertical turbulence. This involves defining horizontal and vertical viscosities rather than a single viscosity; for example, horizontal and vertical viscosities differ by several orders of magnitude in the open sea.

TELEMAC-3D offers various options for turbulence modelling, which can be combined and applied to both velocities and active and passive tracers, such as: constant viscosity model, mixing length model (vertical model), Smagorinsky model, $k - \epsilon$ model, $k - \omega$ model and Spalart-Allamaras model.

The most used ones are usually three: constant viscosity model, mixing length model (vertical model) and $k - \epsilon$ model.

The simplest turbulence model uses a constant viscosity coefficient (default option in TELEMAC-3D). Using the constant viscosity coefficient model, the horizontal and vertical turbulent viscosities are constant throughout the domain. The overall viscosity coefficient (molecular and turbulent viscosity) has a default value of 10^{-6} meters squares per second (corresponding to the molecular viscosity of water).

Using the vertical mixing length model, the vertical diffusivity of velocities is automatically computed by TELEMAC-3D using the selected mixing length model, taking or not considering the effects of density. The mixing length model expresses the turbulent viscosity (or diffusion coefficient) as a function of the mean velocity gradient and the mixing length (Prandtl's theory):

$$\nu = L_m^2 \sqrt{2D_{ij}D_{ij}} \quad (3.9)$$

Where:

$$D_{ij} = \frac{1}{2} \left(\frac{\partial \bar{U}_i}{\partial x_j} + \frac{\partial \bar{U}_j}{\partial x_i} \right) \quad (3.10)$$

The $k - \epsilon$ model is defined through a couple of equations solving the balance equations for k (turbulent energy) and ϵ (turbulent dissipation). Applying the $k - \epsilon$ model increases the calculation times compared to the constant viscosity model.

The overall viscosity coefficient has its real physical value (10^{-6} meters squares per second for molecular diffusion of water), as this is used as such by the turbulence model. Turbulent viscosity may be given by the user or determined by a model simulating the transport of turbulent quantities k (turbulent kinetic energy) and ϵ (turbulent dissipation), for which the equations are the following:

$$\left\{ \begin{array}{l} \frac{\partial k}{\partial t} + U \frac{\partial k}{\partial x} + V \frac{\partial k}{\partial y} + W \frac{\partial k}{\partial z} = \frac{\partial}{\partial x} \left(\frac{\nu_t}{\sigma_k} \frac{\partial k}{\partial x} \right) + \frac{\partial}{\partial y} \left(\frac{\nu_t}{\sigma_k} \frac{\partial k}{\partial y} \right) + \frac{\partial}{\partial z} \left(\frac{\nu_t}{\sigma_k} \frac{\partial k}{\partial z} \right) + P - G - \epsilon, \quad (3.11a) \\ \frac{\partial \epsilon}{\partial t} + U \frac{\partial \epsilon}{\partial x} + V \frac{\partial \epsilon}{\partial y} + W \frac{\partial \epsilon}{\partial z} = \frac{\partial}{\partial x} \left(\frac{\nu_t}{\sigma_\epsilon} \frac{\partial \epsilon}{\partial x} \right) + \frac{\partial}{\partial y} \left(\frac{\nu_t}{\sigma_\epsilon} \frac{\partial \epsilon}{\partial y} \right) + \frac{\partial}{\partial z} \left(\frac{\nu_t}{\sigma_\epsilon} \frac{\partial \epsilon}{\partial z} \right) \quad (3.11b) \\ + C_{1\epsilon} \frac{\epsilon}{k} [P + (1 - C_{3\epsilon})G] - C_{2\epsilon} \frac{\epsilon^2}{k}. \quad (3.11c) \end{array} \right.$$

Where:

- $k = \frac{1}{2} \overline{u'_i u'_i}$ is the turbulent kinetic energy of the fluid;
- $u'_i = U_i - \bar{u}_i$ is the i^{th} component of the fluctuation of the velocity $\mathbf{U}(U, V, W)$;
- $\epsilon = \nu \frac{\partial u'_i}{\partial x_j} \frac{\partial u'_i}{\partial x_j}$ is the dissipation of turbulent kinetic energy;
- P is a turbulent energy production term;
- G is a source term due to the gravitational forces:

$$\left\{ \begin{array}{l} P = \nu_t \left(\frac{\partial \bar{U}_i}{\partial x_j} + \frac{\partial \bar{U}_j}{\partial x_i} \right) \frac{\partial \bar{U}_i}{\partial x_j}, \quad (3.12a) \end{array} \right.$$

$$\left\{ \begin{array}{l} G = \frac{-\nu_t g}{Pr_t \rho} \frac{\partial \rho}{\partial z}, \quad (3.12b) \end{array} \right.$$

$$\left\{ \begin{array}{l} \nu_t = C_\mu \frac{k^2}{\epsilon}. \quad (3.12c) \end{array} \right.$$

- $C_\mu, Pr_t, C_{1\epsilon}, C_{2\epsilon}, C_{3\epsilon}, \sigma_k, \sigma_\epsilon$ are constants in the $k - \epsilon$ model.

3.2.2. Coastal zone modeling

Since the 2D model fails to simulate well the mid-field and far-field areas of the plume, mainly dependent on wind stress and sediment buoyancy, a three-dimensional model was used to try to obtain a better simulation of the plume.

TELEMAC-3D software requires the input and output files already described in Section 3.1.1 as mandatory, therefore, the same mesh, bottom, roughness coefficient, and initial and boundary conditions are used for the 2D model. Using a 3D mesh becomes necessary when working in a three-dimensional environment. The three-dimensional mesh, consisting of prisms possibly cut into tetrahedrons, is automatically constructed by TELEMAC-3D from a two-dimensional mesh. The software provides many tools to decide the levels of distribution along the vertical. In this model, the default value for constructing the three-dimensional mesh is used, corresponding to the classical sigma transformation. The classical sigma transformation results in a homogeneous level distribution in the vertical direction (example in Figure 3.15).

In TELEMAC-3D, the water depth is the only two-dimensional variable computed, so its processing at the boundaries is like that being performed by TELEMAC-2D. For other variables like velocities and tracers, the user has to specify which profile should be prescribed by TELEMAC-3D. The horizontal velocity profile is the same as that used in the two-dimensional simulation for velocities. On the river boundary, the velocity vector is normal to the boundary and its norm is proportional to the square root of a virtual water depth computed from the lowest point of the free surface on the boundary; on the maritime boundary, the values of U and V are read from the boundary conditions file (TPXO files). The vertical velocity profile is constant (default value) for all the liquid boundaries.

For the two-dimensional simulation, the only tracer used (dye) is a passive tracer, while for the three-dimensional simulation, the tracers used are both active and passive. The active tracers affect the flow through the hydrostatic pressure gradient term (Equation 3.8); in

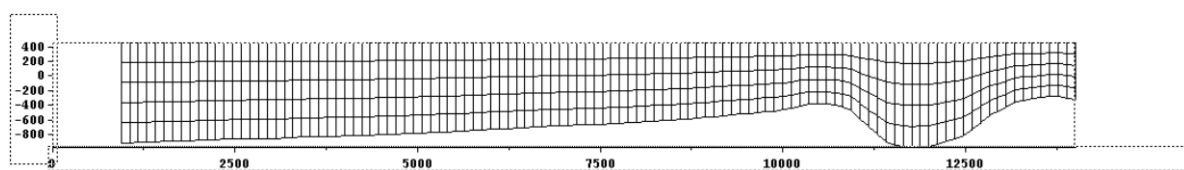


Figure 3.15: Classical sigma transformation (homogeneous distribution of levels in the vertical direction).

this equation, the ratio $\Delta\rho/\rho_0$ operates in the buoyancy source term and directly depends on the values of the active tracers. In these simulations, the salinity and temperature of the water (active tracers, which alter the density) and the dye (passive tracer, which does not alter the density) are introduced. At the boundary conditions, the tracer concentrations have a constant vertical profile.

For the three-dimensional model, the fluvial plume event of March 11, 2021, was simulated, previously tried to reproduce it in two dimensions. Unlike the 2D model, with TELEMAC-3D, it is possible to obtain more realistic simulations considering the sea salinity and the water mean temperature. From the ERA5 data and previous studies carried out on the Ofanto River on behalf of the Puglia Region, it was possible to establish a sea salt concentration of about 38 PSU (Practical Salinity Units) and a mean sea water temperature of about 12 °C for the day March 11, 2021, and an average river water temperature of about 9 °C.

Based on the horizontal turbulence model and the vertical turbulence model set for the 3D simulation, the reproduction of the flow field (and consequently of the plume dispersion phenomenon) can vary. These variations in the result occur above all in the river estuary area, characterized by a high Reynolds number. The $k - \epsilon$ model is the one that manages to obtain a good result in terms of distribution and diffusion of the tracer, but its computational burden is very high (Figure 3.17b). Slightly different results in terms of tracer distribution and diffusion are obtained using different horizontal and vertical turbulence models (Constant viscosity model and Mixing length model). These results are reported in Appendix B.2.3. In particular, the simulation performed with the Mixing length turbulence model reproduces a result quite similar to that obtained with the $k - \epsilon$ turbulence model, but performed in a shorter computational time.

The best set of physical parameters resulting from the calibration exercise of the TELEMAC-3D model (comparing the satellite image processed with SNAP with the product of the simulations) are shown in Table 3.3.

Table 3.4 shows the five vertical layers applied to the 3D mesh. Since only the surface data detected by satellites are available, the results shown in the Figures of this Section always refer to the most superficial layer, i.e. layer 5.

The satellite image of March 11 2021, at 09:50 with the relative solid concentrations in suspension obtained from the SSC formula from [Zhang et al., 2014] (Figure 3.17a) can be compared with the best result obtained with TELEMAC-3D by calibrating the parameters according to the satellite image (Figure 3.17b). Since the best result in 2D was the one obtained with the wind recorded in Bisceglie, it was decided to use this anemometric

Table 3.3: The best set of physical parameters resulting from the calibration exercise of the TELEMAC-3D model.

Mesh level of distribution along the vertical	Classical sigma transformation
Number of horizontal levels	5
Horizontal turbulence model	$k - \epsilon$ model
Vertical turbulence model	$k - \epsilon$ model
Tidal flats	Yes
Time step	1 s
Manning's coefficient for the seabed	0.025
Manning's coefficient for the river	0.028; 0.04
Tide (TPXO) at the shooting time	ebb
Coefficient of wind influence	Variable with wind speed
Constant inflow dye concentration	55 mg/L
Seawater salinity	38 PSU
Mean sea temperature	12 °C
Mean river temperature	9 °C

Table 3.4: Vertical layers in the 3D model.

Layer	Z min [m]	Z max
Layer 5	-0.76	6.78
Layer 4	-7.78	6.78
Layer 3	-15.19	6.78
Layer 2	-22.59	6.78
Layer 1	-30	6.78

recording for the three-dimensional simulation. The calibration objects in the 3D module are the turbulence models, the river water temperature (calibration between 9 and 10 °C) and the marine salinity (calibration between 37 and 38 PSU).

Figures 3.16a and 3.16b show the simulations of salinity concentrations and water temperature in the most superficial layer of the mesh (surface layer thickness: 0.76 meters; it is noted that the freshwater and its temperature predominate the mouth area and persist with higher concentrations and temperatures up to 5 kilometres offshore until they merge with the sea value (38 PSU, 12 °C and 9 °C after calibration).

Figure 3.17b shows the results obtained in the most superficial layer of the mesh (surface layer thickness: 0.76 meters). Comparing Figure 3.17a and Figure 3.17b, it can be seen

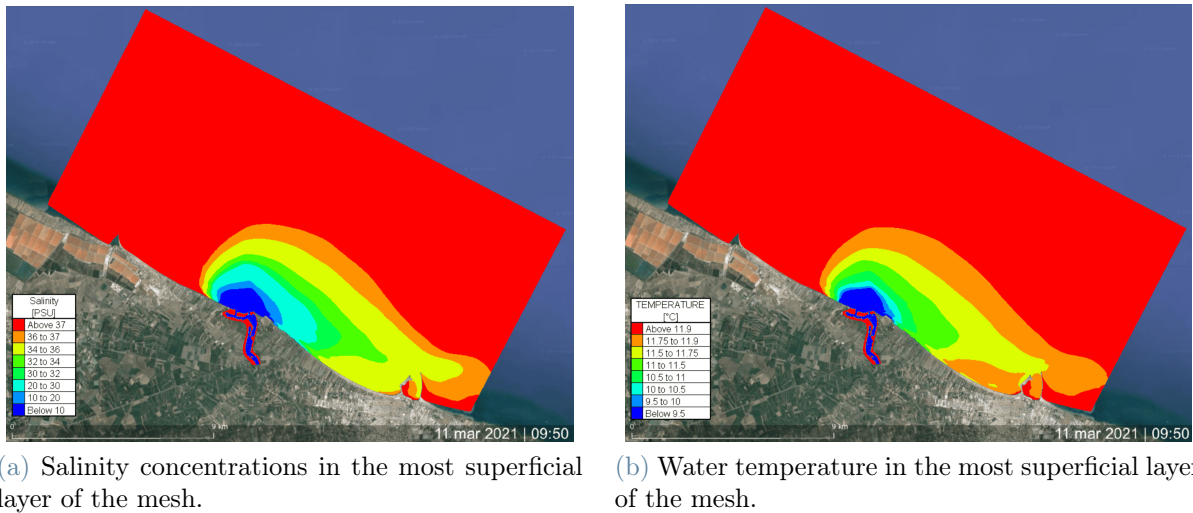


Figure 3.16: Salinity concentrations and water temperature in the most superficial layer of the mesh (surface layer thickness: 0.76 meters) using $k - \epsilon$ turbulence model.

that the three-dimensional model is able to simulate the fluvial plume also in its mid-field and far-field areas, managing to simulate the distances reached offshore by the plume with an error of a few hundred meters in the mid-field area (about 5200 meters simulated) and with an even minor error in the far-field area near the port of Barletta (about 1800 meters simulated). The far-field area extends alongshore even beyond the port of Barletta, but there are no satellite images that day to carry out investigations. From the literature already described in Section 2.1, it is known that many fluvial plume far-fields can expand even for hundreds of kilometres alongshore; considering that the port of Barletta is already 10 kilometres from the Ofanto River's mouth, the plume could extend for tens of kilometres in South-East direction, due to the buoyancy of the sediments, to the wind stress oriented in this direction, to the effect of the Earth's rotation and coastal currents in this direction affecting the Southern Adriatic Sea.

Figure 3.17a shows that the concentrations vary by even more than an order of magnitude between the near-field and far-field areas; this is also confirmed by the model, even if it tends to overestimate the tracer concentrations. This may be because the tracer behaves like a dye and not like sediment; suspended sediments have their own density and buoyancy, which depends on their critical shear velocity.

Table 3.5 reports the comparison between the satellite image and the best three-dimensionally simulated result, listing the offshore plume distance, the offshore plume distance near Barletta harbour and the alongshore plume distance beyond Barletta harbour. Furthermore, the corresponding near-field tracer concentrations, the far-field tracer concentrations near

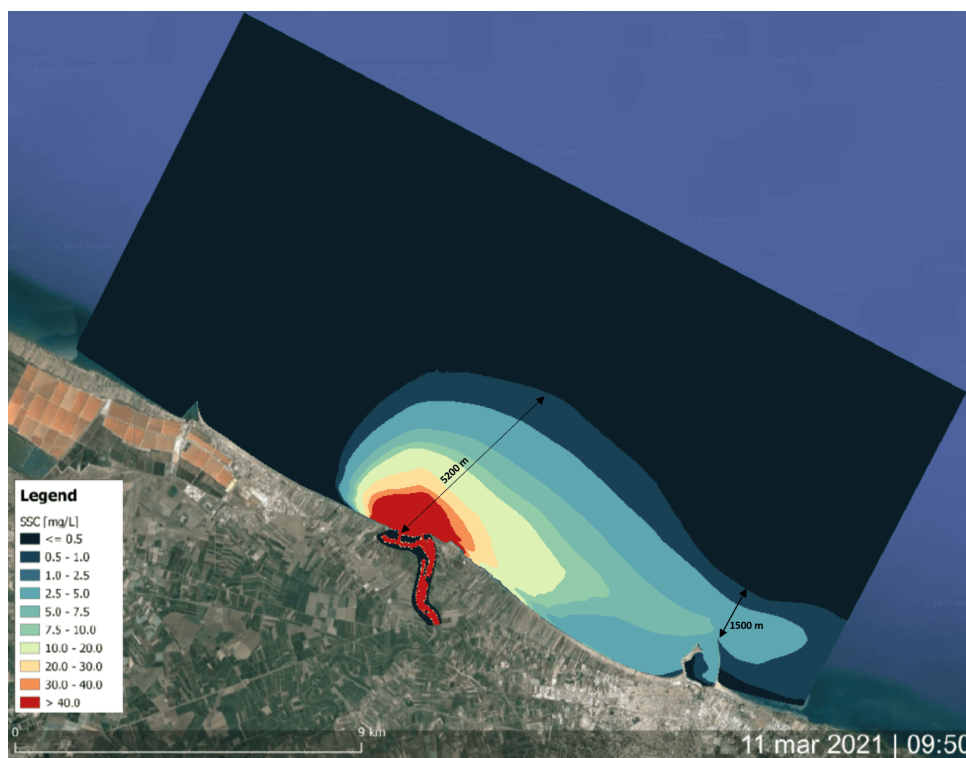
Table 3.5: Comparison between satellite data and 3D model.

	SSC (satellite)	3D Model
Offshore plume distance	4700 m	5200 m
Offshore plume distance (near Barletta harbour)	1850 m	1500 m
Alongshore plume distance (beyond Barletta harbour)	>12 km	>12 km
Near-field tracer concentrations	≥ 40 mg/L	≥ 40 mg/L
Far-field tracer concentrations (near Barletta harbour)	1 - 2.5 mg/L	2.5 - 5 mg/L
Far-field tracer concentrations (beyond Barletta harbour)	0.5 - 2.5 mg/L	0.5 - 2.5 mg/L

Barletta harbour and the far-field tracer concentrations beyond Barletta harbour are listed. The distances of the river plume captured by satellite with the one simulated three-dimensionally differ by 500 meters for the offshore plume distance in the mid-field area and by 350 meters in the far-field area near the port of Barletta. The concentrations differ by about 2.5-5 mg/L in the far-field areas while in the near-field area they exceed 40 mg/L both for the image with the SSC formula applied and for the 3D model.



(a) Suspended sediment concentration on March 11, 2021, calculated with the formula calibrated in [Zhang et al., 2014].



(b) 3D simulation of the river plume, March 11, 2021 (representation of the concentrations in the most superficial layer of the mesh).

Figure 3.17: Comparison between the satellite image with the SSC formula applied and the 3D simulation using $k - \epsilon$ turbulence model.

Conclusions and future developments

A fluvial plume phenomenon is a widespread event in marine coastal areas throughout the world. Even considering rivers with relatively modest flow rates, the plume can have an offshore horizontal spatial extension of hundreds or thousands of meters and an alongshore horizontal spatial extension of tens or hundreds of kilometres. Being an event characterized, many times, by considerable dimensions, it plays an important role in the land-ocean interaction because the river discharge carries freshwater to the sea (at a certain temperature) mixed with suspended solid sediments, nutrients and anthropogenic pollutants. Accordingly, river plumes influence the coastal maritime environment, modifying its physics, biology and geochemistry; in fact, the main influences in the presence of river plumes include changes in several fields: the seabed morphology, seawater stratification, coastal currents, primary production and biogeochemical cycle.

The river plume is a dynamic system influenced by processes with a very large temporal and spatial scale. It is very variable due to the river flow rate, the type of river mouth, the weather and sea conditions (salinity, temperature, wind, tide, waves height and direction), the coastal currents, the latitude in which it is located and the seabed bathymetry. These conditions play different roles in the plume field zones, i.e. they influence the formation, size, direction and persistence of the near-field, mid-field and far-field zones.

This thesis aimed to study the fluvial plume phenomenon and to understand if, with the help of satellite images, it was possible to create a hydrodynamic model able to replicate the plume events captured by satellite.

The area of interest was the Ofanto River mouth in Puglia in the time period from July 1 2019, to March 31, 2021. Since the phenomenon of the river plume is captured by optical satellites even daily (even if sometimes the cloud cover didn't allow it), it was possible to analyze and understand how the flow rate and weather conditions influence the plume. A logarithmic relationship was found between river discharge and Tidal Plume Front (TPF) dimension, which increases in size and expands offshore as a function of the flow, i.e. the creation and expansion of the plume are linked to the river discharge, which, increasing, enlarges the shape and distance of the TPF. No correlation with the discharge was found

for how much it concerns the far-field zone: this is the region beyond the mid-field where the plume water has lost all memory of the inflow momentum of the river discharge but is still distinct from the ambient receiving water; this region can extend even for hundreds of kilometres from the river mouth and is mainly affected by the action of the wind. Studying the influence of the wind on the plume phenomenon, a linear correlation was found between the fluvial plume direction and the wind direction. In fact, the direction of the plume always agrees with the direction of the wind, except for two minimal events in which the tide played a decisive role.

After having analyzed the main factors that modify the Ofanto River plume, first of all, a 2D river model was developed and calibrated by varying the roughness coefficients against the observations of satellite data. The discharge was extracted at three kilometres from the mouth, in such a way as to obtain the flows downstream of the last hydrometric station available (San Samuele di Cafiero, 18 kilometres inland); after that, a 2D coastal model was developed which allowed the simulation of the river plume event. For the 2D coastal model, despite knowing the importance of salinity from the literature, it had to be excluded from the simulation because the mixing of freshwater and saltwater near the mouth is not well reproduced by the 2D model, creating a saline wall that did not allow to the tracer, used to reproduce the plume, to expand offshore. The results of the 2D simulations carried out for the event of March 11, 2021, and for the event of April 24, 2020, show an accurate reproduction of the Tidal Plume Front while failing to reproduce the plume in its mid-field and, above all, in its far-field areas.

Since salinity and water temperature vary significantly between river water and seawater, a 3D model has been implemented to consider as many variables as possible. The tidal event is replicated through the TPXO database, the wind used is that recorded by the anemometric station of Bisceglie (the closest, on the coast, to the domain available for the entire research period), the flow rate extracted from the fluvial model and two active tracers such as salinity and temperature and a passive tracer (dye) were implemented in the 3D model. The result of the three-dimensional simulation shows that the introduction of salinity and water temperature is essential to simulate the mid-field and the far-field plume areas; in fact, the offshore distances of both zones are simulated with an error of a few hundred meters for the mid-field and with an even smaller error for the far-field. Not having in-situ sampling, the surface concentrations of suspended solids were calculated using the spectral bands of the satellite image. From the comparison with the model, it is not possible to perfectly simulate the concentrations in the far-field; this can be due to several factors:

- the possible inaccuracy of the satellite image with the SSC formula applied, which

acts as a filter of the spectral bands but is calibrated for the seawaters of Hong Kong Bay;

- plume simulation using a tracer and not sediments;
- to neglect the phenomena related to the suspended solid transport, such as the mean diameter, density and deposition of the sediments;
- the accuracy of horizontal and vertical turbulence models;
- not having introduced wind-generated water waves in the model.

Having few in-situ sampled data available and relying mainly on satellite images alone, it is possible to simulate the phenomena of fluvial plumes through finite element fluid-dynamics computational models. Satellite data can guide the modeller to understand the critical variables acting on the plume, which models to adopt (2D or 3D) and how to choose parameters (wind direction, concentration of suspended solids).

Future developments that can be performed are:

- to use a new equation for the estimation of suspended solids using satellite sensors, which must be calibrated and validated for the seawaters of the area of interest thanks to in-situ sampling;
- to reproduce a 3D hydromorphodynamic computational model, i.e. implementing the solid transport in the 3D hydrodynamic model, but this becomes feasible only after in-situ sampling and analysis of the Ofanto River sediments;
- to implement wind-generated water waves in the three-dimensional model, but the simulation requires a high computational burden;
- for all plume simulations that took place after May 2022, to use the wind recorded by the anemometric station of Barletta, which came into operation that month and is located near the port of Barletta (south-eastern area of the coastal domain), therefore with winds remarkably similar to those in action in the model.

Bibliography

- Aufide (fleuve) — Wikipedia, the free encyclopedia, 2020. URL [https://en.wikipedia.org/wiki/Ofanto#/media/File:Aufide_\(fleuve\).png](https://en.wikipedia.org/wiki/Ofanto#/media/File:Aufide_(fleuve).png).
- L. O. Amoudry and A. J. Souza. Deterministic coastal morphological and sediment transport modeling: A review and discussion. *Reviews of Geophysics*, 49(2), 2011.
- M. Caldara, L. Pennetta, and O. Simone. Holocene Evolution of the Salpi Lagoon (Puglia, Italy). *Journal of Coastal Research*, 36(sp1):124 – 133, 2002. doi: 10.2112/1551-5036-36.sp1.124. URL <https://doi.org/10.2112/1551-5036-36.sp1.124>.
- J. Cochran and F. Kelly. Low-frequency circulation on the texas-louisiana continental shelf. *Journal of Geophysical Research: Oceans*, 91(C9):10645–10659, 1986.
- G. J. de Boer, J. D. Pietrzak, and J. C. Winterwerp. Using the potential energy anomaly equation to investigate tidal straining and advection of stratification in a region of freshwater influence. *Ocean Modelling*, 22(1):1–11, 2008. ISSN 1463-5003. doi: <https://doi.org/10.1016/j.ocemod.2007.12.003>. URL <https://www.sciencedirect.com/science/article/pii/S1463500307001631>.
- G. J. de Boer, J. D. Pietrzak, and J. C. Winterwerp. Sst observations of upwelling induced by tidal straining in the rhine rofi. *Continental Shelf Research*, 29(1):263–277, 2009.
- R. M. Dellisanti. *RParco Naturale Regionale Fiume Ofanto*. Stilo Editrice, 2021.
- G. Egbert and S. Erofeeva. Efficient inverse modeling of barotropic ocean tides. *J. Atmos. Ocean. Tech.*, 19:183–204, 02 2002. doi: 10.1175/1520-0426(2002)019<0183:EIMOBO>2.0.CO;2.
- D. A. Fong and W. R. Geyer. Response of a river plume during an upwelling favorable wind event. *Journal of Geophysical Research: Oceans*, 106(C1):1067–1084, 2001.
- R. W. Garvine. Estuary plumes and fronts in shelf waters: A layer model. *Journal of Physical Oceanography*, 17(11):1877–1896, 1987.

- W. R. Geyer, A. C. Lavery, M. E. Scully, and J. H. Trowbridge. Mixing by shear instability at high Reynolds number. *Geophysical Research Letters*, 37(22), 2010.
- S. Heise and U. Förstner. Risk assessment of contaminated sediments in river basins—theoretical considerations and pragmatic approach. *Journal of Environmental Monitoring*, 9(9):943–952, 2007.
- J.-M. Hervouet. *Hydrodynamics of free surface flows: modelling with the finite element method*. John Wiley & Sons, 2007.
- K. Hessner, A. Rubino, P. Brandt, and W. Alpers. The rhine outflow plume studied by the analysis of synthetic aperture radar data and numerical simulations. *Journal of physical oceanography*, 31(10):3030–3044, 2001.
- R. D. Hetland. The effects of mixing and spreading on density in near-field river plumes. *Dynamics of Atmospheres and Oceans*, 49(1):37–53, 2010.
- B. M. Hickey, R. M. Kudela, J. Nash, K. W. Bruland, W. T. Peterson, P. MacCready, E. J. Lessard, D. A. Jay, N. S. Banas, A. M. Baptista, et al. River influences on shelf ecosystems: introduction and synthesis, 2010.
- C. Hissler and J.-L. Probst. Chlor-alkali industrial contamination and riverine transport of mercury: Distribution and partitioning of mercury between water, suspended matter, and bottom sediment of the thur river, france. *Applied Geochemistry*, 21(11):1837–1854, 2006.
- A. R. Horner-Devine, D. A. Jay, P. M. Orton, and E. Y. Spahn. A conceptual model of the strongly tidal columbia river plume. *Journal of Marine Systems*, 78(3):460–475, 2009.
- A. R. Horner-Devine, R. D. Hetland, and D. G. MacDonald. Mixing and transport in coastal river plumes. *Annual Review of Fluid Mechanics*, 47:569–594, 2015.
- R. Houghton, R. Chant, A. Rice, and C. Tilburg. Salt flux into coastal river plumes: Dye studies in the delaware and hudson river outflows. *Journal of Marine Research - J MAR RES*, 67:731–756, 11 2009. doi: 10.1357/002224009792006142.
- G. Jones, J. Nash, and R. Doneker. Buoyant surface discharges into water bodies. i: Flow classification and prediction methodology. *Journal of Hydraulic Engineering-asce - J HYDRAUL ENG-ASCE*, 133, 09 2007. doi: 10.1061/(ASCE)0733-9429(2007)133:9(1010).

- H. J. Kanbar, E. Montargès-Pelletier, B. Losson, I. Bihannic, R. Gley, A. Bauer, F. Villieras, L. Manceau, A. G. El Samrani, V. Kazpard, et al. Iron mineralogy as a fingerprint of former steelmaking activities in river sediments. *Science of the Total Environment*, 599:540–553, 2017.
- L. F. Kilcher and J. D. Nash. Structure and dynamics of the columbia river tidal plume front. *Journal of Geophysical Research: Oceans*, 115(C5), 2010.
- L. F. Kilcher, J. D. Nash, and J. N. Moum. The role of turbulence stress divergence in decelerating a river plume. *Journal of Geophysical Research: Oceans*, 117(C5), 2012.
- N. Kobayashi, G. R. Tomasicchio, and B. Brunone. Partial standing waves on a steep slope. *Journal of Coastal Research*, pages 379–384, 2000.
- S. J. Lentz and K. R. Helfrich. Buoyant gravity currents along a sloping bottom in a rotating fluid. *Journal of Fluid Mechanics*, 464:251–278, 2002.
- J. Lepesqueur, R. Hostache, N. Martínez-Carreras, E. Montarges-Pelletier, and C. Hissler. Sediment transport modelling in riverine environments: on the importance of grain-size distribution, sediment density and boundary conditions. *Hydrology and Earth System Sciences Discussions*, pages 1–24, 11 2018. doi: 10.5194/hess-2018-511.
- D. G. MacDonald, L. Goodman, and R. D. Hetland. Turbulent dissipation in a near-field river plume: A comparison of control volume and microstructure observations with a numerical model. *Journal of Geophysical Research: Oceans*, 112(C7), 2007.
- R. M. McCabe, B. M. Hickey, and P. MacCready. Observational estimates of entrainment and vertical salt flux in the interior of a spreading river plume. *Journal of Geophysical Research: Oceans*, 113(C8), 2008.
- J. D. Milliman and K. L. Farnsworth. *River discharge to the coastal ocean: a global synthesis*. Cambridge University Press, 2013.
- S. P. Murray. An observational study of the mississippi-atlafalaya coastal plume. 1998.
- J. D. Nash, L. F. Kilcher, and J. N. Moum. Structure and composition of a strongly stratified, tidally pulsed river plume. *Journal of Geophysical Research: Oceans*, 114 (C2), 2009.
- Y. Onishi, R. Serne, E. Arnold, C. Cowan, and F. Thompson. Critical review: Radionuclide transport, sediment transport, and water quality mathematical modeling; and radionuclide adsorption/desorption mechanisms. 1981.

- C. R. Orsino, Scirocco. *Interventi ripristino, recupero e gestione dell'area umida costiera in prossimità della foce del Fiume Ofanto dei comuni di Barletta e Margherita di Savoia*. 2020.
- L. Pennetta. Ricerche sull'evoluzione recente del delta dell'ofanto. *Boll. Mus. St. Nat. Lunigiana*, 6:41–45, 1988.
- M. Pritchard and D. A. Huntley. A simplified energy and mixing budget for a small river plume discharge. *Journal of Geophysical Research: Oceans*, 111(C3), 2006.
- S. Rijnsburger, R. P. Flores, J. D. Pietrzak, A. R. Horner-Devine, A. J. Souza, and F. Zijl. The evolution of plume fronts in the rhine region of freshwater influence. *Journal of Geophysical Research: Oceans*, 126(7):e2019JC015927, 2021.
- J. Simpson, W. Bos, F. Shirmer, A. Souza, T. Rippeth, S. Jones, and D. Hydes. Periodic stratification in the rhine rofi in the north sea. *Oceanologica Acta*, 16:23–32, 01 1993.
- P. J. Smith, S. L. Dance, and N. K. Nichols. A hybrid data assimilation scheme for model parameter estimation: Application to morphodynamic modelling. *Computers & fluids*, 46(1):436–441, 2011.
- W. D. Smyth, J. N. Moum, and D. R. Caldwell. *Journal of Physical Oceanography*, (8): 1969 – 1992. doi: [https://doi.org/10.1175/1520-0485\(2001\)031](https://doi.org/10.1175/1520-0485(2001)031).
- K. E. Trenberth, L. Smith, T. Qian, A. Dai, and J. Fasullo. Estimates of the global water budget and its annual cycle using observational and model data. *Journal of Hydrometeorology*, 8(4):758–769, 2007.
- F. Verspecht, T. Rippeth, M. Howarth, A. Souza, J. Simpson, and H. Burchard. Processes impacting on stratification in a region of freshwater influence: Application to liverpool bay. *Journal of Geophysical Research*, 114, 11 2009. doi: 10.1029/2009JC005475.
- A. E. Yankovsky and D. C. Chapman. A simple theory for the fate of buoyant coastal discharges. *Journal of Physical oceanography*, 27(7):1386–1401, 1997.
- P. Zhang, O. W. Wai, X. Chen, J. Lu, and L. Tian. Improving sediment transport prediction by assimilating satellite images in a tidal bay model of hong kong. *Water*, 6(3):642–660, 2014.
- Z. Zhang and R. Hetland. A numerical study on convergence of alongshore flows over the texas-louisiana shelf. *Journal of Geophysical Research: Oceans*, 117(C11), 2012.

A | Appendix Part I

A.1. Satellite images



Figure A.1: Date: December 16, 2019, at 09:26. Instrument: Dove Classic (PS2). Pixel resolution: 3 meters.



Figure A.2: Date: December 25, 2019, at 07:41. Instrument: Dove Classic (PS2). Pixel resolution: 3 meters.

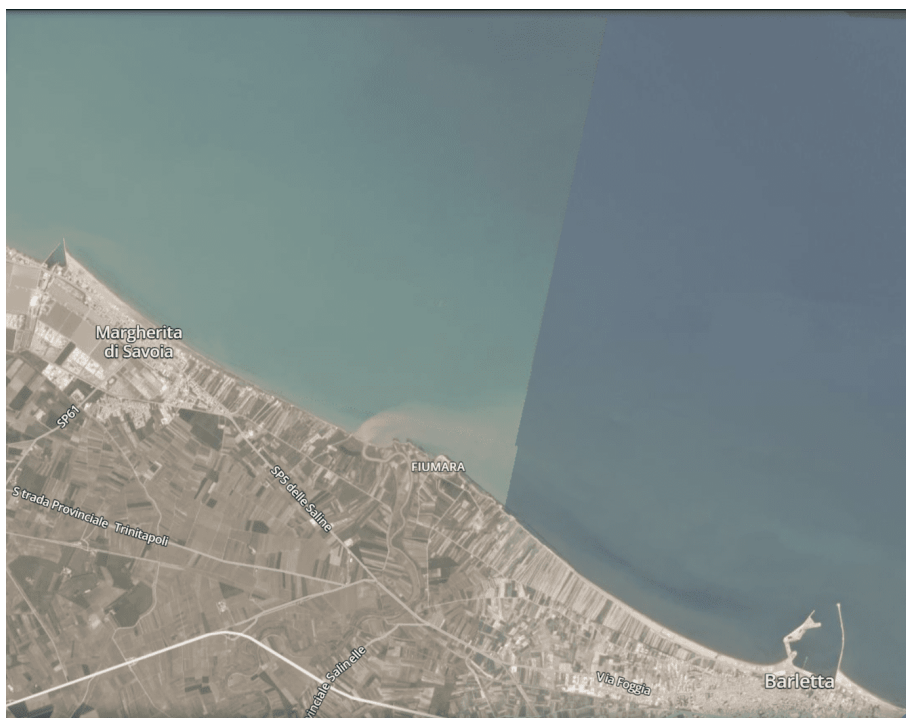


Figure A.3: Date: March 29, 2020, at 09:25. Instrument: Dove Classic (PS2). Pixel resolution: 3 meters.



Figure A.4: Date: April 24, 2020, at 09:40. Instrument: Sentinel-2B. Pixel resolution: 10 meters.

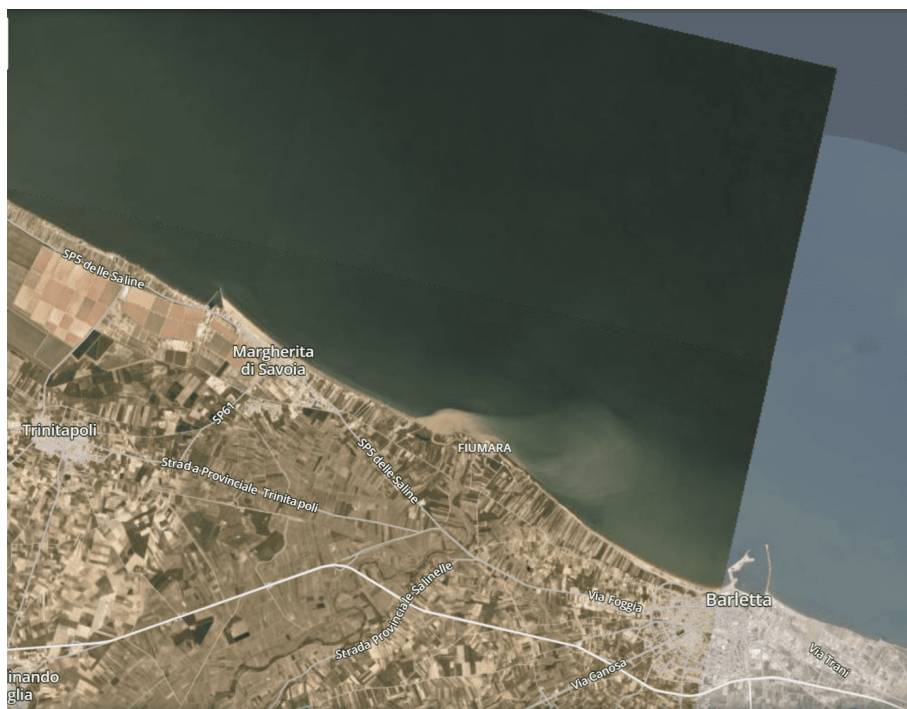


Figure A.5: Date: April 25, 2020, at 09:27. Instrument: Dove Classic (PS2). Pixel resolution: 3 meters.



Figure A.6: Date: April 26, 2020, at 09:25. Instrument: Dove Classic (PS2). Pixel resolution: 3 meters.

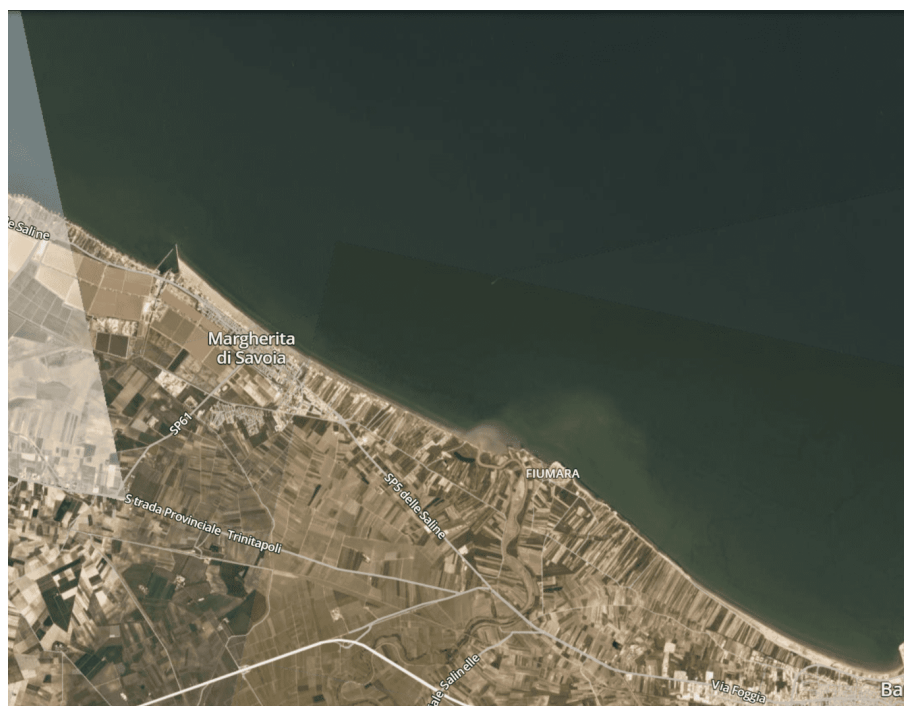


Figure A.7: Date: April 27, 2020, at 09:27. Instrument: Dove Classic (PS2). Pixel resolution: 3 meters.



Figure A.8: Date: May 22, 2020, at 09:50. Instrument: Sentinel-2A. Pixel resolution: 10 meters.



Figure A.9: Date: May 23, 2020, at 09:25. Instrument: Dove Classic (PS2). Pixel resolution: 3 meters.



Figure A.10: Date: May 25, 2020, at 07:20. Instrument: Dove Classic (PS2). Pixel resolution: 3 meters.



Figure A.11: Date: December 05, 2020, at 09:53. Instrument: Dove Classic (PS2). Pixel resolution: 3 meters.



Figure A.12: Date: December 10, 2020, at 09:14. Instrument: Dove R (PS2.SD). Pixel resolution: 3 meters.



Figure A.13: Date: January 14, 2021, at 09:43. Instrument: Sentinel-2A. Pixel resolution: 10 meters.



Figure A.14: Date: January 14, 2021, at 09:22. Instrument: Dove Classic (PS2). Pixel resolution: 3 meters.



Figure A.15: Date: February 03, 2021, at 09:26. Instrument: Dove Classic (PS2). Pixel resolution: 3 meters.

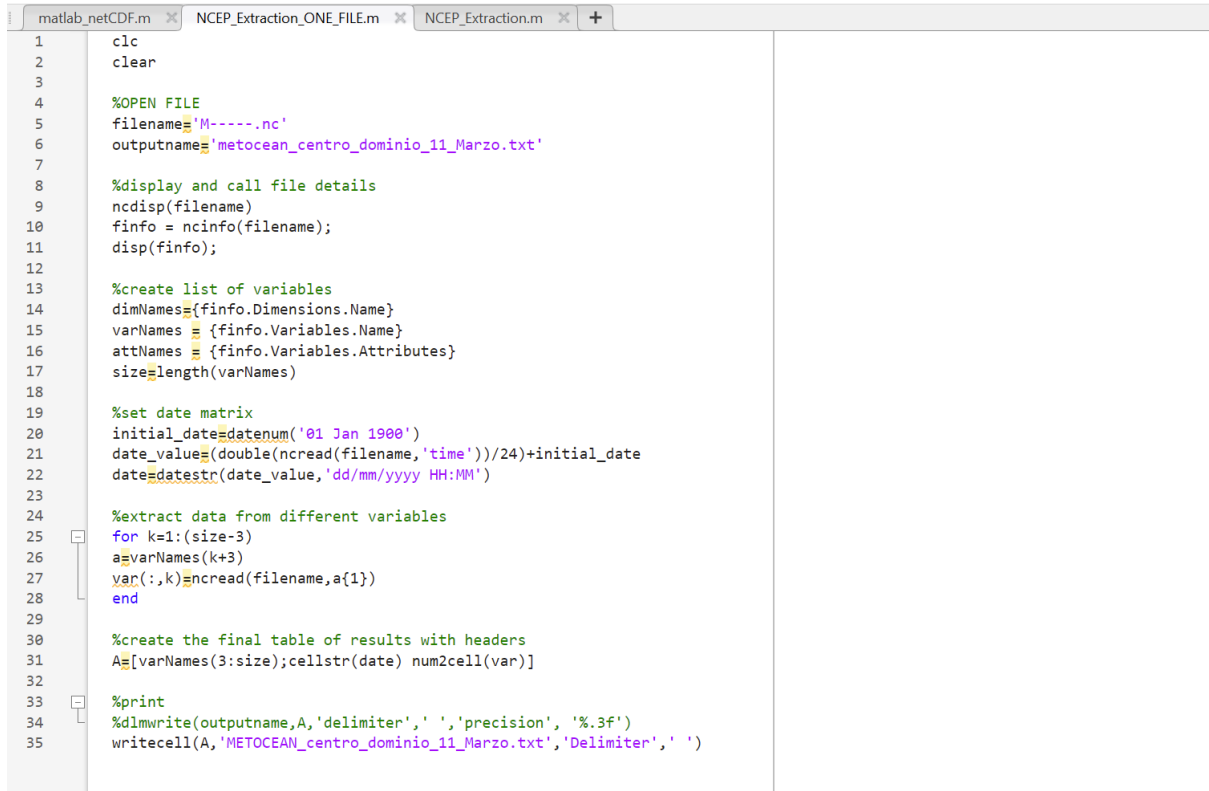


Figure A.16: Date: February 18, 2021, at 09:40. Instrument: Sentinel-2B. Pixel resolution: 10 meters.



Figure A.17: Date: March 11, 2021, at 09:50. Instrument: Super Dove (PSB.SD). Pixel resolution: 3 meters.

A.2. Matlab code



```

1  clc
2  clear
3
4  %OPEN FILE
5  filename='M-----.nc'
6  outputname='metocean_centro_dominio_11_Marzo.txt'
7
8  %display and call file details
9  ncdisp(filename)
10 finfo = ncinfo(filename);
11 disp(finfo);
12
13 %create list of variables
14 dimNames={finfo.Dimensions.Name}
15 varNames = {finfo.Variables.Name}
16 attNames = {finfo.Variables.Attributes}
17 size=length(varNames)
18
19 %set date matrix
20 initial_date=datetime('01 Jan 1900')
21 date_value=(double(ncread(filename,'time'))/24)+initial_date
22 date=datestr(date_value,'dd/mm/yyyy HH:MM')
23
24 %extract data from different variables
25 for k=1:(size-3)
26     a=varNames(k+3)
27     var(:,k)=ncread(filename,a{1})
28 end
29
30 %create the final table of results with headers
31 A=[varNames(3:size);cellstr(date) num2cell(var)]
32
33 %print
34 %dlmwrite(outputname,A,'delimiter',' ','precision', '%.3f')
35 writecell(A,'METOCEAN_centro_dominio_11_Marzo.txt','Delimiter',' ')

```

Figure A.18: Matlab code to extract ERA5 data.

B | Appendix Part II

B.1. River model

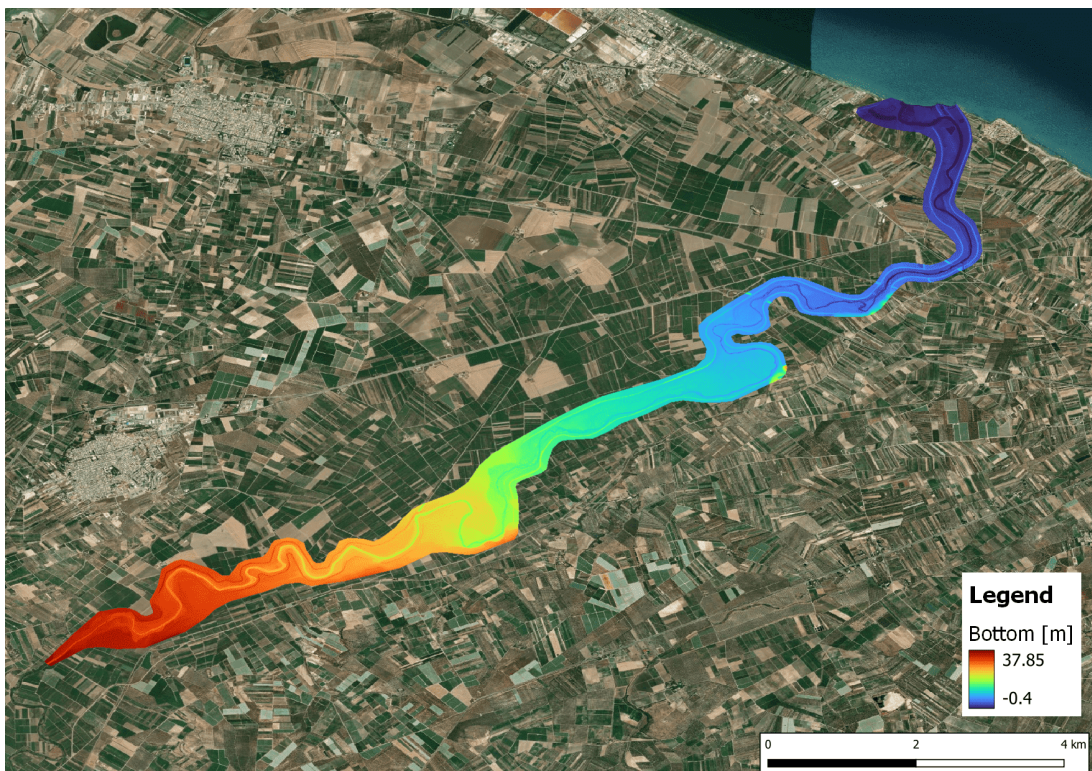


Figure B.1: River bottom.

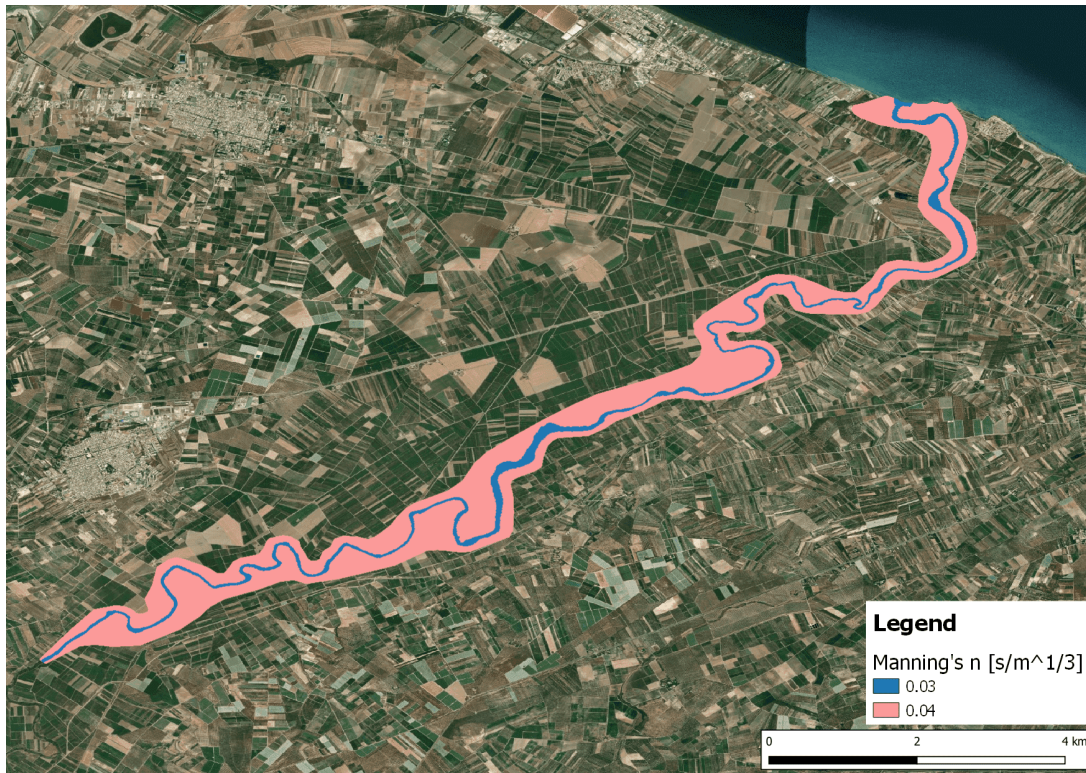


Figure B.2: Simulation 1 Manning's coefficients.



Figure B.3: Simulation 2 Manning's coefficients.

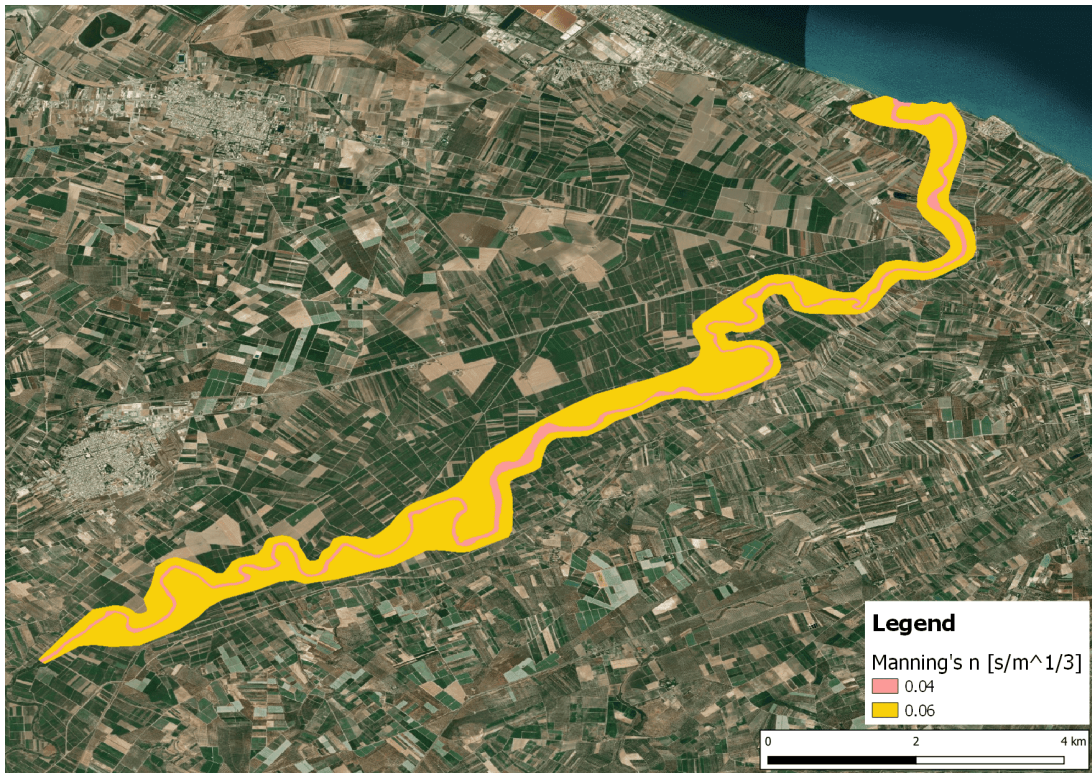


Figure B.4: Simulation 3 Manning's coefficients.

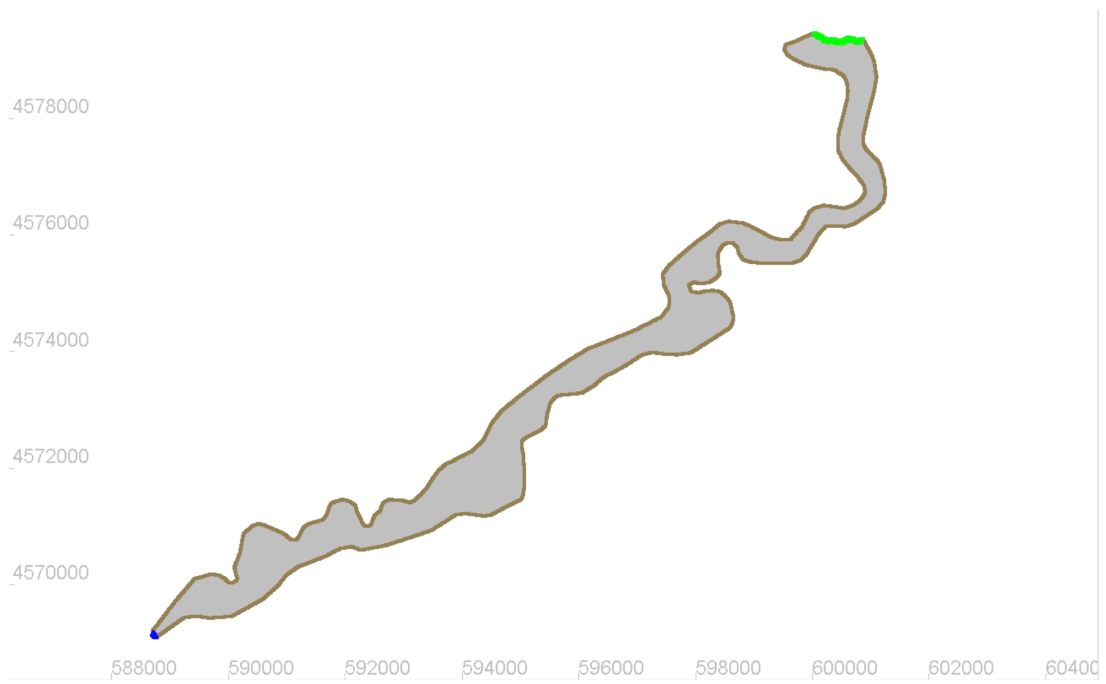


Figure B.5: River model boundary conditions.

B.1.1. TELEMAC-2D river model code

```

/-----
/ Ofanto river
/-----
TITLE ='Ofanto river'
PARALLEL PROCESSORS=12
BOTTOM SMOOTHINGS =1
FRICTION COEFFICIENT =0.04
LAW OF BOTTOM FRICTION =4
TURBULENCE MODEL =3
/-----
/ EQUATIONS, BOUNDARY CONDITIONS
/-----
PRESCRIBED FLOWRATES =999;999
PRESCRIBED ELEVATIONS =0;1
VELOCITY PROFILES =5;1
OPTION FOR LIQUID BOUNDARIES =2;2
/-----
/ EQUATIONS, INITIAL CONDITIONS
/-----
COMPUTATION CONTINUED =YES
PREVIOUS COMPUTATION FILE ='8 MARZO INITIAL CONDITIONS.slf'
/-----
/ CONTROL SECTIONS
/-----
PRINTING CUMULATED FLOWRATES = yes
SECTIONS INPUT FILE = Control Section.dat
SECTIONS OUTPUT FILE = Control Section Output RUN 3.dat
/-----
/ INPUT-OUTPUT, FILES
/-----
LIQUID BOUNDARIES FILE ='liquid boundary 3gg Q.lqd'
GEOMETRY FILE ='GEOMETRY.slf'
STEERING FILE ='telemac ofanto river.cas'

```

```
BOUNDARY CONDITIONS FILE ='mesh Ofanto BC.cli'  
RESULTS FILE ='RESULTS RUN 3 Ofanto river.slf'  
/  
/ INPUT-OUTPUT, GRAPHICS AND LISTING  
/  
LISTING PRINTOUT PERIOD =20  
INFORMATION ABOUT SOLVER =YES  
GRAPHIC PRINTOUT PERIOD =120  
VARIABLES FOR GRAPHIC PRINTOUTS =U,V,S,H,F  
MASS-BALANCE =YES  
/  
/ NUMERICAL PARAMETERS  
/  
CONTINUITY CORRECTION =true  
TIME STEP =0.5  
NUMBER OF TIME STEPS =514800  
DISCRETIZATIONS IN SPACE =11;11  
SUPG OPTION =1;1  
TIDAL FLATS =true  
TYPE OF ADVECTION =1;5  
TREATMENT OF THE LINEAR SYSTEM = 1  
FREE SURFACE GRADIENT COMPATIBILITY = 0.9  
/  
/ TIME  
/  
INITIAL TIME SET TO ZERO: YES  
ORIGINAL DATE OF TIME: 2021 ; 03 ; 09  
ORIGINAL HOUR OF TIME: 00 ; 00 ; 00  
GEOGRAPHIC SYSTEM:2  
ZONE NUMBER IN GEOGRAPHIC SYSTEM: 33
```

B.1.2. TELEMAC-2D river model results



Figure B.6: Upstream area satellite image.



Figure B.7: Upstream area Simulation 3.



Figure B.8: Central area satellite image.



Figure B.9: Central area Simulation 3.



Figure B.10: Downstream area satellite image.



Figure B.11: Downstream area Simulation 3.

B.2. Coastal model

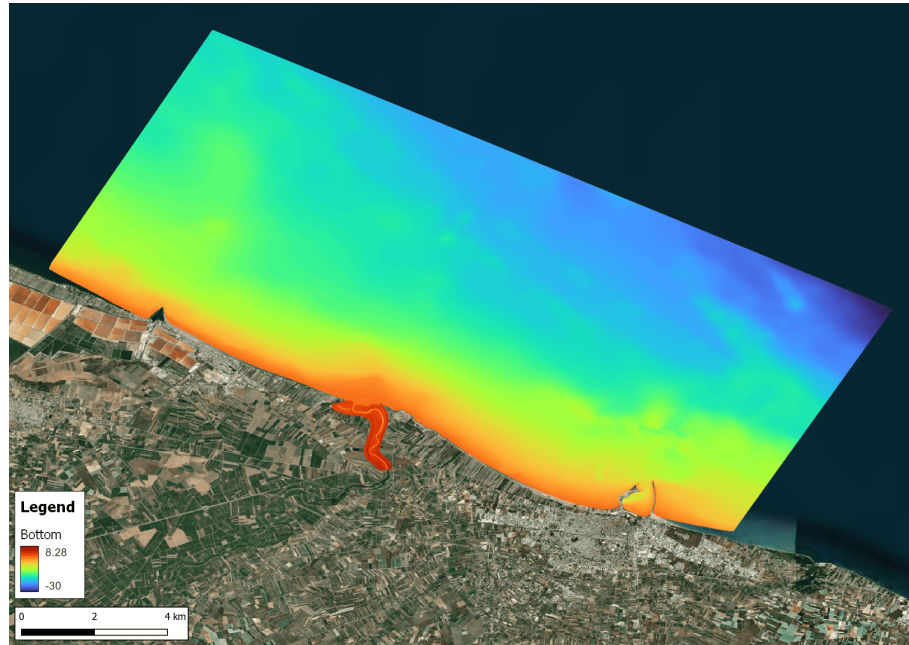


Figure B.12: Coastal model bottom.



Figure B.13: Coastal model Manning's coefficients.

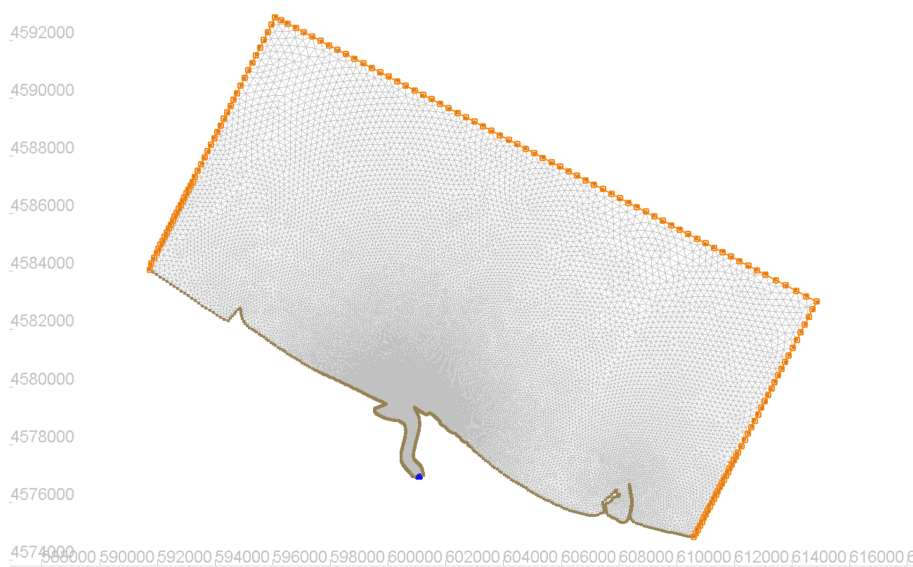


Figure B.14: Coastal model boundary conditions.

B.2.1. TELEMAC-2D coastal model code

```

TITLE = 'Coastal 2D model'
PARALLEL PROCESSORS: 12
OPTION FOR LIQUID BOUNDARIES:2;2
OPTION FOR TIDAL BOUNDARY CONDITIONS:0;1
PRESCRIBED ELEVATIONS =999;999
VELOCITY PROFILES =5;2
PRESCRIBED VELOCITIES =999;999
PRESCRIBED FLOWRATES = 200; 0

/—/
/INPUT
/—/

LIQUID BOUNDARIES FILE ='Portata 3gg 11 Mar 3km foce.lqd'
COMPUTATION CONTINUED =YES
PREVIOUS COMPUTATION FILE ='NEW INITIAL CONDITIONS 8 MAR.slf'
GEOMETRY FILE= 'GEOMETRY.slf'
BOUNDARY CONDITIONS FILE= 'mesh OLTRE PORTO BC.cli'
RESULTS FILE: 'HYDRO Bisceglie wind.slf'
NUMBER OF FIRST TIME STEP FOR GRAPHIC PRINTOUTS:0
GRAPHIC PRINTOUT PERIOD: 120
LISTING PRINTOUT PERIOD: 10

```

VARIABLES FOR GRAPHIC PRINTOUTS:'U,V,B,H,S,T1'

/—/

/TIDE

/—/

TIDAL DATA BASE: 2

BINARY DATABASE 1 FOR TIDE : h tpxo9.v2

BINARY DATABASE 2 FOR TIDE : u tpxo9.v2

INITIAL CONDITIONS : 'TPXO SATELLITE ALTIMETRY'

MINOR CONSTITUENTS INFERENCE: YES

INITIAL TIME SET TO ZERO: YES

ORIGINAL DATE OF TIME: 2021 ; 03 ; 09

ORIGINAL HOUR OF TIME: 00 ; 00 ; 00

GEOGRAPHIC SYSTEM: 2

ZONE NUMBER IN GEOGRAPHIC SYSTEM: 33

COEFFICIENT TO CALIBRATE SEA LEVEL=-0.218

COEFFICIENT TO CALIBRATE TIDAL RANGE=1.1

TREATMENT OF THE LINEAR SYSTEM = 2

FREE SURFACE GRADIENT COMPATIBILITY = 0.9

OPTION FOR THE DIFFUSION OF VELOCITIES=2

CORIOLIS: YES

CORIOLIS COEFFICIENT = 9.6E-05

/—/

/COMPUTATION

/—/

TIME STEP: 1

NUMBER OF TIME STEPS: 216000

/—/

/PHYSICAL PARAMETERS

/—/

LAW OF BOTTOM FRICTION: 4

FRICTION COEFFICIENT: 0.028

CONTINUITY CORRECTION = true

MASS-BALANCE = YES

TURBULENCE MODEL = 1

DISCRETIZATIONS IN SPACE = 11; 11

```

SUPG OPTION =2;0
PRECONDITIONING =2
TIDAL FLATS =YES
TYPE OF ADVECTION =1;5
SOLVER = 1
/——/
/ TRACERS
/——/
NUMBER OF TRACERS = 1
NAMES OF TRACERS = 'TRACER in KG/M3 '
DIFFUSION OF TRACERS=YES
PRESCRIBED TRACERS VALUES = 0.055; 0
OPTION FOR THE DIFFUSION OF TRACERS = 2
/——/
/ WIND
/——/
WIND = YES
OPTION FOR WIND = 2
THRESHOLD DEPTH FOR WIND =0.1
COEFFICIENT OF WIND INFLUENCE VARYING WITH WIND SPEED:YES
ASCII ATMOSPHERIC DATA FILE = 'fo1 wind bisceglie 3gg.txt'

```

B.2.2. TELEMAC-3D coastal model code

```

TITLE = 'Coastal 3D model'
PARALLEL PROCESSORS: 12
OPTION FOR LIQUID BOUNDARIES:2;1
OPTION FOR TIDAL BOUNDARY CONDITIONS:0;1
PRESCRIBED ELEVATIONS =999;999
VELOCITY PROFILES =5;2
PRESCRIBED VELOCITIES =999;999
PRESCRIBED FLOWRATES=200;0
/————/
/INPUT
/————/
LIQUID BOUNDARIES FILE ='Portata 3gg 11 Mar 3km foce.lqd'

```



```
GEOMETRY FILE='GEOMETRY.slf'
BOUNDARY CONDITIONS FILE= 'mesh OLTRE PORTO BC.cli'
2D RESULT FILE: 'HYDRO 2D wind Bisceglie 5layer SAL38.slf'
3D RESULT FILE: 'HYDRO 3D wind Bisceglie 5layer SAL38.slf'
NUMBER OF FIRST TIME STEP FOR GRAPHIC PRINTOUTS:0
GRAPHIC PRINTOUT PERIOD: 120
LISTING PRINTOUT PERIOD: 1
VARIABLES FOR 2D GRAPHIC PRINTOUTS : 'U,V,H,S,F'
VARIABLES FOR 3D GRAPHIC PRINTOUTS : 'Z,U,V,W,TA1,TA2,TA3'
NUMBER OF HORIZONTAL LEVELS = 5
MESH TRANSFORMATION = 1
/————/
/TIDE
/————/
TIDAL DATA BASE: 2
BINARY DATABASE 1 FOR TIDE : h tpxo9.v2
BINARY DATABASE 2 FOR TIDE : u tpxo9.v2
INITIAL CONDITIONS : 'TPXO SATELLITE ALTIMETRY'
MINOR CONSTITUENTS INFERENCE:YES
ORIGINAL DATE OF TIME: 2021 ; 03 ; 09
ORIGINAL HOUR OF TIME: 00 ; 00 ; 00
GEOGRAPHIC SYSTEM:2
ZONE NUMBER IN GEOGRAPHIC SYSTEM: 33
COEFFICIENT TO CALIBRATE SEA LEVEL=-0.218
COEFFICIENT TO CALIBRATE TIDAL RANGE=1.1
FREE SURFACE GRADIENT COMPATIBILITY = 0.9
CORIOLIS: YES
CORIOLIS COEFFICIENT = 9.6E-05
HORIZONTAL TURBULENCE MODEL = 1
VERTICAL TURBULENCE MODEL = 2
MIXING LENGTH MODEL = 6
DAMPING FUNCTION = 2
AVERAGE WATER DENSITY=1000
/————/
/COMPUTATION
```

/————/

TIME STEP:1

NUMBER OF TIME STEPS:216000

/————/

/PHYSICAL PARAMETERS

/————/

LAW OF BOTTOM FRICTION: 4

FRICTION COEFFICIENT FOR THE BOTTOM:0.028

MASS-BALANCE =YES

TIDAL FLATS = YES

/————/

/ NUMERICAL SETUP OF THE COMPUTATION

/————/

SCHEME FOR ADVECTION OF VELOCITIES =5 /(default=5)

SCHEME FOR ADVECTION OF TRACERS =5;5;5 /(default=5)

SCHEME OPTION FOR ADVECTION OF VELOCITIES=4 /LIPS=4 (default=4)

SCHEME OPTION FOR ADVECTION OF TRACERS=4;4;4 /(default=4)

TREATMENT ON TIDAL FLATS FOR TRACERS=1

/————/

/ TRACERS

/————/

NUMBER OF TRACERS = 3

NAMES OF TRACERS = 'SALINITY KG/M3 '; 'TEMPERATURE DEGREE C '; 'TRACER in KG/M3 '

TRACERS VERTICAL PROFILES=2

DENSITY LAW=3

PRESCRIBED TRACERS VALUES = 0.00001; 9; 0.055; 38; 12; 0

INITIAL VALUES OF TRACERS = 38; 12; 0

/————/

/ WIND

/————/

WIND = YES

OPTION FOR WIND = 2

THRESHOLD DEPTH FOR WIND =0.1

COEFFICIENT OF WIND INFLUENCE VARYING WITH WIND SPEED:YES

ASCII ATMOSPHERIC DATA FILE = 'fo1 wind bisceglie 3gg.txt'

B.2.3. Other 3D model results

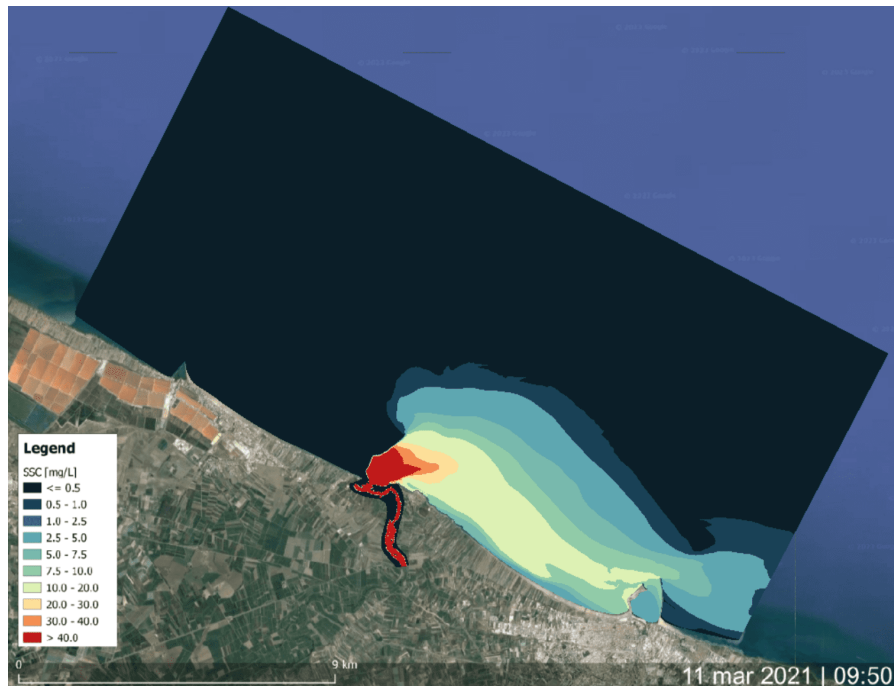


Figure B.15: 3D results using Constant viscosity model as both "Horizontal turbulence model" and "Vertical turbulence model".

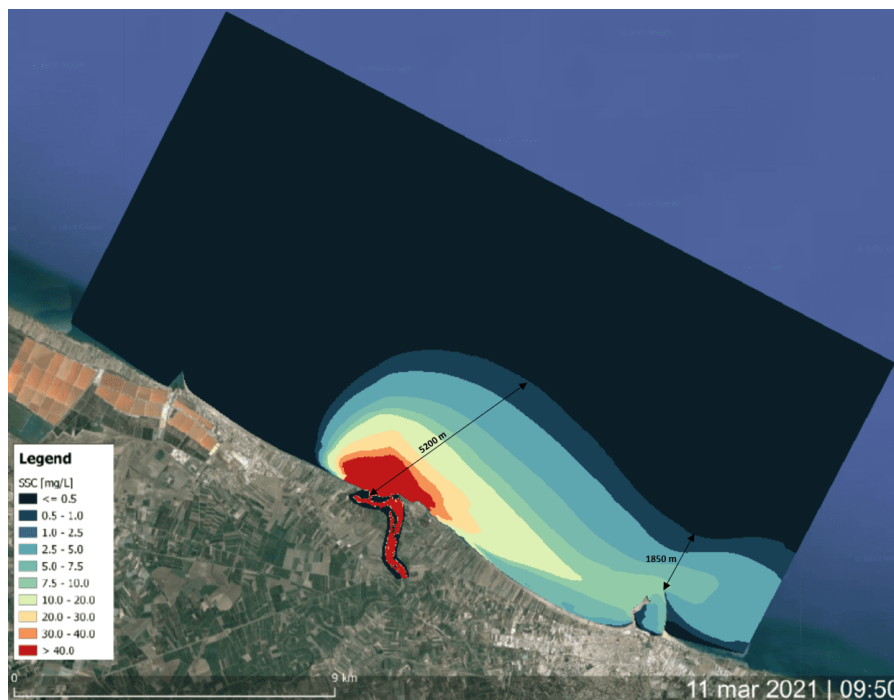


Figure B.16: 3D results using Constant viscosity model as "Horizontal turbulence model" and Mixing length as "Vertical turbulence model".

List of Figures

1.1	Extract from the cartography of the Kingdom of Naples in 1808 by G. A. Rizzi Zannoni; focus on the Ofanto River mouth and the nearby town of Barletta.	5
1.2	Ofanto catchment area and southern Adriatic Sea.	6
1.3	Ofanto River map [wik, 2020].	7
1.6	Dams and weirs in the Ofanto catchment area.	8
1.4	Change of the river mouth in the last century (according to the two previous studies).	8
1.5	Last two kilometers of the Ofanto River and its estuary mouth.	9
1.7	Coastal area between Margherita di Savoia and Barletta (area affected by the Ofanto’s fluvial plume phenomenon); image from Sentinel-2A, taken on March 5, 2023.	10
2.1	(a) Schematic representation of the plume liftoff process and the near-field plume region. (b) Large-scale mixing structures in the flow acceleration region. Panel (b) adapted from [Geyer et al., 2010]. (c) Shear instabilities comprising the large-scale mixing structures. Image and description from [Horner-Devine et al., 2015].	14
2.2	Schematic representation of the prototypical plume comprising all dynamical regions. Image and description from [Horner-Devine et al., 2015]. . . .	15
2.3	Schematic of the Dutch coast with different types of river plume fronts: tidal plume front (TPF), inner front (IF) of entire plume, outer front (OF) of entire plume, and relic tidal plume fronts (RF). Image and description from [Rijnsburger et al., 2021].	16

2.4	River plume morphologies: prototypical (plume A); nonrotational (plume B); wide estuary (plume C); angled inflow (plume D); delta plume (plume E); and region of freshwater influence (plume F). Inset images show examples of each plume type: (plume A) the Columbia River, (plume B) River Teign, (plume C) Chesapeake Bay, (plume D) Eel River, (plume E) Mekong River, and (plume F) Rhine River. Image and description from [Horner-Devine et al., 2015].	21
2.5	The plane wave solution of Maxwell's equations has the B field directly proportional to the E field at each point, with the relative directions shown.	23
2.6	Characteristic parameters of the electromagnetic signal.	23
2.7	Electromagnetic spectrum	24
2.8	SuperDove satellite.	28
2.9	SkySat satellite.	30
2.10	RapidEye satellite.	31
2.11	Landsat 8 satellite.	33
2.12	Sentinel-2A satellite.	34
2.13	Example of image search on the Planet website.	36
2.14	Example of satellite image capturing the Ofanto River plume (image taken by Dove Classic (PS2) on December 16, 2019, with a pixel resolution of 3 meters).	37
2.15	Location map of Arpa Puglia weather station (Barletta weather station in red).	38
2.16	Barletta weather station (daily rainfall).	39
2.17	Puglia Civil Protection stream gauging stations (Ofanto River stations in red).	40
2.18	Water level and discharge recorded at the San Samuele di Cafiero stream gauging station from 1 July 2019 to 31 March 2021.	41
2.19	Rete Mareografica Nazionale measuring stations (Bari in orange and Vieste in greenish).	42
2.20	Tides recorded in Bari and Vieste from 1 July 2019 to 31 March 2021.	43
2.21	Correlations between acquired data and plume direction.	46
2.22	Satellite images captured on 24, 25, 26, 27 April 2020.	48
2.23	Discharge, tides, wind direction and mean wave direction referring to the river plume event of April 24, 2020.	49
2.24	Plume of March 11, 2021.	50
2.25	Discharge, tides, wind direction and mean wave direction referring to the river plume event of March 9, 2021.	51

List of Figures	121
3.1 Methodology workflow chart.	53
3.2 River and coastal domains.	59
3.3 Mesh with illustrative zoom in the central area of the domain.	60
3.4 Comparison between flooded areas taken from satellite and simulated by the river model.	62
3.5 Simulated discharges with different Manning's coefficients, extracted at 3 kilometres from the mouth.	63
3.6 SNAP control panel.	65
3.7 Mesh with illustrative zoom in the river mouth area of the domain.	66
3.8 Satellite image on March 11, 2021, and the same with suspended sediment concentration (SSC).	68
3.9 Comparison of the tides recorded in Bari and Vieste with the one simulated in the coastal model with the TPXO database.	69
3.10 Satellite image of March 11, 2021, the same with suspended sediment concentration (SSC formula) compared with the simulated 2D model, using the wind recorded by the Bisceglie anemometric station.	70
3.11 2D simulations of the same event, applying different wind recordings.	71
3.12 Discharge extracted 3 kilometers from the river mouth, simulated with the river model.	72
3.13 Comparison of the tides recorded in Bari and Vieste with the one simulated in the coastal model with the TPXO database.	73
3.14 Satellite image of April 24, 2020, the same with suspended sediment concentration (SSC formula) compared with the simulated 2D model, using the wind recorded by the Manfredonia anemometric station.	73
3.15 Classical sigma transformation (homogeneous distribution of levels in the vertical direction).	79
3.16 Salinity concentrations and water temperature in the most superficial layer of the mesh (surface layer thickness: 0.76 meters) using $k - \epsilon$ turbulence model.	82
3.17 Comparison between the satellite image with the SSC formula applied and the 3D simulation using $k - \epsilon$ turbulence model.	84
A.1 Date: December 16, 2019, at 09:26. Instrument: Dove Classic (PS2). Pixel resolution: 3 meters.	93
A.2 Date: December 25, 2019, at 07:41. Instrument: Dove Classic (PS2). Pixel resolution: 3 meters.	94

A.3	Date: March 29, 2020, at 09:25. Instrument: Dove Classic (PS2). Pixel resolution: 3 meters.	94
A.4	Date: April 24, 2020, at 09:40. Instrument: Sentinel-2B. Pixel resolution: 10 meters.	95
A.5	Date: April 25, 2020, at 09:27. Instrument: Dove Classic (PS2). Pixel resolution: 3 meters.	95
A.6	Date: April 26, 2020, at 09:25. Instrument: Dove Classic (PS2). Pixel resolution: 3 meters.	96
A.7	Date: April 27, 2020, at 09:27. Instrument: Dove Classic (PS2). Pixel resolution: 3 meters.	96
A.8	Date: May 22, 2020, at 09:50. Instrument: Sentinel-2A. Pixel resolution: 10 meters.	97
A.9	Date: May 23, 2020, at 09:25. Instrument: Dove Classic (PS2). Pixel resolution: 3 meters.	97
A.10	Date: May 25, 2020, at 07:20. Instrument: Dove Classic (PS2). Pixel resolution: 3 meters.	98
A.11	Date: December 05, 2020, at 09:53. Instrument: Dove Classic (PS2). Pixel resolution: 3 meters.	98
A.12	Date: December 10, 2020, at 09:14. Instrument: Dove R (PS2.SD). Pixel resolution: 3 meters.	99
A.13	Date: January 14, 2021, at 09:43. Instrument: Sentinel-2A. Pixel resolution: 10 meters.	99
A.14	Date: January 14, 2021, at 09:22. Instrument: Dove Classic (PS2). Pixel resolution: 3 meters.	100
A.15	Date: February 03, 2021, at 09:26. Instrument: Dove Classic (PS2). Pixel resolution: 3 meters.	100
A.16	Date: February 18, 2021, at 09:40. Instrument: Sentinel-2B. Pixel resolution: 10 meters.	101
A.17	Date: March 11, 2021, at 09:50. Instrument: Super Dove (PSB.SD). Pixel resolution: 3 meters.	101
A.18	Matlab code to extract ERA5 data.	102
B.1	River bottom.	103
B.2	Simulation 1 Manning's coefficients.	104
B.3	Simulation 2 Manning's coefficients.	104
B.4	Simulation 3 Manning's coefficients.	105
B.5	River model boundary conditions.	105

B.6 Upstream area satellite image. 108

B.7 Upstream area Simulation 3. 108

B.8 Central area satellite image. 109

B.9 Central area Simulation 3. 109

B.10 Downstream area satellite image. 110

B.11 Downstream area Simulation 3. 110

B.12 Coastal model bottom. 111

B.13 Coastal model Manning’s coefficients. 111

B.14 Coastal model boundary conditions. 112

B.15 3D results using Constant viscosity model as both "Horizontal turbulence
 model" and "Vertical turbulence model". 117

B.16 3D results using Constant viscosity model as "Horizontal turbulence model"
 and Mixing length as "Vertical turbulence model". 117

List of Tables

2.1	PlanetScope satellite characteristics.	28
2.2	SkySat satellite characteristics.	29
2.3	RapidEye satellite characteristics.	31
2.4	Landsat 8 satellite characteristics.	32
2.5	Sentinel-2 satellite characteristics.	34
2.6	Various spatial resolutions of the described satellites.	35
2.7	Plumes directions and correlations with acquired data.	45
3.1	Manning's coefficients used and simulation results extracted 3 kilometers from the mouth.	64
3.2	The best set of physical parameters resulting from the calibration exercise of the TELEMAC-2D model.	69
3.3	The best set of physical parameters resulting from the calibration exercise of the TELEMAC-3D model.	81
3.4	Vertical layers in the 3D model.	81
3.5	Comparison between satellite data and 3D model.	83

